

Diagnostics of ion generation and fluxes from cathodic arc spots for a better understanding of energetic deposition of thin films

Von der Fakultät für Physik und Geowissenschaften
der Universität Leipzig
genehmigte

DISSERTATION

zur Erlangung des akademischen Grades
doctor rerum naturalium

Dr. rer. nat.

vorgelegt
von M. Sc. Kyunghwan Oh
geboren am 05.01.1984 in Seoul, Republic of Korea

Gutachter: Prof. Dr. rer. nat. Anders, André
Prof. Dr. Keidar, Michael

Tag der Verleihung: 16. March 2023

Die vorgelegte Arbeit entstand zwischen Januar 2019 und März 2022
am Leibniz-Institut für Oberflächenmodifizierung e.V. (IOM)
Permoserstraße 15
04318 Leipzig
Deutschland.

Die Arbeit wurde betreut von
Prof. Dr. André Anders.
Dr. Dmitry Kalanov.
Dr. Yeliz Unutulmazsoy.

Bibliographische Beschreibung

Oh, Kyunghwan

Diagnostics of ion generation and fluxes from cathodic arc spots for a better understanding of energetic deposition of thin films

Universität Leipzig, Dissertation

105 S.¹, 243 Lit.², 51 Abb., 6 Tab.³

Referat

In dieser Arbeit werden die Ionenerzeugung und die Ionenflüsse aus kathodischen Lichtbogenflecken für die energetische Abscheidung von Dünnschichten untersucht. Die Ionenerzeugung hängt mit den Eigenschaften des Lichtbogenpunkts zusammen, und die Ionenflüsse beeinflussen die Schichtabscheidung. Bezeichnenderweise hat der kathodische Lichtbogen einen explosionsartigen Zündprozess, der der Prozess der Ionenerzeugung ist. Daher ist es nicht einfach, die Brennfleckeneigenschaften zu beobachten, und die grundlegende Frage im Zusammenhang mit der Fleckenbewegung ist noch offen. Die mehrfach geladenen Ionen, die bei der Spot-Zündung erzeugt werden, haben höhere Ionenpotenzialenergien als Ionen bei andere Abscheidetechniken; daher muss die Auswirkung der Ionenpotenzialenergie auf das Schichtwachstum bei der kathodischen Lichtbogentechnik berücksichtigt werden.

Der erste Teil dieser Arbeit befasst sich mit der grundlegenden Charakteristik des Lichtbogenbrennflecks, insbesondere mit der Entwicklung der Brennfleckbewegung in einer magnetisch gesteuerten Bogenquelle, die sich im Vakuum- oder in einer Reaktivatmosphäre befindet. Zur Untersuchung wird einer Streakkamera, die eine hohe räumliche und zeitliche Auflösung aufweist, benutzt. Zur Beantwortung der grundlegenden Frage, ob die Brennflecken charakteristische Zeiten haben, wie z.B. eine "Brennfleckenlebensdauer" oder eine "charakteristische Zeit zwischen den Brennfleckzündungen", wurden die Streakbilder durch schnelle Fourier-Transformation (FFT) analysiert. Es wurde gefunden, dass das Leistungsspektrum der Lichtbogenfleckenfluktuationen keine spezifischen Frequenzen aufweist, was bedeutet, dass der Lichtbogenzündungsprozess durch ein entsprechendes fraktales Modell beschrieben werden kann und dass der Anstieg der Geraden in der log-log Leistung-Frequenz-Darstellung bei Vorhandensein einer Verbundschicht (z.B. Oxid oder Nitrid) tendenziell abnimmt. Durch die Fraktalanalyse und zusätzliche Messungen der optischen Emissionsspektroskopie wird auch die fundamentale Grenze der zeitlichen Auflösung für die optische Emissionsmethode erkannt und berücksichtigt.

¹ S.: Seitenzahl insgesamt

² Lit.: Anzahl der im Literaturverzeichnis ausgewiesenen Literaturangaben

³ Tab.: Anzahl der Tabellen

Der zweite Teil dieser Arbeit befasst sich mit den Anwendungsaspekten des kathodischen Bogens: der energetischen Abscheidung. Die meisten Studien im Zusammenhang mit der energetischen Abscheidung haben bisher die Auswirkungen der kinetischen Energie der Ionen auf die Schichtabscheidung untersucht; diese Arbeit hier konzentriert sich jedoch auf die Auswirkungen der potenziellen Energie der Ionen auf das Schichtwachstum. Um die Auswirkungen der potenziellen Ionenenergie auf das Schichtwachstum zu untersuchen, wurden eine Plasmadiagnose mittels energieaufgelöster Massenspektroskopie und die Charakterisierung der abgeschiedenen Schichten mittels XRD, XRR, AFM und SEM durchgeführt. Die Energie des Ionenpotenzials beeinflusst die Vorzugsrichtung des Schichtwachstums im Falle der Aluminiumabscheidung. Dieses Ergebnis könnte ein Ausgangspunkt für weitere Forschungen über die Auswirkung der Ionenpotenzialenergie auf die Schichtabscheidung sein.

Bibliographic Description

Oh, Kyunghwan

Diagnostics of ion generation and fluxes from cathodic arc spots for a better understanding of energetic deposition of thin films

University Leipzig, Dissertation

105 pages, 243 references, 51 figures, 6 Tables

Abstract

This thesis is devoted to the investigation of ion generation and fluxes from cathodic arc spots for a better understanding of energetic deposition of thin film. The ion generation is related to the arc spot properties, and ion fluxes influence the film deposition. Significantly, the cathodic arc has the explosion characteristic for the ignition process, which is the generation process of ions. Thus, it is not easy to observe the spot characteristics, and some fundamental questions related to cathodic arc spot motion are still open. The multiply charged ions produced from the arc spot ignition process have a higher ion potential energy than ions of other deposition techniques; therefore, consideration of the effect of ion potential energy on film growth is required for the cathodic arc technique.

The first part of this thesis deals with fundamental arc spot characteristics, especially the trend of spot motion in a magnetically steered arc source placed in vacuum or in a reactive gas atmosphere. This is investigated with a streak camera having high spatial and temporal resolutions. To answer the fundamental question of whether the spots have characteristic times, such as a "periodic spot lifetime" or a "the periodic characteristic time between spot ignitions", the streak images were analyzed by fast Fourier transformation (FFT). It was found that the power spectrum of the arc spot fluctuations does not show any specific frequencies, which means the arc spot ignition process can be described by a fractal model, and the spectral slope in the log-log power-frequency diagram has a tendency to be reduced in the presence of a compound (for example oxide or nitride) layer on the cathode surface. Through the fractal analysis and measurements of optical emission spectroscopy, the fundamental limitation of the temporal resolution for the optical emission method is determined and considered.

The second part of this thesis considers cathodic arc's application aspects: the energetic deposition of thin films and coatings. Most studies related to energetic deposition have previously investigated the effects of ion *kinetic* energy on film deposition; however, this thesis focuses on the effects of ion *potential* energy on film growth. To investigate the effect of ion potential energy on film growth, plasma diagnostic by energy-resolved mass spectrometry and deposited film characterization by XRD, XRR, AFM, profilometry and SEM were carried out. The ion potential energy influences the preferential direction of film growth or a polycrystalline growth in the case of aluminum deposition. This result could be a starting point for further research into the effect of ion potential energy on film deposition.

Contents

1. Introduction	1
2. Theory and literature review	4
2.1 Cathodic arcs	4
2.1.1 Cathodic arc ignition process	4
2.1.2 Cathodic arc voltage and current characteristics	14
2.1.3 Theoretical plasma expansion model	17
2.1.4 Types of cathodic arc spots	19
2.1.5 Cathodic arc spot motion in a magnetic field	23
2.1.6 Fractal spot model	26
2.2 Film deposition	29
2.2.1 Energetic deposition	29
2.2.2 Ion kinetic and potential energies	30
3. High-resolution observations of cathode spots with a streak camera	34
3.1 The concept of observing of cathode spots	34
3.2 Plasma diagnostics	34
3.2.1 High resolution streak camera observations	34
3.2.2 Optical emission spectroscopy	38
3.3 Experimental setup	40
3.4 Streak image results	43
3.4.1 Arcs in vacuum	43
3.4.2 Arcs in low pressure argon, nitrogen, and oxygen atmospheres	47
3.5 Fast Fourier transform (FFT) analysis of experimental results	54
3.5.1 FFT analysis of arcs in vacuum	55
3.5.2 FFT analysis of arcs in low pressure argon, nitrogen, and oxygen atmospheres	56
3.6 Fundamental limitations of optical emission method	59
3.7 Discussion & conclusions	60
4. Investigation of effect of ion potential energy on film growth	62
4.1 Three different cases for investigation of the effect of ion potential energy on film growth	62
4.2 Tuning of ion kinetic and potential energies	63
4.3 Experimental setup	64
4.4 Plasma diagnostics	67
4.4.1 Voltage and current characteristic analysis	67
4.4.2 Energy-resolved mass spectrometry	67
4.5 Plasma characterization results	69
4.5.1 Voltage and current data	69
4.5.2 Ion energy distributions	71
4.6 Film characterization results	74
4.6.1 X-ray diffraction (XRD) and X-ray reflectivity (XRR) analysis	74
4.6.2 Atomic force microscopy (AFM) analysis	78

4.6.3 Scanning electron microscope (SEM) analysis	78
4.7 Discussion & conclusions.....	80
5. Summary and conclusions	82
Bibliography	84
Acknowledgements	100
Scientific curriculum vitae	101
List of own peer-reviewed publications	102
List of own presentations	103
Author contribution	104
Declaration of academic integrity.....	105

1. Introduction

The cathodic arc discharge is one of the oldest techniques to generate plasma, which stands for one mode of arc discharge [1]. The arc discharge can be developed in gas atmospheres at atmospheric pressure, or, in a low- or high- pressure medium, or in vacuum [1]–[3]. The arc discharge may thus appear in various environments, and the discharge can be applied to a wide range of applications such as vacuum interrupter [4], cutting [5], welding [6], or thin film deposition [1].

The cathodic arc discharge is widely used [1], [7]. Considering the thin film deposition, understanding the generation of ions is essential: first, which is the material to be deposited, and second, the flux of the ions because the energy of the ions is influenced during the generation and flux processes, which affects film growth. The ions are generated in a high energy plasma area called “spots” near the cathode surface, in which the plasma is fully ionized [1]. Namely, the cathode spots are the primary source (location) for plasma generation in the case of the cathodic arc. The spots are formed with tiny mobile luminaries, as shown in Figure 1-1. The investigation of spots is therefore an essential factor for understanding the generation of ions.

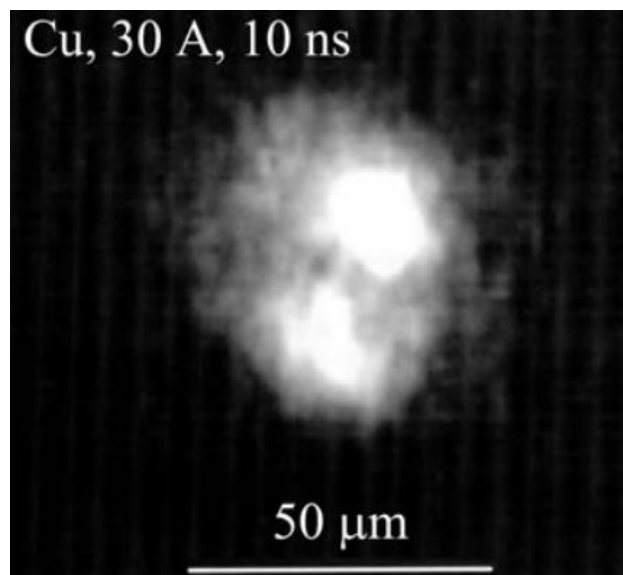


Figure 1-1 An example of the cathode spot image, recorded by a CCD camera (IMACON 468) at a surface of copper cathode (The applied arc current was 30 A). The exposure time for this recording was 10 ns [8].

The cathode spots were researched on various topics such as observation of the appearance of spot motion in the absence [9]–[13] or presence [14]–[21], [22]–[25] of an external magnetic field,

properties of the cathode spots [26]–[30], and investigation of the spot craters on the cathode surface [31]–[35]. However, the abovementioned investigations with theoretical and experimental approaches are inconclusive related to whether arc spots have characteristic times such as a ‘periodic spot lifetime’ (or frequencies) between spot ignitions. This topic is still an open question, and there are two central claims. The first one is that the spots have a periodic lifetime of nanoseconds [36], [37] or microseconds [38], and the second one is no specific frequency related to the arc ignition process [39], which is described in the framework of fractal model [40], [41].

The generated plasma, including ions, in the cathode spot center spreads rapidly into the vacuum, low pressure-area, or substrate with having a certain amount of energy. In the case of a vacuum arc, the flux of ions keeps the energy until hitting the wall or substrate, while they lose energy due to collisions with neutrals in the case of presence of process gas. Although this phenomenon commonly occurs for all types of gas, additional consideration is required if the gas is reactive, since additional chemical reactions take place between the cathode surface and the reactive gas, affecting the spot ignition process. The effect of the reactive gas on the cathodic arc spot relatively little has been investigated.

The energy of ions consists of kinetic and potential energies [42]. In general, the effect of ion kinetic energy on film deposition has been extensively studied [43]–[45]. In contrast, the effect of the ion potential energy on the film deposition has not been investigated much, although the potential energy of ions contributes to film deposition [42]. When the ions arrive at the substrate surface, the potential energy may cause atomic scale heating [42], [46] through the local release of potential energy via a complicated electron-phonon coupling [42], which is especially significant for multiply charged ions [47]. Thus, the potential energy effect is critical to high energetic deposition process, such as cathodic arc plasma deposition.

This thesis aims to better understand the complex cathodic arc spot ignition process and application for thin film deposition based on plasma diagnostics. To understand the fundamental cathodic arc spot ignition process, apparent steered arc spot motion in vacuum or in gas atmospheres is observed with a high resolution (temporal, and spatial) diagnostic device. The investigation of cathodic arc spots is still an important topic since the types of cathode spots influence the plasma properties [48], [49], and arc performance in applications [1], [50], as it affects the relative stability of a cathodic arc [3]. Also, there is still a fundamental open question about whether arc spots have periodic characteristic times such as a “periodic spot lifetime” or a “periodic characteristic time between spot ignitions”. The observation of cathodic arc spots is generally not accessible due to the short formation time of arc and the small scale of microexplosions [26], [36], [51].

To better understand the application for the thin film deposition based on plasma, the effect of ion potential energy on film growth is investigated using a combination of energy-resolved ion mass spectrometry and film characteristics. In general, the cathodic arc plasma is characterized by a high ionization of metal plasma, causing multiply charged ions [52], which is one of the main differences of the arc plasma compared to other type of plasmas. The highly charged ions have high ion potential energy and high kinetic energy. Therefore, the effect of ion potential energy cannot be ignored in the high energetic deposition process, such as cathodic arc deposition [42], [47].

This thesis is organized as follows: this chapter (chapter 1) describes the structure and objectives. An overview of cathodic arcs, including the cathodic arc ignition process, voltage and current characteristics, plasma expansion, types of cathodic arc, apparent motion of spots in the presence of an external magnetic field, and fractal model are introduced in the first part of the theory and literature review (chapter 2). The second part of the theory and literature (chapter 2) review introduces the energetic deposition based on the description of ion kinetic and potential energy.

In chapter 3, the observation of apparent motion of cathode spot in vacuum or in a low-pressure atmosphere (noble or reactive gas) with high resolution is discussed to observe the appearance of spot motion and to answer the fundamental question about whether arc spots have periodic characteristic times such as a “spot lifetime” of a “characteristic time between spot ignitions”. Through the plasma diagnostics (streak camera and optical emission spectroscopy), which were applied for the experiment, the limitations of the diagnostic method, and analyzed data with the fractal model are explained. This chapter is published in ref. [53], [54].

In chapter 4, the investigation of the effect of ion potential energy on film growth is carried out. This chapter presents the ion potential energy tuning method and the utilized plasma diagnostics (voltage and current characteristics and energy-resolved ion mass spectrometry). The results of plasma and film characterization are discussed to better understand the effect of ion potential energy on film growth.

In chapter 5, the summary of the thesis and main conclusions are given.

2. Theory and literature review

This chapter introduces fundamental knowledge of the cathodic arc, including ignition process of cathodic arc spots, voltage and current characteristics, plasma expansion, and apparent motion of spots in a magnetic field, through a literature review of previous research. Also, one of the theoretical approaches to interpreting the cathodic arc spot, the fractal model, is presented. The concept of energetic film deposition is briefly introduced, and the effect of energetic deposition on film growth also is covered by elucidating the ion kinetic and potential energies.

2.1 Cathodic arc

2.1.1 Cathodic arc ignition process

The properties of the cathodic arc

Plasma is often called the fourth state of matter [55], and has a quasi-neutral collective behavior [56] is being used in numerous fields, including in the industry, and research, and medical areas. Plasmas have different physical parameters, such as plasma density and temperature, depending on the kind of plasma [2]. The plasma to be handled mainly with this thesis is a cathodic arc plasma formed at a cathode electrode [1] in vacuum or low-pressure atmosphere. The cathodic arc plasma source has several exclusive features compared to other plasma sources. The cathodic arc has an unique voltage-current characteristic, like relatively low discharge voltages and high current [1], [3], [57], [58], also there is a small, mobile, luminous formation which is called “spot”, on the cathode surface [1], [3], [59], [60].

The cathodic arc plasma contains multiply charged ions [61]–[64] and has a high ion velocity [65]–[67], typically 10^4 m/s. The cathodic arc plasma has strongly fluctuating parameters [68]–[71] since the electron emission occurs explosively [37], [72]–[79]. The plasma is non-uniform due to the spot generation at a tiny area and the plasma expansion, which causes a significant difference in plasma density [1], [52], [67], [80], [81].

The cathodic arc plasma can be produced through electrical discharge. In vacuum, the electrical discharge occurs in vaporized electrode material forming a conductive medium [3]. Even in the case of presence of gas, the primary electrical discharge happens in vaporized electrode material, but the electrical discharge starts in a compound layer of the cathode electrode [1]. The phase transition of

electrode material into plasma occurs extremely fast, shorter than 1 ns [1], due to the high energy density of the cathode spot region. This phase transition in which electrode material directly changes into the supercritical fluid that finally evolves into a fully ionized plasma could be carried out at the beginning of the explosive stage since the small volume of material is heated rapidly. It causes the density of material to initially to remain almost constant, it can exceed the temperature of the critical point C; following the path in the diagram goes to the right almost horizontally, as shown in Figure 2-1 (Path ii) [52], [82].

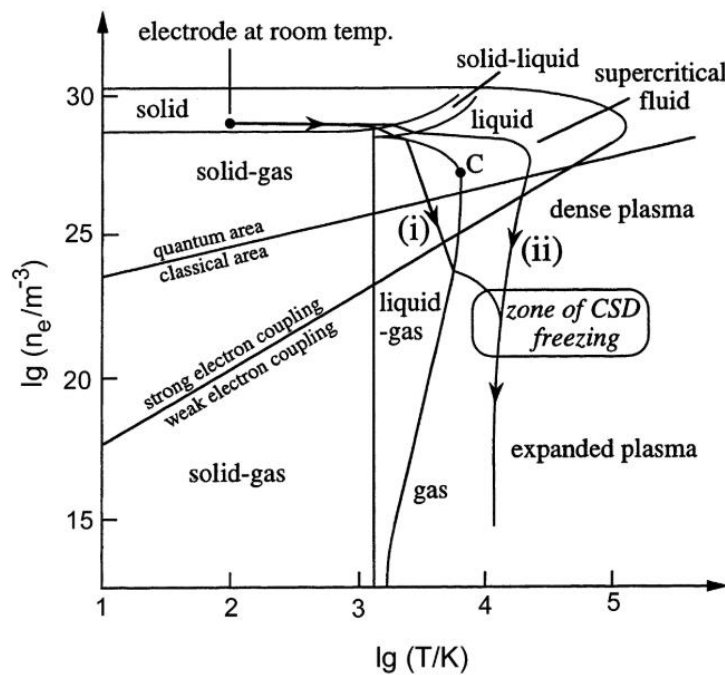


Figure 2-1 The phase diagram of copper in the density-temperature phase diagram: (i) classical model, with melting, evaporation, and ionization and (ii) model of microexplosions, circumnavigating the critical point C [52], [82]. Both paths of phase transition merge approximately in the zone of charge state distribution freezing (CSD), which is the zone, where the charge state distribution remains constant when the plasma expands into the vacuum [82].

The cathodic arc ignition process

The cathodic arc ignition process is central in producing cathodic arc plasma [1]. The process has different characteristics than other plasma processes, such as high-power impulse magnetron sputtering (HiPIMS). The cathodic arc ignition process has typically low sustaining voltage (12 – 28 V) for currents less than 1 kA, which is named the “burning voltage”. It is the main feature to distinguish

arcs from magnetron sputtering discharges [83], which may have similar current levels. The general potential distribution between cathode and anode is shown in Figure 2-2.

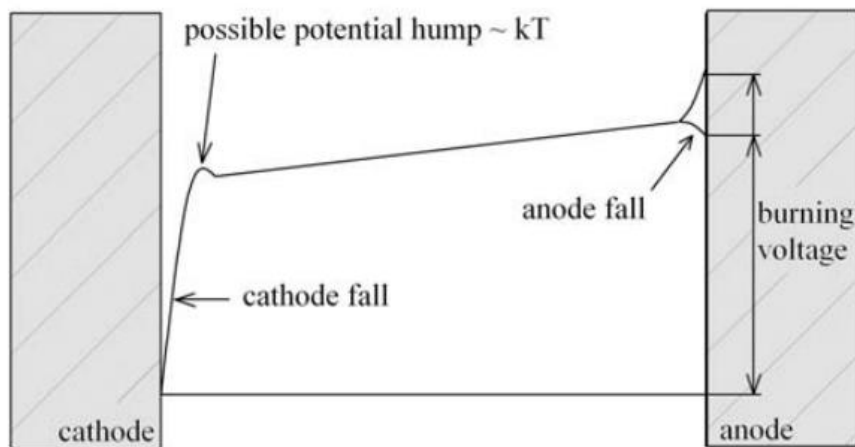


Figure 2-2 A simple drawing of the potential distribution between cathode and anode (not to scale) [1]

The cathodic arc can cover two different ignition environments, such as ignition occurring in the presence of ambient gas or a vacuum. In the case of the presence of reactive gas, such as oxygen or nitrogen, it is called “reactive cathodic arc”, and it is called “vacuum arc” in the absence of gas injection. The presence or absence of reactive ambient gas makes a big difference, namely nitrided [54] or oxidized [54] cathodic surface cause a distinct spot type [31]–[33] and ignition features. The spot ignition is accompanied by electron emission for both presence and absence of gas.

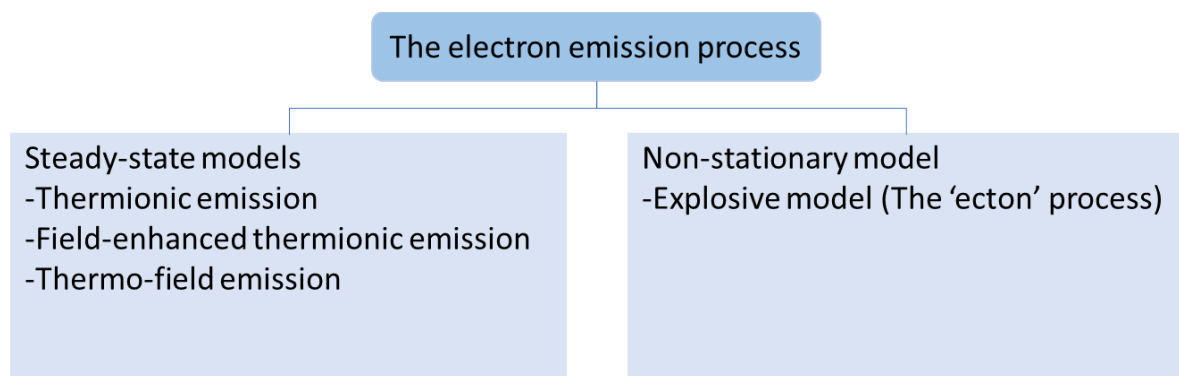


Figure 2-3 Classification of the electron emission process of vacuum arc

The electron emission process of vacuum arc can be classified mainly by two different model groups (Figure 2-3) [1],[84]. The first group is a steady-state, stationary or quasi-stationary which is governed

by thermionic emission of electrons [85]–[89] when the cathode is very hot; field emission [90]–[94] when a strong field is present, and thermo-field emission [95]–[99] when both the cathode is hot and a strong field is present. The second group is an non-stationary, describing ion-enhanced thermo-field emission of electrons [84], [100], [101], leading to explosions [75]–[79], [102], [103] for the operation of discharge.

Stead-state models

The thermionic emission

The thermionic emission of electrons is a model to consider electron emission at elevated temperature. The emission current density from the cathode can be described by the Richardson-Dushman [86]–[89] equation as defined in equation 2.1.

$$j_{thermionic} = AT^2 \exp\left(-\frac{\phi}{kT}\right) \quad (2.1)$$

where ϕ is a work function, k is the Boltzmann constant, and T is the absolute temperature of the emitting electrode. A is the universal Richardson constant, defined as $A = \frac{4\pi em_e k^2}{h^3} = 1.202 \times 10^6 \text{ A/m}^2 \text{K}^2$, where h is the Planck constant, m_e is electron mass. The thermionic emission of electrons only considers electron emission when the temperature is sufficiently high. However, in practical cases, an electric field also exists on the cathode surface [1].

The field emission

If a strong electric field is present at the cathode surface, the field emission model applies: the emission of electrons occurs quantum mechanically through the tunneling effect [1], [90]. The tunneling effect changes the shape of the potential barrier; thus, the electrons can penetrate through the potential barrier even if the energy is less than the barrier height, also the electron penetration occurs even at temperature $T = 0$. The convenient numerical form [91], [92] of emission current density under high electric field strength and low temperature case, based on Fowler-Nordheim formula [94] can be described as equation 2.2.

$$j_{FN}(E_{Field}) = 1.541 \times 10^{-6} \frac{E_{Field}^2}{\phi t^2(y)} \exp\left[-6.831 \times 10^9 \frac{\phi^{3/2} v(y)}{E_{Field}}\right] \quad (2.2)$$

$$y = 3.795 \times 10^{-5} \sqrt{E_{Field}} / \phi \quad (2.3)$$

where E_{field} is electric field, $v(y)$ is the elliptical function that consider the effect of the image force on the emitted electron, and $t(y)$ is a related function $v(y)$ [92]. The numerical values of the Fowler-Nordheim Field Emission function $v(y)$ and $t(y)$ are given in the reference [1], [92].

The thermo-field emission

The previous thermionic and field emission processes describe extreme cases such as very high temperatures with a relatively low electric field and a very high electric field with low temperatures. However, most practical arc discharge cases are considered high temperature and high electric fields. The model is named the “Thermo-field emission model”. The simplified emission current density [93] is defined as equation 2.4, which is obtained by calculating the emission current density based on quantum mechanics [95], [96], [104].

$$j_{TF}(T, E_{Field}) \approx k(AT^2 + BE_{Field}^{\frac{9}{8}}) \exp \left[- \left(\frac{T^2}{C} + \frac{E_{Field}^2}{D} \right)^{-\frac{1}{2}} \right] \quad (2.4)$$

where $A = 120$, $B = 406E_{Field}^{0.1(\phi-4.5)} \exp [-2.22(\phi - 4.5)]$, $C = 2.727 \times 10^9(\phi/4.5)^2$, $D = 4.252 \times 10^{17}(\phi/4.5)^3$. The calculated emission current density is depicted in Figure 2-4 as a function of the cathode surface temperature and surface electric field with a fixed work function ($\phi = 4.2\text{eV}$) [104].

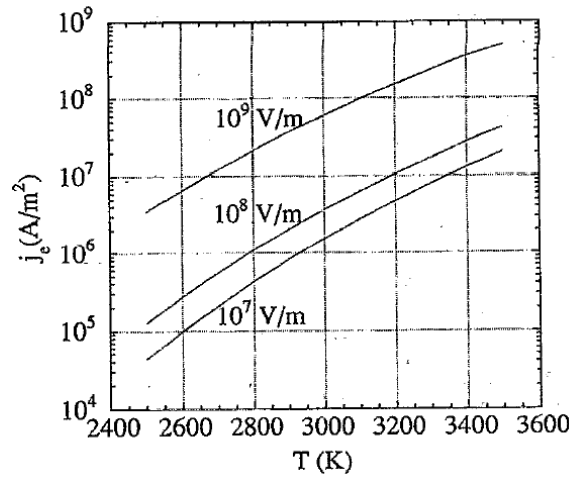


Figure 2-4 The calculated emission current density as a function of the cathode surface temperature and the surface electric field with $\phi = 4.2\text{eV}$ [104].

The emission of the electron in a stationary or quasi-stationary way is assumed in specific conditions such as high cathode temperature, high electric field, or presence of both. However, it is not enough to explain cathodic arc discharge practically since the presence of a space-charge layer which is called “sheath” [105]–[109]. The sheath is a thin layer where a plasma contacts a solid such as the cathode surface or chamber wall. If the thickness is sufficiently thin, the sheath layer could be collision-free, but if the thickness is thick, collisions may occur inside the sheath. The thickness of the sheath also determines the electric field strength for a given voltage drop. If the sheath is getting thinner, the electric field strength is enhanced. The sheath thickness is not fixed but self-adjusting, depending on plasma density. Consequently, the cathodic arc plasma and the sheath are not stationary. The sheath thickness is given by the Child law [1], [110] as

$$S_{Child} = \frac{\sqrt{2}}{3} \lambda_{De} \left(\frac{2e|\Delta V|}{kT_e} \right)^{3/4} \quad (2.5)$$

where λ_{De} is Debye length ($\lambda_{De} = (\epsilon_0 kT_e / n_e e^2)^{1/2}$), ΔV is the potential difference between cathode and plasma ($\Delta V = V_{cathode} - V_{pl}$), $k \approx 1.38 \times 10^{-23} J/K$ is the Boltzmann constant, $\epsilon_0 \approx 8.854 \times 10^{-12} F/m$ is the permittivity of free space, and $e \approx 1.60 \times 10^{-19} C$ is the elementary charge. In the sheath, due to the cathode fall being present (Figure 2-2), some positive ions approach the cathode surface with a kinetic energy corresponding to a voltage drop. As the ions approach very close (about 1 nm) to the cathode surface, the ions have some effect on changing the potential barrier [110]. Also, the ions approaching the cathode surface with the kinetic energy bring back energy to the cathode surface by changing their energy to heating energy. This phenomenon is called ion bombardment heating, and ion heating contributes to enhance locally thermo-field emission mechanism [1]. The ion bombardment heating followed by localized high electric field strength and heating leads to a non-stationary localized electron emission on the cathode surface [102], [103].

Non-stationary model

The ‘ecton’ process

A type of explosion accompanies the electron emission, and the explosive evaporation occurs non-stationary in every different explosive emission center during the ignition process. This explosive emission is often described as the ‘ecton’ process [77], [79], [111]; the ecton is a minimum unit of explosive processes at the tip of a jet of molten metal from the cathode, as shown in Figure 2-5. At this moment, the jet of molten metal is created by high pressure [35] [78] in the vicinity of the

explosion center. The crater formation on the cathode surface is one of the evidence of explosions, accompanied by a temporary extremely high-power density and high-pressure gradients. Even before detaching, the jet of molten metal creates a droplet when the current exceeds the threshold current; this droplet causes an increase in the current density between the jet of molten metal and the droplet at the junction point [77]. The ecton process leads to plasma formation [112], and the process is related to energy dissipation which is correlated with power density and energy balance [113] on the cathode surface.

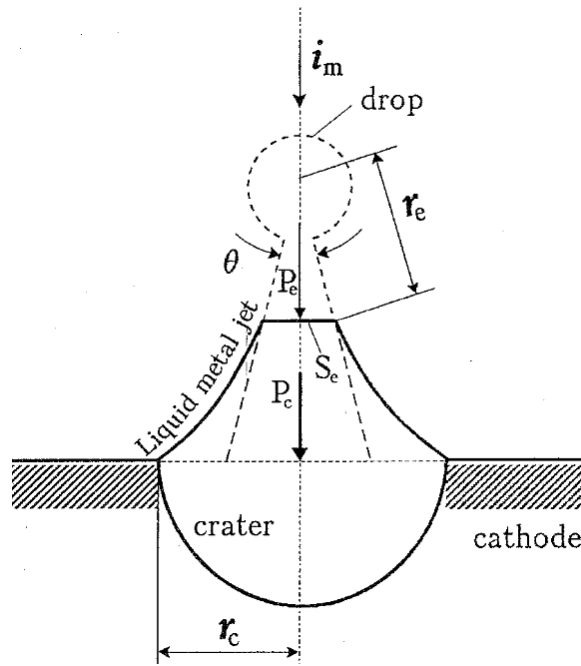


Figure 2-5 A conical jet of liquid metal producing an ecton [77] (i_m : the minimum current of the cell, r_e : length of the generatrix of the cone, r_c : radius of a crater, P_e : expert pressure on the cathode, P_c : pressure in the crater, S_e : emission area, θ : vertex angle of the jet of molten metal)

The plasma produced from the cathode material is scattered by the explosion and propagated much greater than the crater area. The plasma scattering is proposed in the adiabatic model [78], [114], and the kinetic energy of the plasma particles is converted from the explosion energy. The emission current density of the ecton model is defined as [77]

$$j_e = \frac{\pi \theta^4 \alpha \bar{h}}{4 i_m} \quad (2.6)$$

where α is the thermal diffusivity, and \bar{h} is called the specific action [72], [77], [115], [116]. The specific action value depends on the cathode material also, the value can be evaluated by [116]

$$\bar{h} = \frac{\rho c}{\kappa_0} \ln \frac{T_{cr}}{T_0} \quad (2.7)$$

where T_{cr} is a critical temperature as occur explosion, T_0 is the initial temperature of the cathode, and ρ is the density of the cathode material. If the resistivity is given by $\kappa = \kappa_0 T$, the heat capacity c is independent. The jet of molten metal makes possible the ion bombardment heating and field enhancement conditions on the cathode surface. The jet towards the potential spot emission center [1], [8], [15]. Thus, the new spot center could follow the direction of the jet, as shown in Figure 2-6.

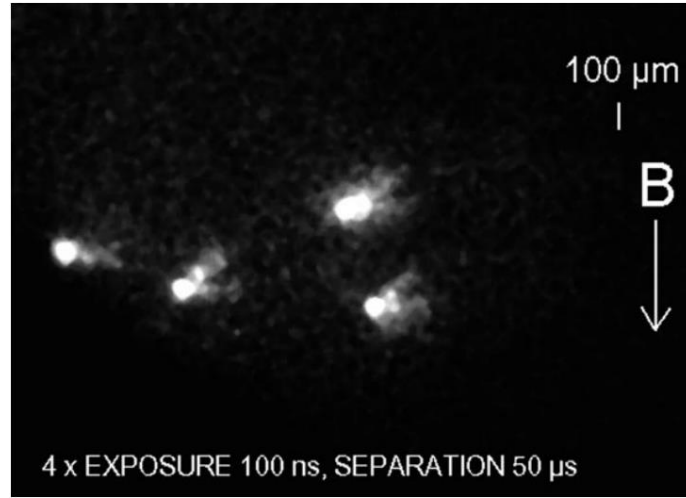


Figure 2-6 Fourfold exposure of a single spot with 50 μs separation of the exposures was recorded by a CCD camera (IMACON 468). The new spot emission center follows the direction of the jets. ($I = 20\text{ A}$, 5 $\mu\text{m}/\text{pixel}$, with external magnetic field) [15]

Typically, the spot ignition occurs in a random direction, but if an external magnetic field is present, the apparent spot motion has a preferred direction [16], [17], [117]–[119]. This phenomenon will be discussed in detail in chapter 2.1.5.

The arc triggering

The high spot temperature and strong electric field are required to start the arc plasma. To fulfill these conditions, various types of triggers are used, such as contact breaking (pulling apart) of main electrodes [120]–[123], mechanical trigger [1], and “triggerless” or surface ignition [124]–[129]. The contact breaking of the main electrodes has the same operation principle as vacuum circuit interrupters [130]. When one of the electrodes is separating from the other, the contacting area is reduced, and high current density applies to microscopic points since the electrode surface is not ideally smooth. In the case of mechanical trigger method (Figure 2-7), the contact breaking method is

used by mechanical devices with an additional electrode called trigger pin. The trigger pin is connected to the anode and touches the cathode with a mechanical device. The trigger pin has a specific resistor between cathode and anode to allow arc initiation at reduced but sufficiently high current. However, if the resistor is too low, the trigger pin can be welded, or too high, the ignition cannot occur. The proper resistor range is about $2 \sim 10 \Omega$ [1]. Mechanical trigger initiation is a very stable method for ignition. However, it cannot be supported to apply pulsed ignition with a high repetition rate.

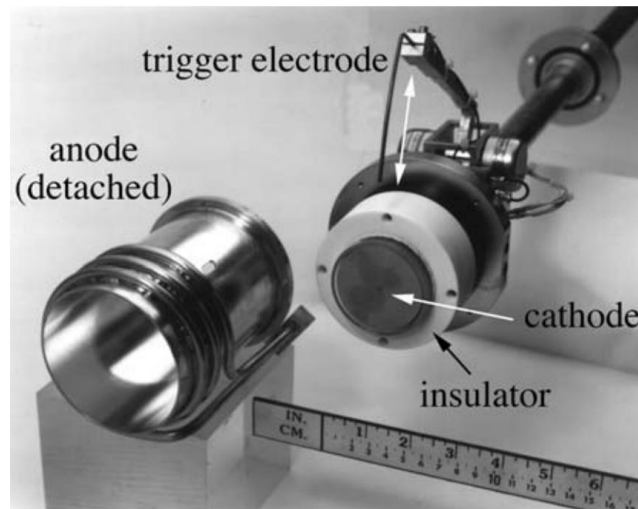


Figure 2-7 The picture of the DC arc source with a mechanical trigger. Here, the trigger is operated by an electromagnetic solenoid. [1]

The pulsed arc ignition has typically a high repetition rate; thus, the mechanical trigger method is not a proper method. There is an alternative method which is a way to use an insulator. The spot ignition starts on the surface of the insulator (Figure 2-8), located between the cathode and anode. The insulator might be coated (silver, carbon, etc.) to obtain a specific resistance (recommended less than $1 \text{ k}\Omega$ [128]). If the insulator has too high a resistance, the current cannot go through the coated insulator, or if the resistance is too low, the current through the insulator without high driving voltage. The current through conducted insulator causes ohmic heating, inducing thermal runaway. This method can be applied to pulsed or DC arc sources, but if the conducting area is eroded, the resistance is increased until the triggering stops.

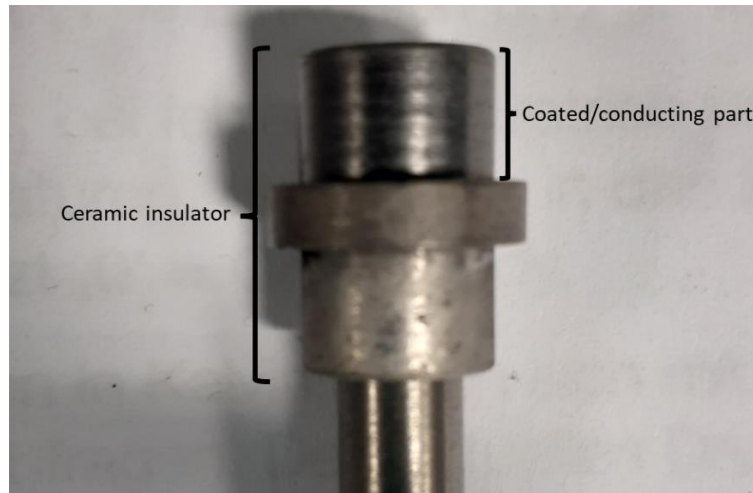


Figure 2-8 Image of carbon coated ceramic piece for arc source (mini gun type). For scale: the diameter of the cathode is 6.25 mm (1/4 inch).

The cathodic arc ignition process

The cathodic arc ignition process (evolution of electron emission and plasma generation process) has several stages (pre-explosion, explosive emission, post-explosion, and final cooldown) [1]. The first stage is the pre-explosion stage. In this stage, the surface of the cathode requires high temperature and enhanced high electric field strength leading to explosive electron emission in the next stage. Two cases are considered to support the specific conditions. The first case is the approach with the initial arc triggering. The arc triggering makes the condition have a high temperature by Joule heating, and it causes thermal runaway. The second case is if the plasma is already generated on the cathode surface, causing thermo-field electron emission. In this case, the plasma affects to subsequent explosion in several ways, such as ion bombardment, causing increase in the temperature of each spot location, and enhancing the high electric field due to the plasma sheath, causing high electric field strength on specific areas, for example, micro- or nano- protrusion of the cathode surface.

The second stage is the explosive emission step which is the main stage of self-maintaining plasma. Here, phase transitions from solid to plasma occur rapidly, and the plasma expands into vacuum. The duration of this stage is characterized by explosive electron emission, which is named the 'ecton' [74], [75]. The explosion induces craters with microvolume on the surface of the cathode, and the explosions are the main reason for fluctuations in the cathodic arc.

The next stage is the post-explosion stage, in which cooldown has begun, but electron emissions from hot surface and evaporation are still significant [4]. Thus, the evaporated liquid metal still spreads into a potential place where a new emission center of the cathode surface may be initiated.

The last stage is the cooldown step, where electron emissions and evaporation of the cathode stop and form micro- or nano- protrusion on the cathode surface. The framework of the fractal model can interpret the spot ignition in the second stage.

2.1.2 Cathodic arc voltage and current characteristics

The first important step for understanding cathodic arcs is to know its voltage-current characteristics. The voltage and current of cathodic arc have fluctuation features because the plasma generation and electron emission explosion occur stochastically with high- and low- frequencies.

Burning voltage and threshold current

The cathodic arc has specific voltage-current characteristics: relatively low voltage and high current. It is distinguishable from magnetron discharge [83]. This voltage is named “burning voltage”, which is the potential difference between anode and cathode [131], and, together with the current, the voltage determines the power dissipation of the cathodic arc [131]. The burning voltage is determined depending on the cathode material, which is correlated to the cohesive energy of the cathode material [131]. This “cohesive energy rule” was well established through the empirical method [131], [132]. The rule is defined as *“The average arc burning voltage of a vacuum arc at a given current is approximately directly proportional to the cohesive energy of the cathode material”* [132] thus the burning voltage approximately linearly increases or decreases depending on the cohesive energy of the cathode material as shown in Figure 2-9.

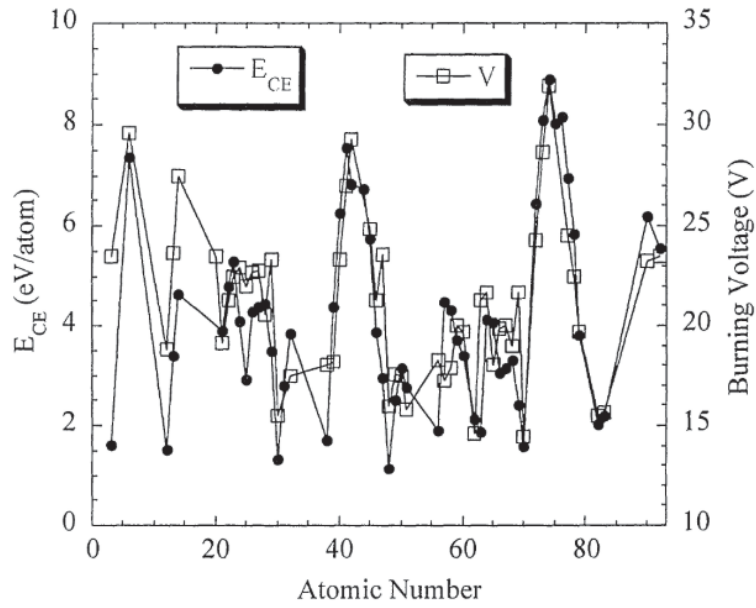


Figure 2-9 Burning voltage (V) and cohesive energy (E_{CE}) as a function of the cathode material of atomic number (Z). The burning voltage was measured at 300 A. [131]

The quantified cohesive energy rule in a first-order is approximately defined by empirical method as [131]

$$V = V_0 + AE_{CE} \quad (2.8)$$

where, V is a burning voltage, V_0 is a base arc voltage, A is an empirical correlation coefficient between the cohesive energy and burning voltage, and E_{ce} is cohesive energy. These values are dependent on the system, for example, $V_0 = 14.3$ V and $A = 1.69$ V/(eV/atom) for “Mevva V” system at Lawrence Berkeley National Laboratory with an applied current is 300 A. If the given current (I) is higher than 1 kA, the burning voltage is significantly changed [133]. For example, the mean burning voltage of Cu is about 20 V at less than 1 kA, but the burning voltage has about two times higher at 6.5 kA of given current [3].

There is a minimum arc current to maintain the cathode spot ignition, which is named as “threshold current”. The threshold current (I_0) is defined [58]

$$I_0 = 0.52 \times 10^{-3} T_b \sqrt{\lambda_T} \quad (2.9)$$

where, T_b is the boiling temperature of cathode material and λ_T is heat conductivity. The threshold current is determined by the combination of boiling temperature and heat conductivity of the cathode materials.

Burning voltage in the presence of external magnetic field

The cathodic arc ignition patterns vary greatly depending on the presence or absence of an external magnetic field around the anode. It is well known that the external magnetic field presence near the anode increases plasma impedance [1], [134], [135]–[137] when the magnetic field is essentially parallel to the anode surface. The phenomena lead to a higher burning voltage being available for ignition, which allows greater power input which implies higher energy for enhanced ionization within the plasma [135]. Therefore, the ion charge state increases finally in the presence of an external magnetic field compared to in the absence of an external magnetic field. The ion charge state distribution of aluminum as a function of the magnetic field strength is shown in Figure 2-10. The ion charge state distribution for Al^{2+} and Al^{3+} are on the rise. In contrast, the ion charge state distribution for Al^+ is the opposite trend of them.

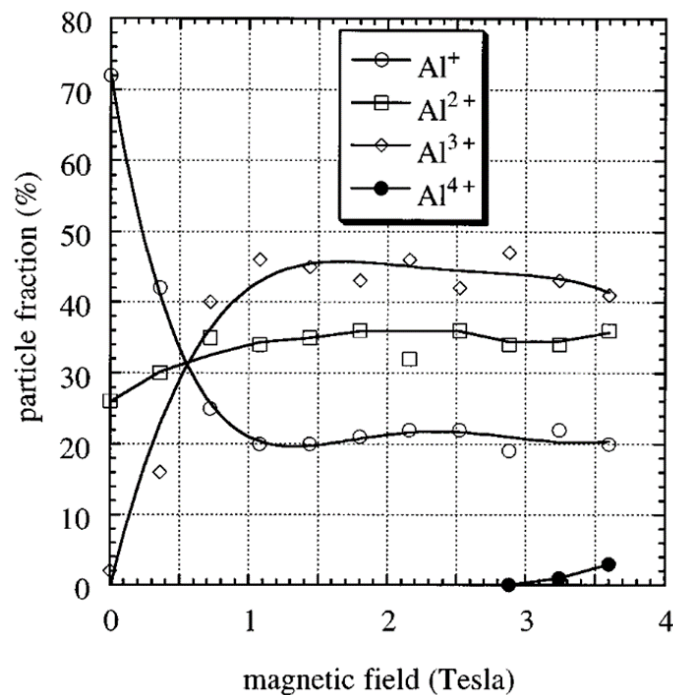


Figure 2-10. Aluminum ion charge state as a function of the magnetic field strength (The plasma source was a broad beam vacuum arc ion source with 30 A, and the magnetic field was generated by a capacitor bank charged up to 20 kV) [138].

2.1.3 Theoretical plasma expansion model

Partial local Saha Equilibrium model

The cathodic arc ignition generates fully ionized plasma [1], [52] in the cathode spot, and the ionized plasma contains a multiply charge state [1], [52], [69], [82] with high energy. The ion charge state is one of the interesting plasma properties which can help to understand the cathode processes and plasma generation [1]. The multiply charged state is changed rapidly from equilibrium (dense plasma, many collisions) to non-equilibrium since the plasma expansion into vacuum ambient, or region of low gas pressure, based on pressure gradient and electron-ion coupling [1], [63], [139]. The plasma expansion was considered by two similar models of transition from equilibrium to non-equilibrium, such as transition from “Local Saha Equilibrium” (the Instantaneous freezing model) and transition from “Partial Local Saha Equilibrium (PLSE)” (the Stepwise freezing model) [70]. They have different assumptions to describe plasma expansion. The Local Saha Equilibrium model assumed that all ion charge state ratios would freeze instantaneously, which means that near the spot states are reaching equilibrium rapidly, almost at the same moment [70], [82]. In contrast to the Local Saha Equilibrium model, the Partial Local Saha Equilibrium model has assumptions that the equilibrium phenomena occur gradually with various ion charge state ratios at different plasma conditions [70]. In practice, charged ion freezing phenomena do not occur instantaneously [70]. Thus, the Partial Local Saha Equilibrium model is closer to reality. It is intuitively obvious that the ion equilibrium phenomena are gradually processed [70]. The process can be described simply, as shown in Figure 2-11.

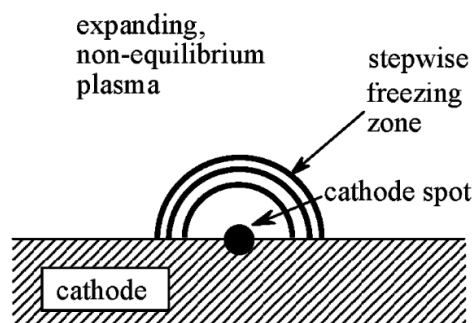


Figure 2-11 Simple illustration of the partial local Saha equilibrium with finite thickness of the step freezing zone [1].

The partial local Saha equilibrium can be explained via the ionization-recombination balance equation, defined follow as [1], [70]

$$\frac{\partial n_Q}{\partial t} = n_{Q+1}n_e^2\alpha_{Q+1,Q} - n_Qn_e\beta_{Q,Q+1} \quad \text{for } Q = 0, \quad (2.10)$$

$$\frac{\partial n_Q}{\partial t} = n_{Q-1}n_e\beta_{Q-1,Q} + n_{Q+1}n_e^2\alpha_{Q+1,Q} - n_Qn_e\beta_{Q,Q+1} - n_Qn_e^2\alpha_{Q,Q-1} \quad \text{for } Q \geq 1, \quad (2.11)$$

where, Q is the charge state number, n_e is the density of free electrons, and n_Q is the density of ions of charge state Q ($Q = 0$ for neutral atoms, $Q = 1$ for singly ionized ions, etc.). α and β are the recombination and ionization coefficients considered independent coefficients with respect to density [140], respectively. The equation (2.11) describes the ionization and recombination balance; the ionization (from $Q-1$) and recombination (from $Q+1$) enhance the ion density of charge state Q , as described by the first two terms, and the other terms explain the decrease by ionization (to $Q+1$) and recombination (to $Q-1$) [70]. Using the Saha equation, the ion charge state distribution of plasma in equilibrium can be calculated as [82]

$$S_Q \equiv n_en_{Q+1}/n_Q = \Lambda_B^{-3} \frac{2\Sigma_{Q+1}(T)}{\Sigma_Q(T)} \exp\left(-\frac{E_Q - \Delta E_Q}{kT}\right), \quad Q = 0, 1, 2, \dots, Q_{max} \quad (2.12)$$

$$\Lambda_B = h/(2\pi m_e kT)^{1/2} \quad (2.13)$$

where, k is the Boltzmann constant, h is the Planck constant, T is the temperature, $\Sigma_Q(T)$ is the temperature-dependent partition function of ions of charge state Q , Λ_B is the thermal de Broglie wavelength, and E_Q is the ionization energy of the Q -fold charged ion. By substituting the Saha equilibrium equation (near the spot) into equation (2.11) and obtaining the following equation (2.14)

$$\Delta t = \frac{\Delta n_Q}{n_Q} \left(\frac{n_e^2}{S_{Q-1}} \beta_{Q-1,Q} + S_Q n_e \alpha_{Q+1,Q} - n_e \beta_{Q,Q+1} - n_e^2 \alpha_{Q,Q-1} \right)^{-1} \quad (2.14)$$

The recombination and ionization can be defined as follows [140]

$$\alpha_{Q,Q-1} \sim (kT)^{-9/2}, \quad \beta_{Q,Q+1}(E_Q, T) \sim \frac{\Sigma_{Q+1}}{g_Q} \exp\left(-\frac{E_Q - \Delta E_Q}{kT}\right) / (kT)^3 \quad (2.15)$$

where, $g_Q = 2J_Q + 1$ is statistical weight [1], the total angular momentum J_Q can be obtained from spectroscopic tables. Through equation (2.14), the characteristic times for ionization and recombination can be estimated. In equation (2.14), the first and fourth terms have an independent relationship with Q , and the second and third terms are proportional to $\exp\left(-\frac{E_Q - \Delta E_Q}{kT}\right)$. According to the equation, the second term has a greater change with respect to energy change than the third term, which means that ions with a high charge state become out of equilibrium sooner than ions with a lower charge state.

The investigation of the charged ions has been done with two different techniques, such as based on Time-of-flight (TOF) [141]–[144] and electrostatic methods [66], [145], [148]–[152]. The two approaches provided different information, for example, the TOF method delivers velocity information, while the electrostatic field method provides energy information [1]. In the case of TOF, techniques showed that the ion velocity is almost independent of the ion charge state, and the electrostatic methods showed that the energy depends to some degree on the charge state [151]. Through the previous results, the ion acceleration mechanism can be described by electron pressure gradient and electron-ion friction [141], [142], [152], which means that the primary ion acceleration does not occur by a hypothetical electrostatic potential hump [148], [153].

The effect of an external magnetic field on the ion charge state was investigated [134]–[138], [154]. In the case of the presence of external magnetic field, the electrons are confined by the external magnetic field, which causes an increase in plasma impedance. The high impedance leads to a high burning voltage to sustain the ignition process, which also implies greater power input and an increase in the ion charge state [1].

Time-resolved techniques for ion energy or charge state distribution were investigated for single-element cathode [155]–[158] and multi-element cathodes [62], [159], [160]. In both single- and multi-element cathode cases, the shift of ion charge state from high to low state was observed. On the other hand, the ion velocity distribution decreased for multi-element cathode cases [62], [160], especially for Nb-Al composition [62]. It is presumed that this is probably because the cohesive energy of the two cathodes is quite different, but no conclusion has been reached.

2.1.4 Types of cathodic arc spots

The spot types 1 and 2

The cathode spots are the primary source of electron emission and plasma formation. The properties of the spots influence all plasma parameters [1]. The spots have two main characteristic spot types, depending on the condition of the cathode surface [161]–[163], such as a contaminated condition [14] and a clean condition [112]. The plasma composition of the cathodic arc is determined by the presence of a contaminated layer or not since the contaminated layer is eroded first, which means the spots ignite on a non-metal area, cleaning until a surface metallic is exposed, and the metal cathode is eroded, [48], [49]. The two main spot types are named “Spot type 1” and “Spot type 2” [112],

respectively. The spot type 1 ignites on contaminated layers, such as an oxide or nitride layer of the cathode surface; thus the spot type 1 always exists initially, whereas spot type 2 appears on a metallic surface [1], which is a chemically clean surface after removing contamination on the cathode surface. Because spot type 1 and spot type 2 have different ignition conditions, there are different characteristic phenomena between them. The spot type 1, which has relatively dim brightness, has higher apparent spot velocity than the spot type 2. This is because that the compound layers on the cathode surface change the work function of the metal surface [164]. And, the lower cathode work function makes the spot motion change [118]. The cathode material erosion of spot type 1 is smaller than erosion of spot type 2; therefore, the ignition process is a little different between spot type 1 and spot type 2.

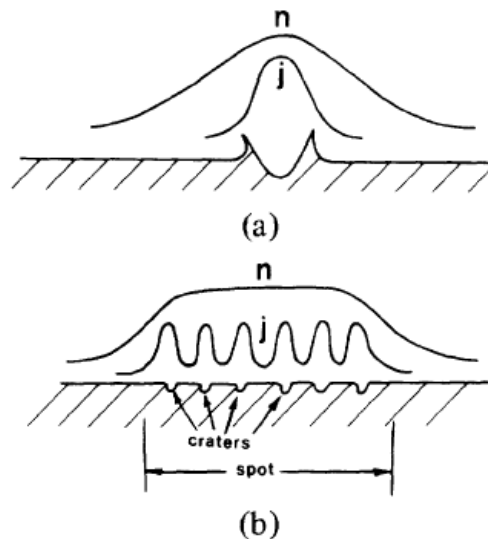


Figure 2-12 (a) Schematic description of arc ignition for spot type 2 (clean surface); (b) schematic description of arc ignition for spot type 1 (contaminated surface); j is a current density, n is a plasma density [162].

In Figure 2-12, the spot ignition is simply portrayed by the distribution of current density (j), and plasma density (n) at one instant. For a clean surface, the arc current and plasma density are concentrated in the one crater area. However, in the case of the contaminated surface, the current and plasma density spread into the distributed small craters on the contaminated thin film, and the current density is shared with each small crater, causing the ignition. Most of the spot is formed on the rim of the eroded area since the sharp rim edge makes it easy to enhance the electric field in that

area, and the thinner contaminated layer is adjacent to the eroded trace origin from the previous spot ignition [14].

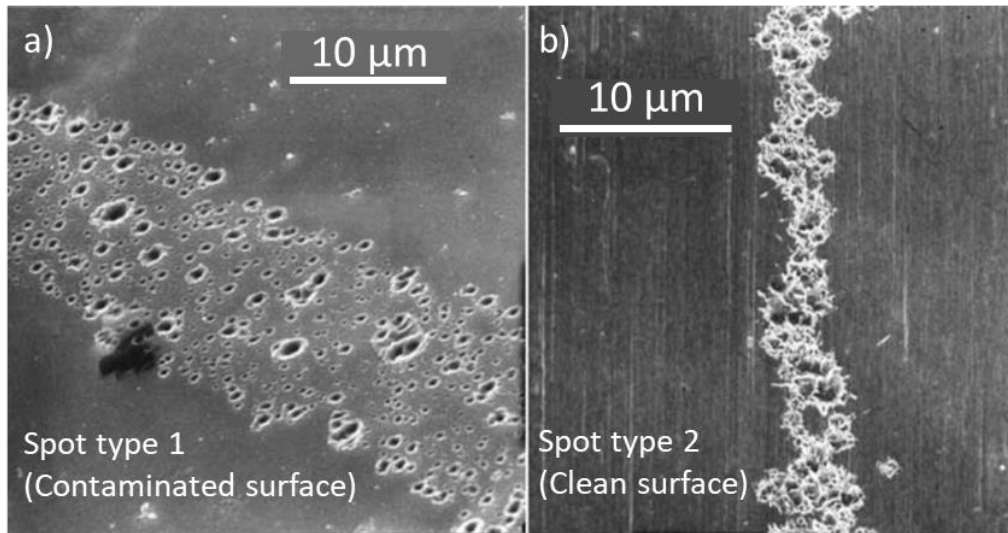


Figure 2-13 (a) The characteristic of craters formed on the cathode surface of spot type 1 (contaminated surface), and (b) spot type 2 (clean surface) [1]. The spot was magnetically steered in both cases.

The spot type 1 and 2 have a rather different pattern of crater appearance. The different characteristics can also be found by “postmortem” examination of the cathode surface because the erosion craters correlate with the arc ignition mechanism (Figure. 2-13) [162]. For spot type 1, it shows a pattern of spot ignition, where the craters are separated from each other (isolated and spread ignition). On the other, spot type 2 has a pattern where ignitions happen adjacent to each other, forming characteristic chains of craters [161]. In general, the pressure dependence of spot type 2 is considered as follows. As the process pressure increased, the fluctuation of burning voltage, chopping current, and current density tend to decrease, while the spot velocity and spot diameter have a trend towards increasing. However, no sharp transition phenomena were found between spot type 1 and spot type 2 [32], which was confirmed experimentally in a pressure range of $10^{-6} - 10^{-5}$ Pa. Also, the cathode spot appears randomly on the clean metal surface; however the randomness of the cathode spot in the temporal distribution decrease on the contaminated surface (oxidized steel surfaces) with an external magnetic field [165]. The phenomenological differences between spot type 1 and spot type 2 are summarized in Table 2.1.

Table 2.1. Phenomenological, qualitative difference between spot type 1 and spot type 2 [1].

	Type 1	Type 2
Surface conditions	Contaminated (i.e., oxide)	Clean (metal)
Apparent brightness	Dim	Bright
Typical crater diameter	Small	Large
Crater appearance	Separate from each other	Adjacent to each other
Apparent spot velocity	High	Low
Cathode erosion rate	Low	High
Relative ease of arc triggering and burning	Easy	Difficult
Chopping current	Low	High
Plasma composition	Metal and gas (hydrogen, oxygen, etc.)	Metal only
Average ion charge state	Low	High
Relative amplitude of fluctuations	Low	High

Recently, a study devoted to the type of spot found that the spot is affected differently depending on the process gas in spot type 2 [34]. The spot behavior was investigated by tracking spot craters formed on a multilayer cathode. The layers play a role as trace makers keeping track of thermal and material displacement effects. Here, repeated spot type switching on the cathode surface was found due to the interplay of cathode surface poisoning, regardless of the gas atmosphere (either N_2 or O_2). The ignition of spot type 1 was observed significantly more in the case of O_2 than in the case of N_2 because the layer formed between the cathode material (titanium) and O_2 is more thermodynamically stable than the layer formed between N_2 and the cathode material. Further, in the N_2 atmosphere, a greater number of deep craters was found than in the O_2 atmosphere [34].

The spot type 3

There is type named “spot type 3” [1]. The spot type 1 and spot type 2 are considered on metal cathodic surfaces with sufficient conductivity to carry the arc current. However, if the conductivity is not enough like in metals, such as in highly conducting semiconductors and semi-metals, the spots have quite different pattern compared to “spot type 1” and “spot type 2”. In the case of B_4C [166], the spots ignited on the same location of the cathode surface for its whole ignition period, instead of a specific direction of moving, which left deep spot crater on the cathode surface. For graphite [167], cathode spots on the surface showed a very short range of motion compared to those on the metal cathode surface. The spot velocity was determined by characterization of such material properties, as grain size, pore size, and electrical resistivity [168]. The behavior of cathode spot on graphite in vacuum arc was described with a model of near-electron processes, which explained the spot

parameters as a function of a spot lifetime, and the parameter strongly affected at spot lifetime shorter than $10\text{ }\mu\text{s}$ [169].

2.1.5 Cathodic arc spot motion in a magnetic field

Random walk motion

The cathodic arc spot is typically shown with the type of emitted tiny spot, a sequential action on the cathode surface with microscopic explosions. During the sequential process, variable energy exchange occurs between the cathode spot and the cathode surface; therefore, an apt description of spot motion is required to deeply understand the process [9]. The sequence of emitted tiny spots occurs at different positions within a short time. Therefore, the sequential process appears to have motion [1]; however, the spots do not move. The term “spot motion” thus reflects the sequential plasma ignition and extinction phenomena.

The spots have different trends of motion in the absence [9]–[13] of a magnetic field and the presence [14], [15], [16], [17], [18]–[25], [50], [171] of a magnetic field. If there is no external magnetic field, the cathodic arc spots have “Random walk motion” [9]–[13]. The random walk motion has no memory effect on spot ignitions; thus, the spot ignition occurs stochastically. This process also is called a “Markov process” [171]. The random walk motion is simply described in Figure 2-14.

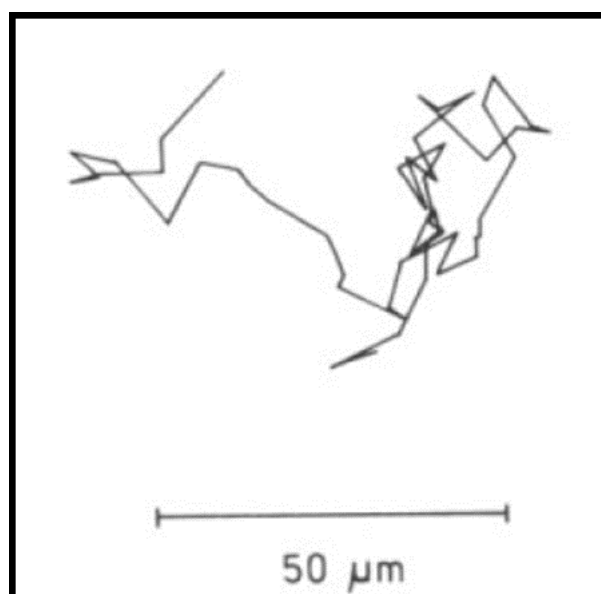


Figure 2-14 Schematic image for random path of a cathode arc spot [172].

The random walk motion could be described by a probabilistic approach, leading to a Rayleigh distribution. The probability $P(R)$ assumes that the probability of cathode spot position is in the range $(R, R + dR)$ after t [1], [9].

$$P(R)dR = \frac{R}{2Dt} \exp\left(-\frac{R^2}{4Dt}\right) dR \text{ for } t \gg \tau \quad (2.16)$$

where, D is the diffusion constant. The diffusion constant has different value depending on the material. For example, $D = (2.3 \pm 0.6) \times 10^{-3} \text{m}^2/\text{s}$ for copper [12], $D \approx 10^{-3} \text{m}^2/\text{s}$ for molybdenum [173], and aluminum has $D \approx 1.4 \times 10^{-3} \text{m}^2/\text{s}$ [9].

$$D = \frac{1}{4} \frac{s^2}{\tau} \quad (2.17)$$

Here, each displacement is considered in a small element step, s , which takes an average elementary time τ [1], and the mean value of displacement is [1], [9]

$$\langle R \rangle = \frac{s}{2} \sqrt{\pi \frac{t}{\tau}} \quad (2.18)$$

The apparent spot velocity is [1]

$$v_{spot} = \frac{d\langle R \rangle}{dt} = \frac{1}{2} \sqrt{\frac{\pi D}{t}} = \frac{s}{4} \sqrt{\frac{\pi}{t\tau}} \quad (2.19)$$

According to equation 2.19, the average spot velocity is influenced by the observation time, t . This is one of the characteristics of the random nature of motion. The average spot velocity is a qualitative measure of random motion therefore the velocity is not in the classical sense which is like the normal time derivative [1], [9].

Retrograde motion

Suppose the external magnetic field exists near the cathode spot in transverse direction. In that case, the cathode spot is magnetically steered in one direction which is named retrograde motion [117] instead of the “Random walk motion”. The retrograde motion can be expressed as a vector as $-\mathbf{j} \times \mathbf{B}$, \mathbf{j} and \mathbf{B} are the current density and magnetic flux density vectors, respectively. In general, the charged particle follows Lorentz force [174] in the electromagnetic field. The charged particle moves along the

$\mathbf{j} \times \mathbf{B}$ direction, which is called the Amperian direction; however, in this case the cathodic arc spot moves along in the opposite direction. The retrograde direction means the “opposite” direction of the Amperian direction ($\mathbf{j} \times \mathbf{B}$). The motion of the cathodic arc spot is related to the probability of reignition. The reignition occurs at the specific location of the cathode surface with anisotropy of azimuthal distribution probability.

The retrograde motion was investigated experimentally [15]–[22], [53], [54] theoretically [23]–[25], [170], in various ways. However, no theory can cover all the observations qualitatively and quantitatively [21], [24]. The control of cathodic arc spot motion was studied systematically with a designed circular transverse magnetic field on graphite and copper cathode surface. It showed that the arc stability was improved with increasing arc current [16]. The cathode spot velocity depended on magnetic field strength and arc current. The spot velocity increased proportionally to magnetic field strength and arc current [20], and the cathode material [23]. For the investigation of cathode spot motion, a roof-shaped configuration of the cathode was used with an external magnetic field, and the cathode spot showed different motions on the slope (random motion) and the roof (retrograde motion), respectively [22]. According to the results, the speed of cathode spot rotational motion is influenced by the parallel magnetic field component. In contrast, the perpendicular magnetic field leads spots to drift in the radial direction [18].

Recently, a theoretical study [24] has been conducted with three different theoretical approaches such as “effect of magnetic field on the spot given hydrodynamic process”, “effect of magnetic field on the motion of ions”, and “effect of magnetic field on the motion of emitted electrons”. From the investigation, no specific correlation was found that the magnetic field is affecting the formation of liquid-metal jet and the droplet detachment. Also, it was found that the ion motion in the near-cathode space-charge sheath is not directly affected by the magnetic field, but only emitted electrons are confined magnetically. Therefore, the fundamental understanding is still missing. The basic phenomena for the cathode spot motion can be described by the empirical model, which is named the Jüttner-Kleberg model [15], as shown in Figure 2-15(a). The model describes that the retrograde motion is determined by plasma jets because the jet increases the space charge at a potential new emission center [15]. Also, the motion has a “zigzag” ignition characteristic. Figure 2-15 shows (a) the simple zigzag ignition characteristic on the cathode surface and (b) the cathode surface photographed after ignitions.

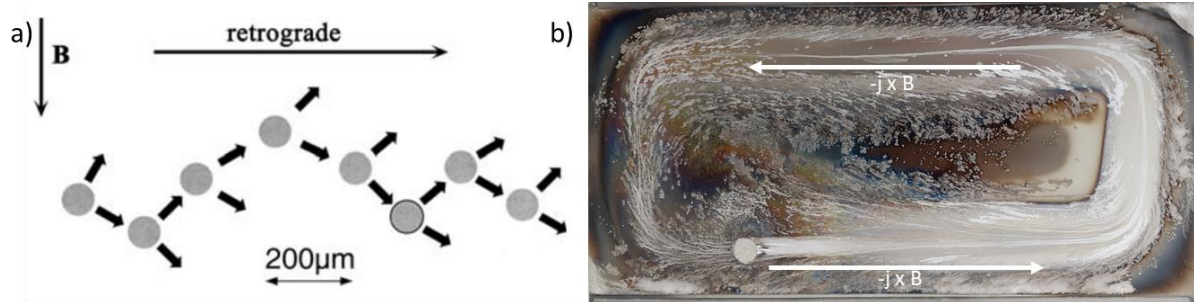


Figure 2-15 (a) Depicted cathode spot motion; the cathode spot has retrograde motion ($-\mathbf{j} \times \mathbf{B}$) with “zigzag” ignition characteristic as shown in a). b) is an aluminum cathode surface for linear magnetron, after arc process. Here, the erosion area followed the retrograde direction with “zigzag” ignition.

2.1.6 Fractal spot model

The cathodic arc ignition is a fluctuating process which is associated with the non-linear explosive nature of cathode spots on the cathode surface [1], [39], [69], [70]. During the process, a bunch of electrons is released explosively, and the electron emission is related to the generation of plasma at the electron emission center [77]. The electron emission occurs under conditions of high spot temperature and strong electric fields, resulting in unstable (non-stationary) conditions accompanied by microscopic explosions of less than 100 ns [51]. The fractals are a well-known theory to explain fundamental nature phenomena [171], [175]. The fractals have a feature which is called self-similarity. The self-similarity is unvaried to scaling; thus, the self-similar object, as shown in Figure 2-16, appears to have a non-changing pattern at different measurement scales, temporally and spatially [1], [171], [175], [176].

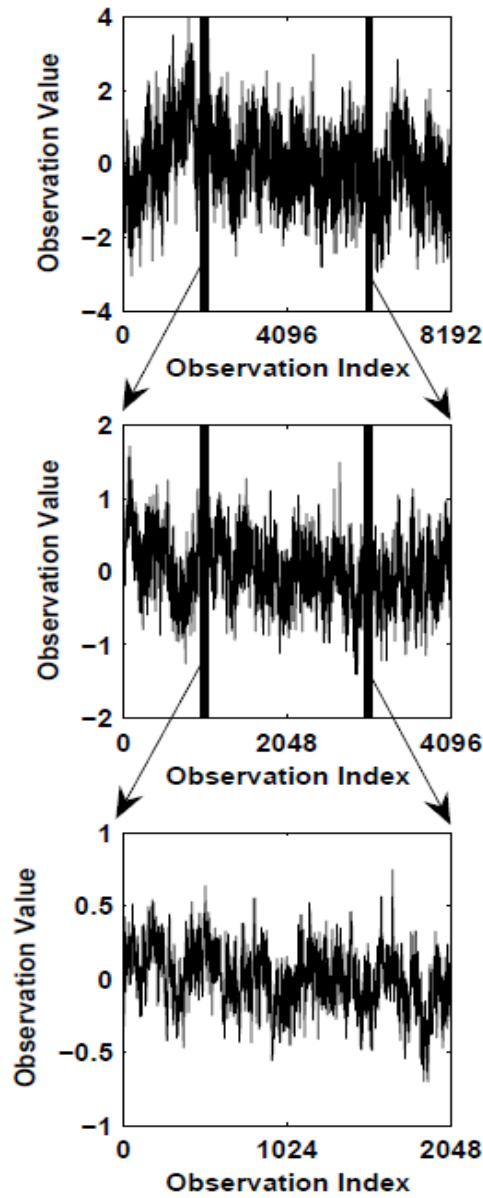


Figure 2-16 Example plot of depicted self-similarity; the second plot zooms in on a range of the observation index in the first plot, and the third one zooms in on a range of the observation index in the second plot. Each depicted plot has the same fluctuation which looks the same as the original one even though they are at different observation scales [176].

The self-similarity could also be discrete or continuous, deterministic or probabilistic, and can be expressed by a power law [1], [171]. The fractal physical phenomena can be defined by power laws as [1], [53], [54]

$$F(f) \sim 1/f^\alpha \quad (2.20)$$

where f is the frequency and α is the so-called colored random noise (CRN) index which has different values depending on the physical phenomena, such as “white noise” for $\alpha = 0$, “pink noise” for $\alpha = 1$, “brown noise” for $\alpha = 2$, and “black noise” for $\alpha > 2$ which is observed in self-similar systems with strong feedback [1], [39], [177], [178]. The self-similarity can be analyzed by fast Fourier transformation (FFT) that can be fitted to a power law equation (2.20). If there exist periodic events during physical phenomena, the FFT should show specific peak values corresponding to such periodic events.

The fractal features were observed through several experiments related to the cathodic arc. The self-similarity of cathodic arc spot was investigated by observing directly with optical emission photography method and spot crater after ignition with a scanning electron microscope (SEM) [179]. The results showed the self-similarity over three orders of magnitude in spatial resolution. The high-frequency fluctuations of the burning voltages of various cathode materials (W, Ta, Hf, Ti, Ni, Au, Sn, Bi) have been investigated by the fast Fourier transformation (FFT), yielding a power spectral density that correlates with the burning voltage of cathode material [68]. The measured voltage noise can be interpreted by power spectral density with a slope of 2 (CRN index) which means a Brown noise [68]. The spectral power intensity has a trend increasing with higher cohesive energy [68], [180]. The current fluctuations of cathodic arc also have been investigated with high analog bandwidth (up to 1 GHz) and fast digital sampling (up to 5 Gsamples/s) device [71], as shown in Figure 2-17. The results show that the microscopic explosions represent the cutoff at the high-frequency end for the fractal model of cathodic arcs [71]. The fluctuation of voltage [68] and current [71] data showed high-frequency peaks over 100 MHz or near 100 MHz, respectively; however, it was not concluded whether the peaks are real because the peaks could be artificial signals coming from the measuring circuit as a resonance [68].

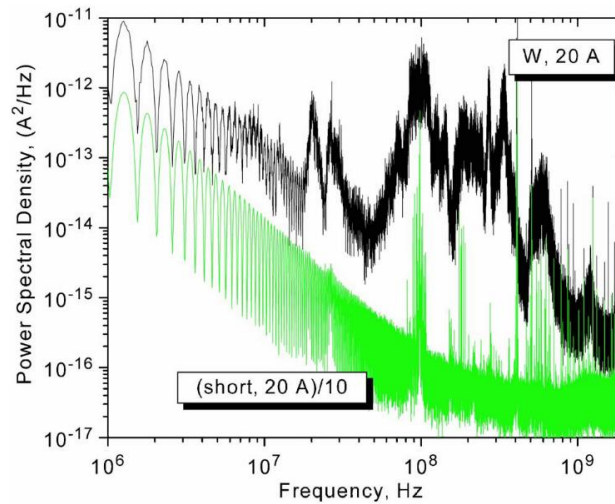


Figure 2-17 The example graph of the power spectral density of current fluctuations, obtained by FFT. The applied current was 20 A in both cases. For better visualization, the short-circuit data were divided by 10 [71].

The arcing phenomenon may occur under various circumstances. To understand that arcing occurs on solar arrays in satellites, experiments of arcing detection have been carried out [181]. The arcing signal was measured with a Yagi antenna. The data from the satellites showed several specific peaks in the spectral graph, especially in the range 300 ~ 350 MHz. However, it was concluded that observed peaks are not correlated with the arc ignition through the reproduced experiments in the lab. It could be assumed that it is occurring artificially during the sampling stages. This conclusion could be one of the pieces of evidence that the arc process has a fractal nature, with the absence of characteristic frequencies.

2.2 Film deposition

2.2.1 Energetic deposition

Thin films and coatings are applied in almost every aspect of modern life, implying a rich field of research and applications. The properties of films are affected by the deposited material, their structure, the deposition process parameters, and the conditions of the surface of a growing film [1]. In the current chapter, the case of the energetic deposition process, in which a significant fraction of particles arriving at the deposition surface has high kinetic and potential energies, is considered (about 10 eV and more significant) [182]. The energetic particle fraction can be produced by several proper

methods. For example, ion-beam assisted deposition [183], magnetron sputtering [184], pulsed laser deposition [185], and cathodic arc deposition [182]. Those several methods can generate energetic deposition conditions at the surface during the film growth.

The energetic deposition process leads to many effects on the film growth, such as increasing intermixing layer, which improves adhesion, enhancing nucleation, and changing film morphology and microstructure (increasing surface mobility) [182], [186], [187]. These physical phenomena are related to ions arriving at the substrate surface with a certain amount of kinetic and potential energy in the energetic deposition process. The bunch of ion energy arriving at the substrate usually has higher values than the binding energy, surface binding energy, and activation energy for surface diffusion. Therefore, both kinetic and potential energy of ions can be expected to have a substantial effect on film growth [1], [42], and both kinetic and potential energy of ions contribute to what can be named atomic-scale heating (ASH) [42]. The ASH process can be described as thermal energy transfer by thermal conduction in atomic-scale volume during the collision cascade with the loss rate of kinetic energy on the order of 100 eV/nm (subplantation). At that moment, the thermal spike occurs only in a small number of atoms [42], [182]. Typically, the energetic deposition only considers the effect of ion kinetic energy [43]–[45]. However, ions have significant potential energy in the case of cathodic arc techniques; thus the films formed by the energetic deposition process may owe some of their properties not only to the kinetic energy of ions but also to their potential energy [42].

2.2.2 Ion kinetic and potential energies

The kinetic and potential energies of ions are explicitly taken into consideration in the extended structural zone diagram [47], which gives an overview of their effect on the structure of thin films.

The ion kinetic energy

The effect of ion kinetic energy on grown film structure was introduced indirectly by the “classic” structure zone diagram (SZD) [188]. The classic SZD only considers the effect of substrate heating and ion kinetic energy on film growth. In contrast to classic SZD, an extended SZD considers the ion kinetic, potential energy effects, and net film thickness (t^*) [47]. Two main parameters govern the film structure properties, namely the generalized temperature (T^*), which includes the effect of potential energy of particles arriving at the surface [47], and normalized energy (E^*) which is correlated with kinetic energy of bombarding particles [47]. The extended SZD is shown in Figure 2-18. The cathodic

arc plasma sources are characterized by high ionization of metal plasma which is sometimes affected by “pressure ionization” due to the high pressure in the spot, causing the formation of multiply charged ions [52]. These multiply charged ions expand from the emission site to a vacuum or low-pressure gas medium with high kinetic and potential energy.

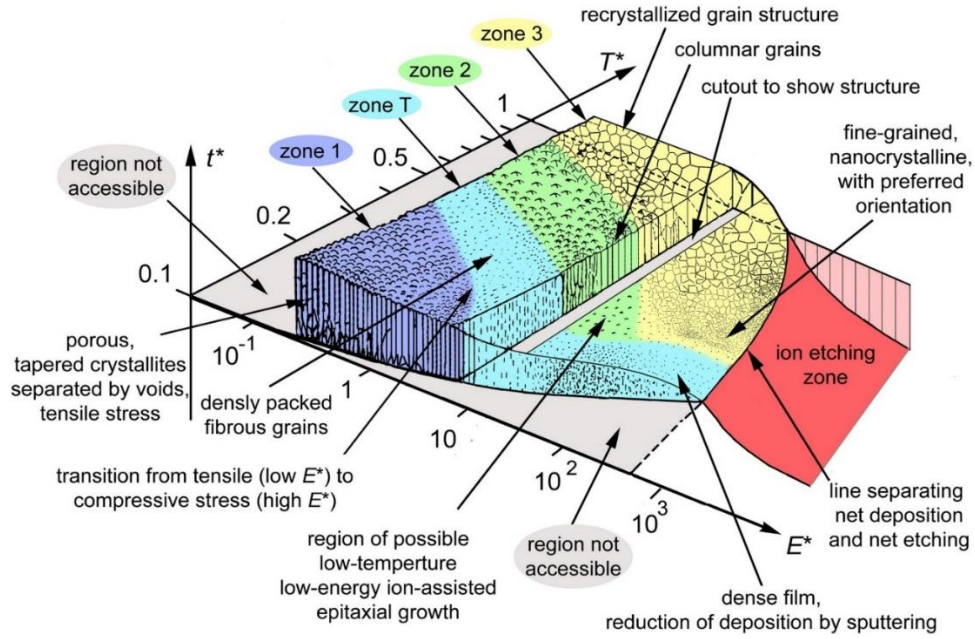


Figure 2-18 The extended structure zone diagram which are described by the generalized temperature (T^*) and normalized kinetic energy (E^*) [47].

The kinetic energy of ions consists of three main elements: the initial energy, which is caused by the explosion ignition process, a term given by charge state and sheath voltage to the substrate, and a term due to image charge acceleration; thus, the kinetic energy of arriving on substrate can be described as [42]

$$E_{kin} = E_0 + QeV_{sheath} + E_{ic} \quad (2.21)$$

where E_0 is initial kinetic energy from plasma, Q is the ion charge state number, e is the elementary charge, E_{ic} is ion kinetic energy by image charge acceleration, and V_{sheath} is the voltage drop between plasma and substrate surface (biasing voltage) [47]. The kinetic energy by image charge acceleration (E_{ic}) could be often ignored because it is a small amount of energy, and it is enhanced the total kinetic energy at the substrate surface only slightly. The initial kinetic energy and ion charge state can be determined by the burning voltage and the cohesive energy of the cathode material [132]. The burning voltage is also correlated with the external magnetic field [134]. If an external magnetic field is

essentially parallel to the anode surface, the electron coming from the cathode material is magnetized perpendicular to the external magnetic field lines before reaching the anode but hindered to reach the anode. The electrons require more energy to escape from the hindering external magnetic field toward the anode. This “magnetic insulation” phenomenon leads to the higher burning voltage which causes greater power input, higher electron temperature, higher pressure gradients from the spot, and finally, higher kinetic energy at a given constant current [1], [134]. The kinetic energy of ions increases proportionally with the external magnetic field strength [134].

The effect of ion kinetic energy has been investigated extensively through theoretical and experimental approaches. The effect of ion kinetic energy is also considered in terms of the background pressure [188]. This is because the collisions affected by the process pressure determine the ion kinetic energy before the ion arrives at the substrate.

The effect of ion kinetic energy by tuning biasing voltage has been shown through the structural properties of the deposited film. The biasing is usually set up with negative polarity to accelerate positive ions and repel electrons. The grain size was decreased with increasing substrate bias voltage for TiAlN [43]. The higher substrate bias voltage affected the microstructure formation, which significantly contributed to the formation and stabilization of the metastable phase [44]. Film stress and morphology also were shown to be affected by turning the bias voltage [45]. The effect of pulsed biasing [45], [189]–[196] on the substrate was investigated. Using the pulsed biasing of the substrate provides advantages, such as lowering the substrate temperature [191]–[193], reducing macroparticle attachment compared to typical DC bias [189], [194]–[196], and supporting precise control with tuning of peak pulse duty cycle [190], [194], because the ions only gain energy in the pulse-on period.

The ion potential energy

The potential energy of ions arriving on the surface can be expressed by the following equation:

$$E(Q) = E_{exc} + E_C + E_i \quad (2.22)$$

where E_{exc} is the excitation energy of bound electron if an excited state. E_{exc} could often be neglected [1] because the excitation energy only give influence in the dense plasma region; E_C is the cohesive energy, and the ionization energy (cumulative ionization energy) is given by $E_i = \sum_{Q'=0}^{Q-1} E_{Q'}$. The ionization energy is the primary contribution to the potential energy, and the energy is defined as the energy required to pull out the bound electrons when forming ions [1], [197]–[199]. Therefore, the ionization energy is cumulative ionization energy of all ionization steps. The contribution of the

ionization energy is the largest part of energy to the ion potential energy especially, in highly ionized plasma like the cathodic arc plasma. The cohesive energy and the cumulative ionization energy are listed in Table 2.2.

Table 2.2 List of cohesive energy, and cumulative ionization energies for aluminum, titanium, and vanadium [1].

	Cohesive energy [eV/atom]	Cumulative ionization energy [eV]		
		E_0	E_1	E_2
Al	3.39	5.99	24.8	53.3
Ti	4.85	6.83	20.6	48.1
V	5.31	6.75	23.3	50.7

The effect of ion potential energy has been investigated by the ion beam irradiation method [200]. The energetic deposition by heavy ions has been performed with slow multi-charged ions to demonstrate the contribution of ion potential energy by comparing Hillock formation and surface roughness of CaF_2 [200]. The Hillock formation and slow multi-charge ions have quite high charge states and huge energies but the ion potential energy effect in a typical cathodic arc range still is not well investigated.

Molecular dynamics (MD) simulations are a proper approach to understanding the contribution of atomistic mechanisms in various physical vapor deposition [201], [202]. Recently, the role of ion potential energy was considered in low energy high-power impulse magnetron sputtering (HiPIMS) deposition using molecular dynamics simulation [203]. The effect of ion potential energy was shown that some features such as a slightly lower interface mixing, and fewer point defects are found. However, resputtering and twinning have increased slightly in the final structure. According to the previous theoretical study [203], the ion potential energy affects film formation in a very short interatomic distance, which means ion potential energy effect is very localized; however, in the case of highly ionized plasma, it is still required to consider ion potential energy.

3. High-resolution observations of cathode spots with a streak camera

3.1 The concept of observing of cathode spots

Observing cathode spot ignition is not easy since the spot size is tiny (μm), and the ignition and extinction events occur rapidly at different positions. Therefore, it is required to use a proper method to investigate the cathodic arc spots and its fluctuations. In the current chapter, two main concepts in terms of the experiment are considered to observe the cathodic arc spots properly. The first concept concerns an experimental device. In order to investigate cathode spots effectively, a linear magnetron was used as an arc source. This setup allows us to enhance the possibility of observing the cathode spots since the light emission from a given spot is based on the ignition and extinction events which occur along the straight section of the racetrack on the cathode surface. The second concept is the approach to the plasma diagnostics. The ignition and extinction events of the spot have very short characteristic time. Thus, the streak camera coupled to a long-distance microscope is used to catch the tiny, bright mobile spots with a short specific time. The apparent motion (ignition and extinction sequences) of the cathode spot can be investigated by using the streak camera in which the entrance slit is projected onto the spot ignition and propagation region. In addition, the question of whether a fractal model is adequate for operating the cathodic arcs can be investigated as well.

3.2 Plasma diagnostics

3.2.1 High resolution streak camera observations

The streak camera is a device to observe ultra-fast light phenomena as a function of time [204]. Unlike fast framing cameras, the streak camera can allow observing the evolution of a process without interruption within selected sweep time. The streak camera produces time-space (x, t) images, as opposed to space-space (x, y) images of a conventional fast framing camera [205].

The operation principle of the streak camera is shown in Figure 3-1. The emitted light coming from the source with different delays and intensities passes through a slit that is tunable by a user. After passing the slit, the emitted light hits the photocathode, where the electron converts sequentially into a number of electrons proportional to the intensity of light. At that time, the converted electrons have

a different incident timing since the photon has an incident time delay from the source. The converted electrons from the photon with different incident timing fly into a micro-channel plate (MCP), where the signal intensity is enhanced. Before reaching the MCP, the electrons are manipulated by a high voltage at the sweep electrode to synchronize the timing of incident light. The electrons from MCP strike the phosphor screen, where the electrons are converted again into photons like the image on the phosphor screen. The image on the phosphor screen that corresponds to the source that arrived first is placed in the uppermost position, with the other images arranged from top to bottom in sequential order [204].

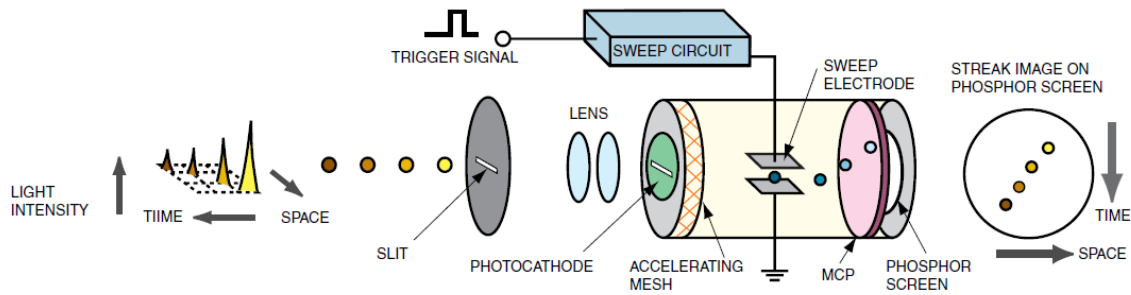


Figure 3-1 The schematic of simple illustration of a streak camera for operating mechanism [204].

An example of a streak image can be shown in Figure 3-2. The streak image consists of two axes; temporal (time dimension) and spatial (direction dimension) axis. Therefore, the streak image allows us to investigate the movement of light-emitting plasma in one direction. The temporal axis can be changed depending on the selected sweep time. For example, if the sweep time is selected 10 ns, then the whole temporal axis has 10 ns observation time, or if the sweep time is selected 10 μ s, then the whole investigation time is 10 μ s. Therefore, the temporal resolution at a given pixel is changed because the total observation time is varied.

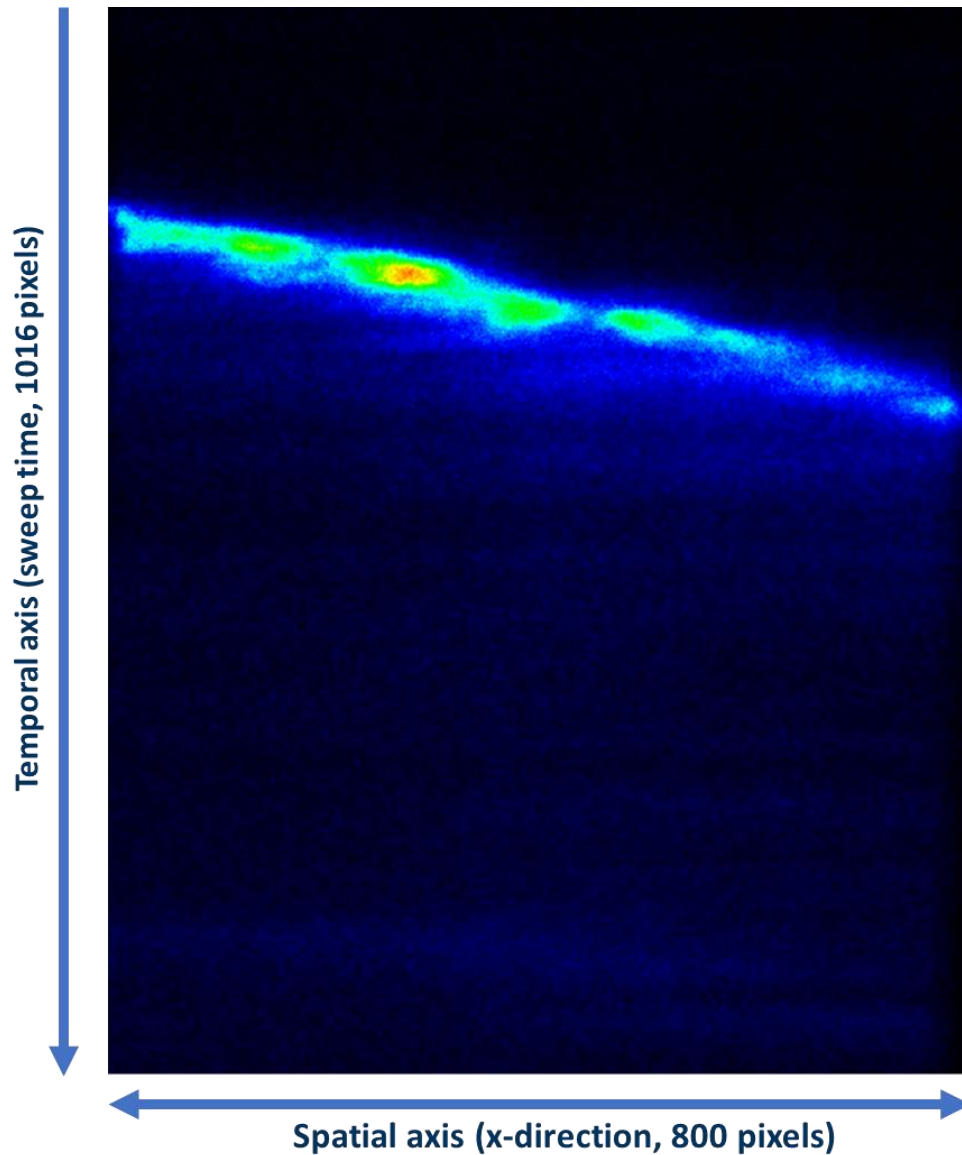


Figure 3-2 Example of streak image (800 X 1016 pixels). X-axis is a spatial dimension and Y-axis is a temporal dimension. This sample has 50 μm observation time (sweep time of this example). The spatial resolution was 1 $\mu\text{m}/\text{pixel}$ (The applied arc current was 750 A).

The applied objective lens determines the spatial resolution; however, the temporal resolution can be adjusted differently by the selected sweep time and slit width (the wider slit, the more light it can receive, but the lower the resolution). The temporal resolution is defined as the full width at half maximum of the intensity of light pulse imaged on a phosphor screen [204]. The theoretical temporal resolution is estimated and shown in Table 3-1.

Table 3-1. Theoretical estimated temporal resolution (with slit width 20 μm) for a streak camera (model C13410 by Hamamatsu).

Selected sweep time	Real sweep time	Theoretical temporal resolution [ns/slit]
10 ns	9.9 ns	0.043
20 ns	19.6 ns	0.085
50 ns	46.3 ns	0.201
100 ns	91.6 ns	0.398
200 ns	211 ns	0.868
500 ns	507 ns	2.2
1 μs	0.986 μs	4.28
2 μs	1.97 μs	8.55
5 μs	4.85 μs	21.06
10 μs	10.0 μs	43.44
20 μs	20.2 μs	87.74
50 μs	49.7 μs	215.87
100 μs	99.1 μs	430.44
200 μs	198 μs	860

The streak camera has been widely used to investigate plasma [20], [53], [54], [60], [172], [206]. For investigation of cathodic spot displacement, setup consisting of combinations of fast framing and streak cameras were used. The spot size categorized the spot structure and the spot displacement was described by cyclic extinction and formation [60] but the cyclic process could not be exactly defined because the process occurred in a broad range of characteristic times (formation time < 50 ns and residence times < 100 ns). The brightness distribution of the cathode spot was investigated by streak camera and framing camera with different exposure times, and the model for determining the brightness distribution of the cathode spot was developed. The spot diameter differed depending on the measuring techniques since the spot with very fast motion gave a broad brightness distribution profile [172]. The cathode spot velocity was measured with a streak camera in a high transverse magnetic field, and the spot velocity depended on magnetic field strength and arc current [20]. A streak camera coupled with a spectrograph was used to investigate time-resolved spectra of cathode spots [206].

In this thesis, the streak camera coupled to a long-distance microscope was used to capture the cathodic arc spot. The system allowed us to observe cathodic arc spots with high-temporal and spatial resolutions. The observed results will be handled in chapter 3.4.

3.2.2 Optical emission spectroscopy

The cathode spots contain tiny mobile luminous areas in spot center, and the spot ignition event happens stochastically, and explosively [72]–[79], [207] within a very short time (nanosecond time scale) [1], [51], [71]. Due to these facts, it is not easy to observe the plasma in practice during the ignition process, and the plasma has non-uniform and strong parameters fluctuations [73]–[76], [208]. In general, when the cathodic arc discharge occurs, it emits electromagnetic radiation from the plasma [209], and the electromagnetic radiation gives us information about the plasma processes and parameters [210]. Electromagnetic radiation commonly has a wide range of wavelengths (the wavelength composition of light), from radio waves (kilometer) down to gamma-rays (picometer) [210]. However, the arc spectrum extends practically only to the vacuum ultraviolet (VUV) region. From the experiment point of view, understanding this wavelength region is a practical consideration since some wavelength range is required for specific optical accessories which can transmit specific wavelengths. For example, quartz windows can be applied from 200 nm, but they cannot be used in the less than 200 nm range; in case of less than 200 nm, it is necessary to use a vacuum ultraviolet (VUV) system since the VUV radiation (10 - 200 nm wavelength range) is rapidly absorbed in the air [211]. Also it is required to use magnesium fluoride optics for proper transmission [212], [213].

The electromagnetic radiation can be analyzed in two types of measurements: the passive method of emission spectroscopy and the active method of absorption spectroscopy [210], as depicted in Figure 3-3.

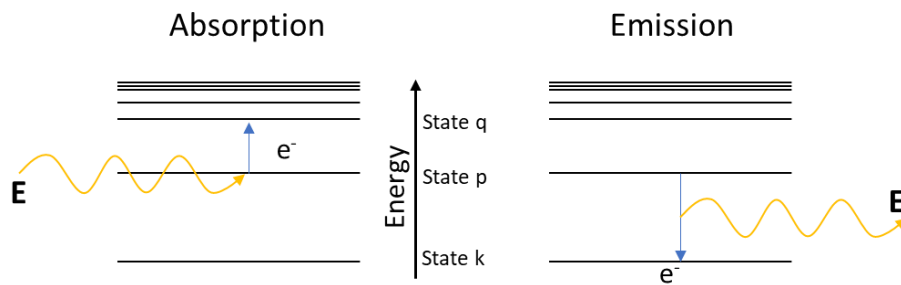


Figure 3-3 Simple description of atomic absorption and emission in excited and ground states

The optical transition in atoms occurs when electrons in the atom move from one energy level to another. For example, the excitation of an atom by electron impact may be followed by a decay from level p to level k with spontaneous emission of a photon with the transition probability A_{pk} [210]. In this process, the energy E_p has a higher value than the energy E_k . In the case of absorption spectroscopy, the excitation from p to q level takes place by absorption of a photon with the transition probability B_{pq} [210]. In this process, the energy value, E_q is higher than the energy value E_p .

The optical emission occurs in the form of line emission with a specific wavelength, which can be defined by the following equation [214]

$$\lambda = hc / (E_p - E_k) \quad (3.1)$$

where E_p is the energy on the level p , E_k is the energy on the level k , h is the Planck's constant, c is the speed of the light, and λ is the central wavelength of line emission, which has the photon energy corresponding to the energy transition from level p to k .

The basic spectroscopic system consists of the entrance and exit slit, the grating as the dispersive element spatially, and the detector [210]. The tuning of the slit width can manipulate the signal intensity and spectral resolution. If the slit has a larger entrance slit, the signal intensity is higher, but the spectral resolution is reduced, therefore a size of the entrance slit is quite an important factor. The grating is classified into mainly two types according to groove patterns which are produced by the mechanical ruling (using a diamond) and interference methods (to form fringe patterns using laser beams for holographic patterning) [213]. The grating has different diffraction efficiency as a function of wavelength. The diffraction efficiency of maximum is about 70 ~ 80 % at λ_B (blaze wavelength), and the valid range of a grating is approximately in the range $\lambda_B/2 \leq \lambda \leq 2\lambda_B$ [213]. The example of the diffraction efficiency graph of IsoPlane SCT 320 grating is shown in Figure 3-4. The diffraction efficiency was used to correct the spectral sensitivity.

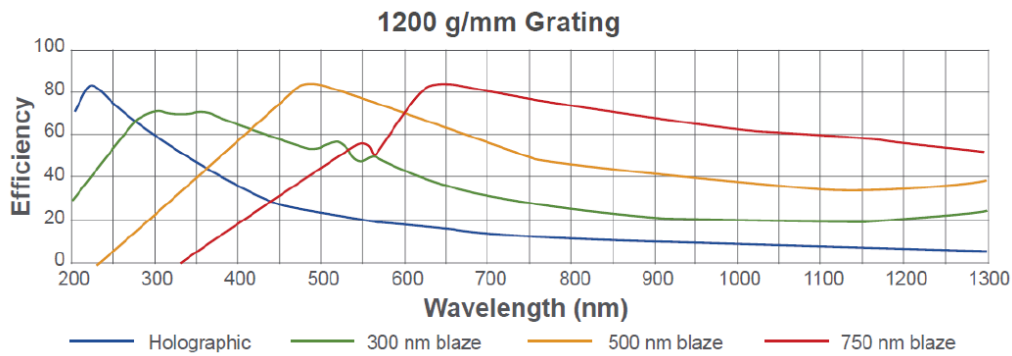


Figure 3-4 The example of an efficiency graph of a diffraction grating of 1200 grooves per millimeter used in IsoPlane SCT 320 spectrometer as a function of wavelength at three different blazed at 300 nm, 500 nm, 750 nm, and holographic case [215].

Optical emission spectroscopy (OES) is a suitable technique to analyze plasma since this allows for species identification by the non-intrusive *in situ* diagnostic method [216]. Many previous investigations already have been done for the cathodic arc plasma analysis [206], [217]–[221]. OES was applied to identify emission species from the spot [217]. The arc behavior between Cu-Cr electrodes was investigated by spatially resolved OES at high-current conditions and found difference in intensity between atomic and ionic lines [218]. Time-resolved analysis was performed for Ga-In alloy cathode [219], and temporal and spatial analysis was done for Ga-In alloy cathode [206]. The OES was applied to compare and analyze emission spectra between vacuum arc and rf-discharge [220], and it was used to identify species for pulsed cathodic arc [221]. The most straightforward case of optical emission spectroscopy analysis is the identification of particle species (atoms, ions, molecules) in the plasma [210]. The identification of the particle species is provided by the spectrum because the radiation wavelength is a fingerprint of an element. The wavelength and transition probabilities of atoms and ions can be obtained in the NIST database [222]. In this thesis, the optical emission spectroscopy was used to identify the main species generated by vacuum arc ignition. It made it possible to confirm the ultimate temporal resolution limit of the optical emission method by comparing the Einstein coefficients corresponding to the generated species with the fast Fourier transformation (FFT) analyzed streak image in chapter 3.6.

3.3 Experimental setup

The experimental setup to observe cathode spots is schematically depicted in Figure 3-5. A linear sputtering magnetron from the Kurt J. Lesker Company was used as a steered arc plasma source. The cathode was an aluminum alloy plate (Al-5754) with a composition of aluminum (97%) and magnesium

(3%) and with the dimensions of 255 mm x 120 mm x 6 mm. The measured magnetic field strength and magnetic field directions of the linear magnetron are shown in Figure 3-6. The magnetic field components were measured using a Tesla meter (model F71 by LakeShore) with three-axis Hall probe sensors less than 500 μm above the cathode surface to confirm the position of a racetrack. The measured magnetic field components were 24,000 points on the cathode surface, and the measuring was done by using an automatic scanning stage. The magnetic field mapping shows that the magnetic field is slightly non-uniform in a central area, as shown in Figure 3-6.

The steered arc plasma source was installed inside a vacuum chamber of 1 m inner diameter, cryogenically pumped to a base pressure of approximately 5.6×10^{-5} Pa. To investigate the arc in low-pressure atmospheres, such as argon (99.999%), nitrogen (99.9999%), and oxygen (99.9992%) were used optionally as process gas. The process gas flow was controlled separately using mass flow controllers (model GV50A by MKS).

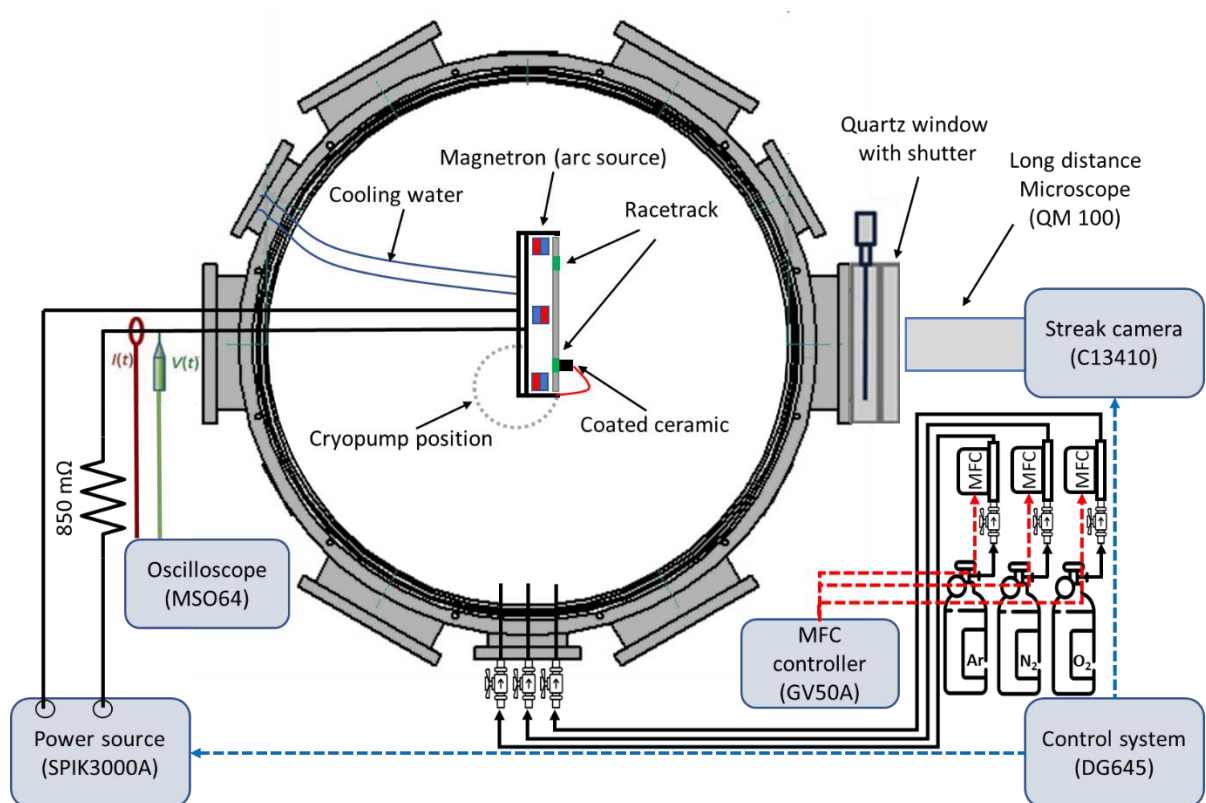


Figure 3-5 A simplified schematic experimental setup. The process gas is introduced into the chamber using mass flow controllers, optionally. (Not to scale)

A “triggerless” or “self-triggering” arc ignition approach was used to ignite the cathodic arc [128], [129]. In this method, a conducted ceramic piece bridged between the anode and cathode, was attached to

the cathode surface to induce “Joule heating” at contact points. The piece was positioned on one of the two linear sections of the racetrack of the cathode surface, as shown in Figure 3-6. A high-power pulsed generator (model SPIK3000A by Melec GmbH) was used to power the cathodic arc discharge, which was charged with a ground-free DC unit (GX50/1000 by ADL GmbH). The applied voltage was between 750 V and 800 V with a pulse width of 100 μ s. The high-power pulse generator has a suppression function of arcing when a threshold current is exceeded. The arc current of the threshold was set up high, and a current limiting resistor (850 m Ω) was installed between the power source and the cathode to deactivate the arc detection function and work with high arc currents.

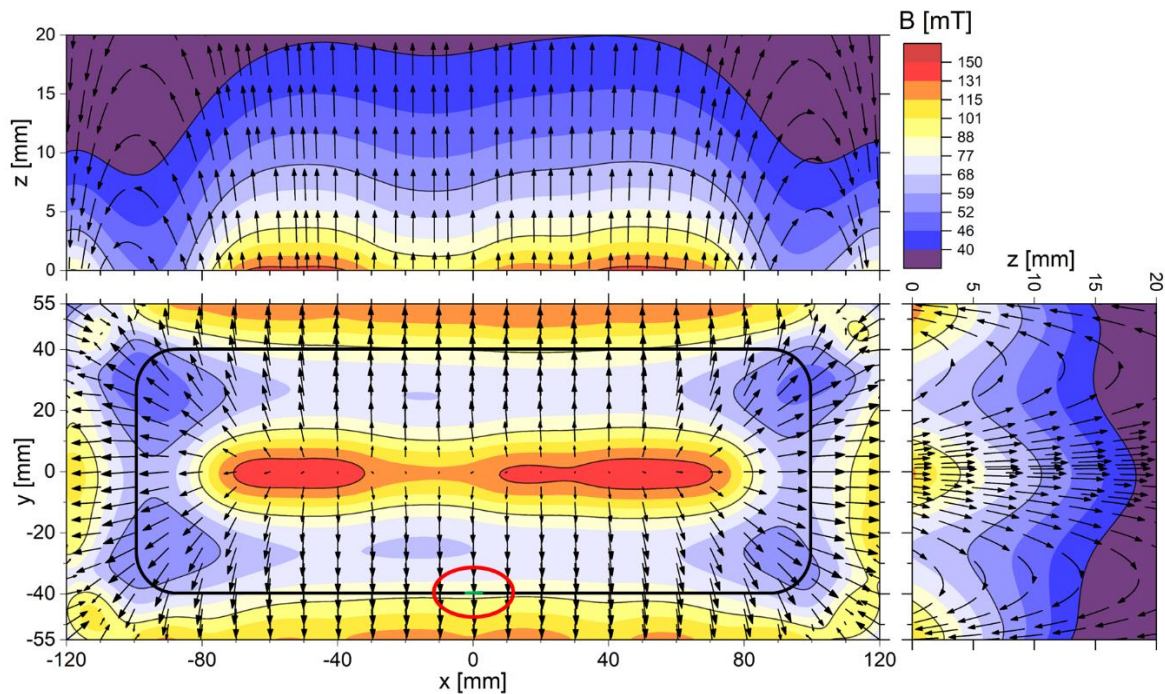


Figure 3-6 The magnetic field strength measured using a three-axis Hall probe less than 500 μ m above the cathode surface. The “racetrack” is marked with a black loop. A narrow green line in the red ellipse indicates the projected area of the entrance slit of the streak camera. (The center of the racetrack is at $B_z = 0$). The front view and side view of the magnetic field were measured at $y = 0$, and $x = 0$, respectively.

The main plasma diagnostic instrument was a streak camera (model C13410 by Hamamatsu) with a long-distance microscope (model QM 100 by Questar). This configuration enables us to investigate the evolution of arc spots with high spatial resolution in one direction (1 μ m/pixel) in different sweep time intervals. As a result, streak images span one dimension of space (the direction of the racetrack) and the other dimension of time. Most spots ignited at the straight section of a racetrack on the cathode surface as decided by the location of the above-mentioned ceramic trigger element. The

specific position of the racetrack next to the trigger ceramic was projected onto the entrance slit of the streak camera (slit width = 20 μm , length = 25 mm). The light passing through the slit is swept for a set amount of time, resulting in the (x, t) -images seen in streak techniques. For better visualization, all raw images from the streak camera were converted from the grayscale intensity values in the image processing software ImageJ [223] using the artificial color scale “royal.”

3.4 Streak imaging results

3.4.1 Arcs in vacuum

Images with sweep time of 10 μs

Selected streak images of cathode spots are shown in Figure 3-7, and zoomed images of the Figure 3-7(a) are shown in Figures 3-7(b) and (c). There is a general trend of spot apparent motion. The spots travel in the $-\mathbf{j} \times \mathbf{B}$ direction, which is called the ‘retrograde direction’ (from left to right in our experimental setup). The streak images show the following attractive characteristics: the spots often occur in separate clusters, where, within each cluster, several spots ignite either at the same or neighboring positions (Figure 3-7(a)). In the investigation of the entire sweep time of 10 μs , the location of spot ignition is changed, on average, in the retrograde direction, whereas this phenomenon is not necessarily observed in the case when looking within a cluster of spots, as shown in Figure 3-7.

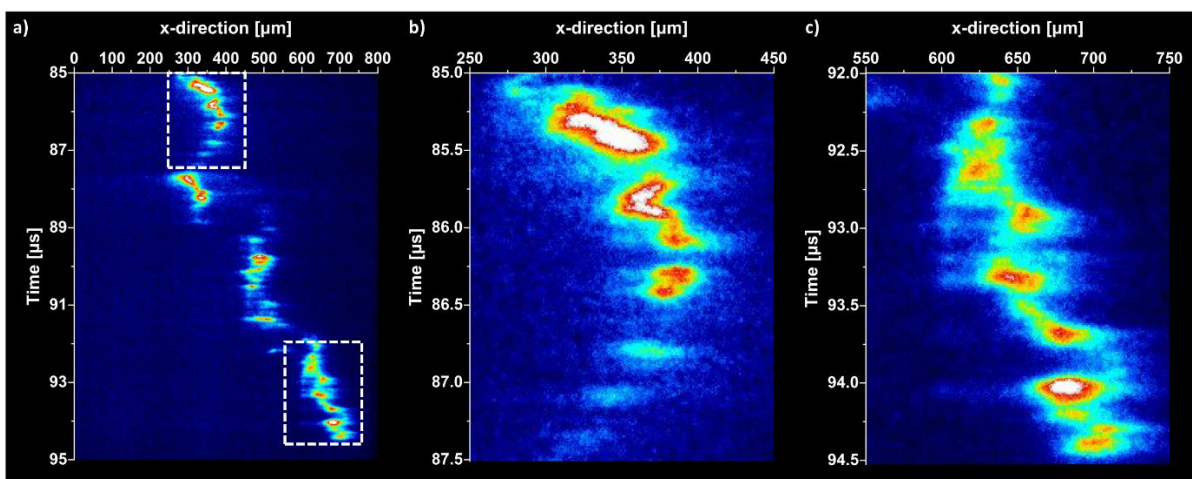


Figure 3-7 (a) Streak images for the cathode spots with 10 μs sweep time; (b) a zoom of the rectangular region in (a); (c) a magnified view of the rectangular area in (a). The applied arc current was 750 A. The color denotes intensity of the plasma light emission (white is the highest intensity of area and

blue is the lowest intensity). The scale of the time-axis is relative to the start of the discharge pulse. The image intensifier set to minimum gain.

In the case of the first cluster, which is magnified in Figure 3-7(b), there is a displacement in a retrograde direction for about $1.5\ \mu\text{s}$ followed by a reversal to the Amperian direction in the next $1.5\ \mu\text{s}$. Taking a closer look at the time interval $85.7\ \mu\text{s}$ to $85.9\ \mu\text{s}$ in the discharge, we see that the light-emitting plasma shifted left (Amperian direction) for about $100\ \text{ns}$ and then shifted right (retrograde direction), in the next $100\ \text{ns}$, for about the same distance. Figure 3-7(c) shows a similar trend again, on average, the displacement is to the right, while individual events may not necessarily show that characteristic.

Images with sweep time of $1\ \mu\text{s}$

Figure 3-8 shows a selected streak image of cathode spots (a) and a zoomed image (b). In Figure 3-8, the lateral displacement of spots is not as clearly observed as previously. This is because the spatial resolution still is the same as before, but the sweep time is changed to $1\ \mu\text{s}$.

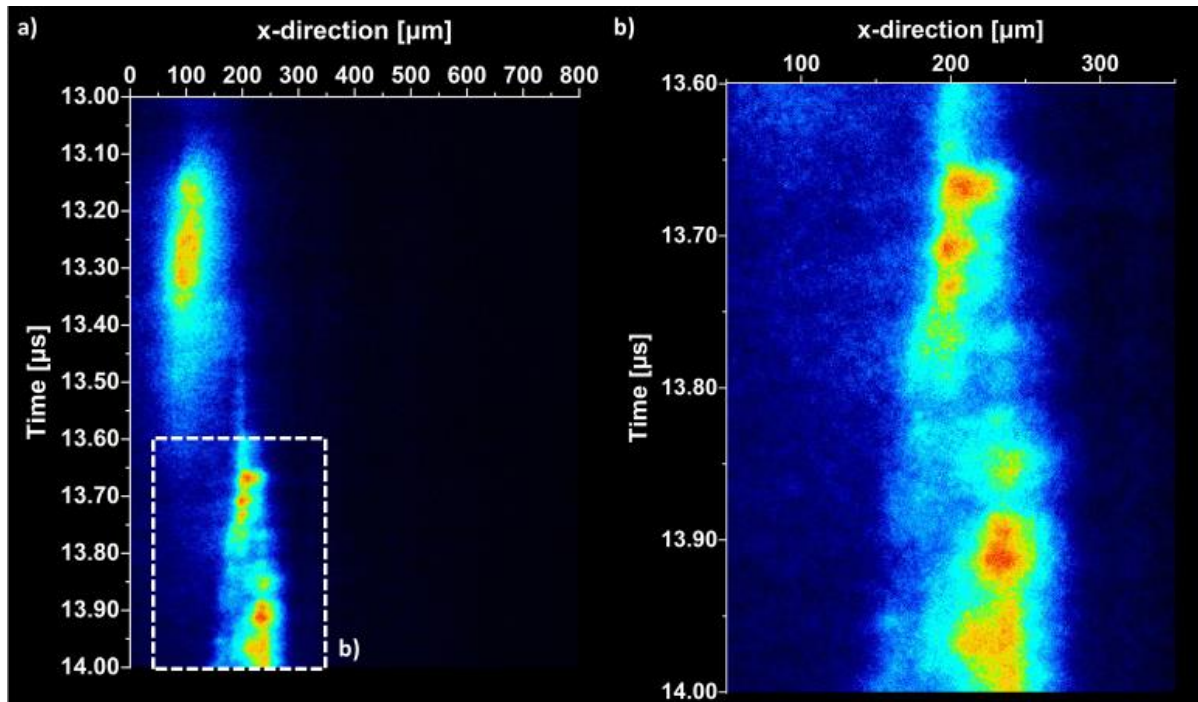


Figure 3-8 (a) Streak images for the cathode spots with $1\ \mu\text{s}$ sweep time; (b) a zoom of the rectangular region in (a). The applied arc current was $800\ \text{A}$. The rest of the details is the same as in Figure 3-7.

The spot displacement is, on average, in the $-\mathbf{j} \times \mathbf{B}$ direction (retrograde direction, as shown in Figure 3-8(a)), and the individual spots within the cluster can be opposite of the retrograde direction, as shown in Figure 3-8(b). The duration of light emission fluctuation associated with spots have various durations but can be as short as 10 ns, as seen with a higher time resolution.

Images with sweep time of 500 ns

Figure 3-9 shows a selected streak image of cathode spots with a sweep time of 500 ns. The general displacement in the $-\mathbf{j} \times \mathbf{B}$ direction is no longer noticeable because the magnification in the spatial direction is not enhanced. Two spot clusters are observed in the selected streak image. The emission light of the left spot is less than the right one.

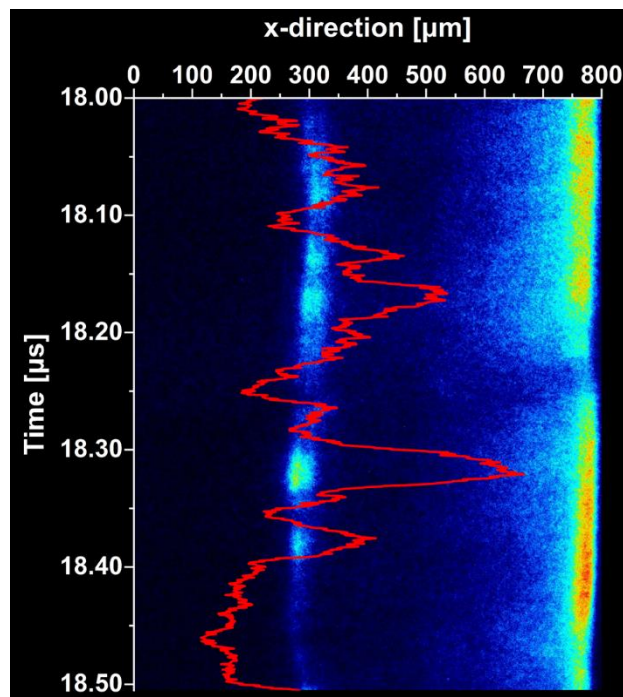


Figure 3-9 Streak images for the cathode spots with 500 ns sweep time; the rest of the details is the same as in the Figure 3-8 The red graph depicts the intensity of light emission fluctuations near the 300 μm location.

The right shows little or no displacement with relatively strong emission, while the left shifts slightly to the left (Amperian direction) with relatively weak emission. This image indicates that more than one spot can be operated in close vicinity to each other. Those simultaneously operating spots can be

of different emission intensity, as shown by the different brightness of the emitting plasma. Their intensity of emission fluctuations does not seem to be correlated with the displacement direction and can be of various brightness. The bright events are accompanied by less intense events before and after.

Images with sweep time of 200 ns

Figure 3-10 shows selected streak images of cathode spots with a sweep time of 200 ns. The lateral displacement is again not found obviously since only the temporal resolution was increased. The trends, already recognized with 500 ns sweep time, as shown in the Figure 3-9, are also observed in 200 ns sweep time. Two spot clusters with different distances can be observed in the selected example images, Figure 3-10(a) and (b). In the case of a relatively close spot, about 100 μm apart, as shown in the Figure 3-10(a), the two spots merge within 20 ns to form a brighter spot at about 24.15 μs into the pulse. When the distance between the two spot is relatively large, about 300 μm , as shown in the Figure 3-10(b), two spots operate independently, occasionally re-igniting at about their same respective positions.

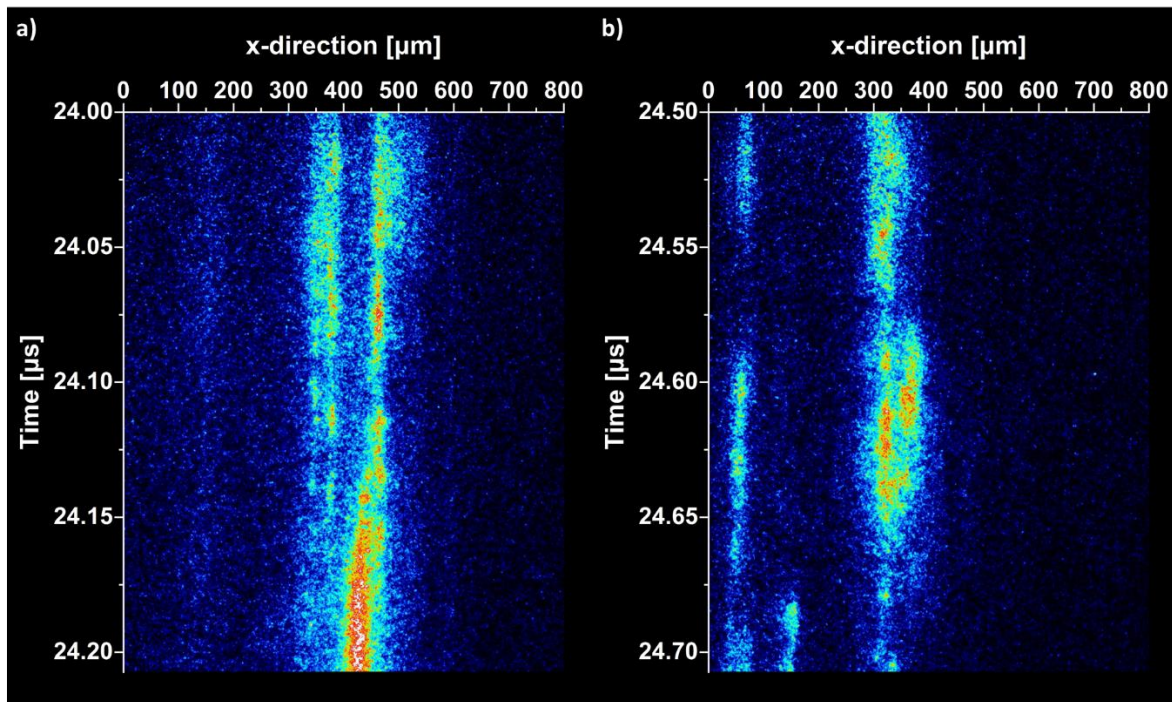


Figure 3-10 Streak images for the cathode spots with 200 ns sweep time. The intensifier gain of streak images was set to '15', while all other parameters remained the same as for the previous images.

As the sweep time was selected to 200 ns, finer characteristics in terms of temporal fluctuations can be observed. For example, short bursts of the brightness of 5 ns or even less can be shown in Figure 3-10. It is shown clearly that the distinguishable duration of brightness fluctuations depends on the sweep time setting of the optical measuring system through our experiment. This characteristic is a specific property of a self-similar (fractal) system.

3.4.2 Arcs in low pressure argon, nitrogen, and oxygen atmospheres

Images with sweep time of 10 μ s for spots in argon

Figure 3-11 shows selected streak images of cathode spots at different argon pressures: (a) 44 mPa and (b) 760 mPa. The spots have a similar trend even at different process gas pressure. Namely, they generally travel in the $-\mathbf{j} \times \mathbf{B}$ direction, which is the “retrograde motion”. The appearance of spot motion is generally in the retrograde direction, but some spots occasionally have Amperian direction, as shown in Figures 3-11(a) and (b), marked by a white rectangle. For instance, in the rectangle in Figure 3-11(a) from 10.7 μ s, the appearance of spots motion is in the retrograde direction for about 200 ns and then the direction has a reverse direction for about the next 200 ns. In Figure 3-11(b), the averaged displacement is observed again; here, the spot traveling for about 500 ns to the left (Amperian direction) and then, in the next 500 ns, to the right, and lastly, the spot travels again in the Amperian direction. This trend also was found in the case of the vacuum arc spot motion.

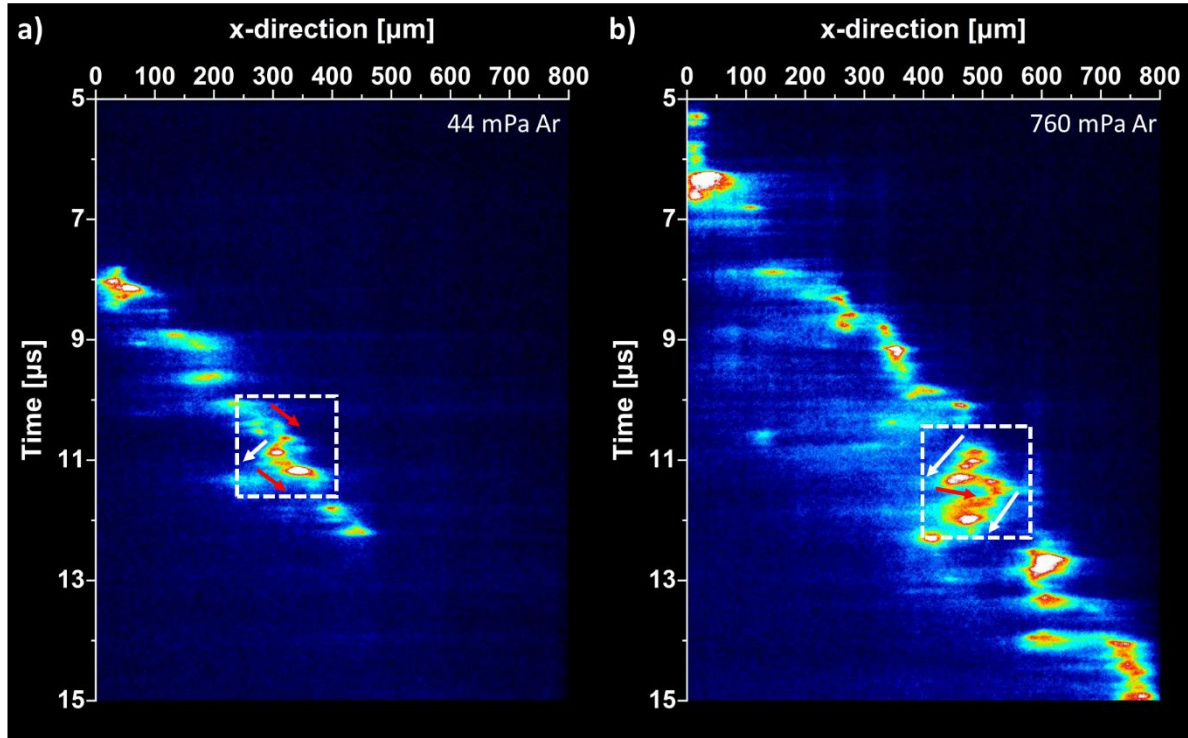


Figure 3-11 Streak images of the cathode spots in argon at a pressure of (a) 44 mPa and (b) 760 mPa with 10 μs sweep time. The applied arc current was 750 A. The retrograde direction is indicated by the red arrow, while the Amperian direction is indicated by the white arrow in the white rectangular area. The apparent motion is generally from left to right (retrograde direction), but it can also be in the opposite, the Amperian direction.

Images with sweep time of 1 μs for spots in argon

Figure 3-12 shows selected streak images of cathode spots with a sweep time of (a) 1 μs and (b) a zoomed image of the rectangular area in (a). The retrograde motion is not observed as clearly as in the case of 10 μs sweep time image since this image has a shorter sweep time, but the spatial resolution was not enhanced.

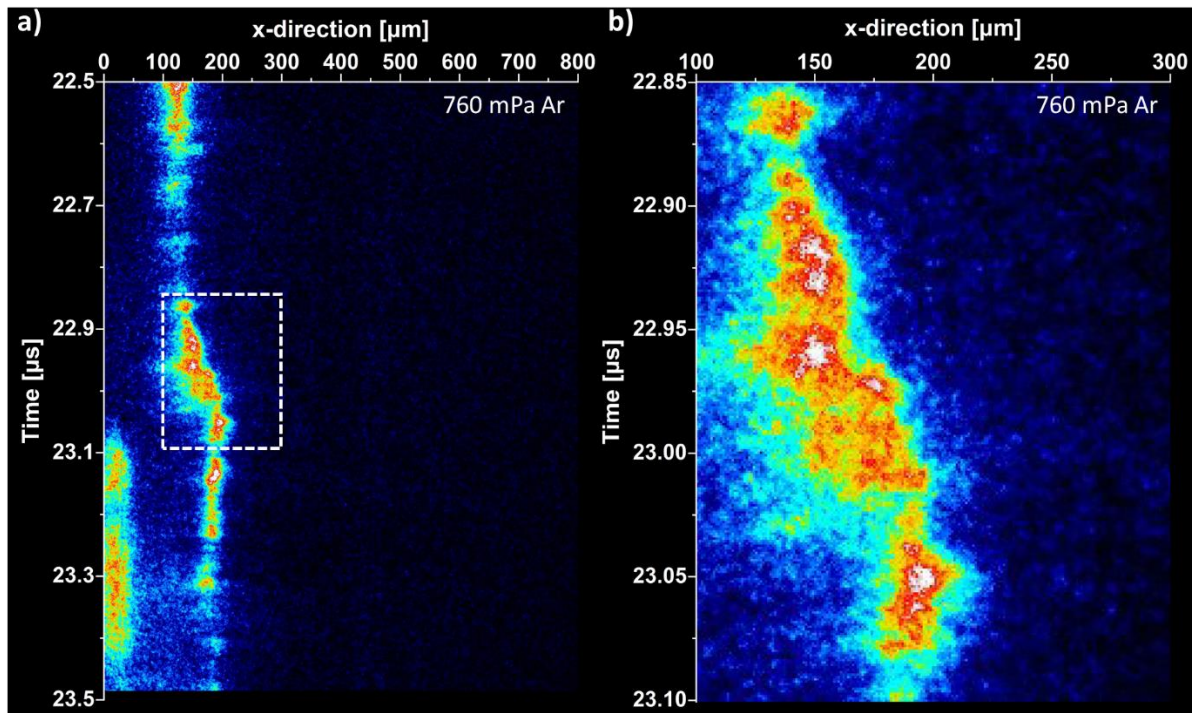


Figure 3-12 (a) Streak images for the cathode spots with 1 μs sweep time in 760 mPa argon; (b) a zoomed image of the white rectangular area in (a). The applied arc current was 750 A. The intensifier gain of streak images was set to '15'. All other parameters remained the same as for the previous images.

The moment of transition in the retrograde direction is observed, as shown in Figure 3-12. The spot location has a multi-step away from 150 μm to 175 μm and to 200 μm in a more gradual (from left to right at about 22.95 μs and 23.05 μs , respectively). The plasma emission does not show a clear periodic trend.

Images with sweep time of 10 μs for spots in nitrogen

Figure 3-13 shows selected streak images of cathode spots at various nitrogen pressures: (a) 17 mPa, (b) 30 mPa, (c) 125 mPa, (d) 1 Pa. The apparent motion of spots goes in both directions, retrograde ($-\mathbf{j} \times \mathbf{B}$) and Amperian ($\mathbf{j} \times \mathbf{B}$), especially obvious at relatively low nitrogen pressure as shown in Figures 3-13(a) – (c).

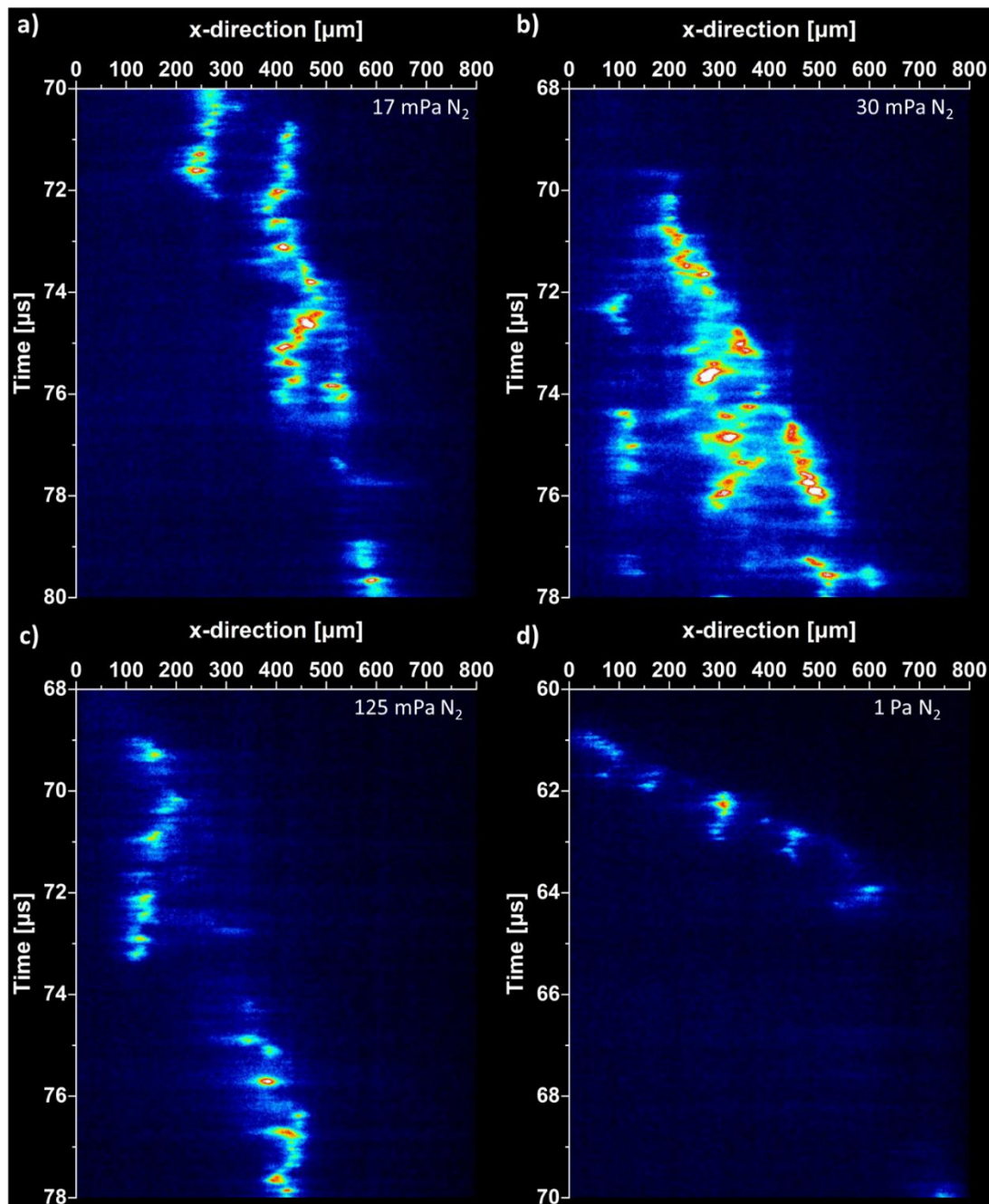


Figure 3-13 Streak images of the cathode spots in nitrogen at a pressure of (a) 17 mPa, (b) 30 mPa, (c) 125 mPa, and (d) 1 Pa with 10 μ s sweep time. The applied arc current was 750 A.

The majority of the retrograde motion images shows clusters of spots. Some spots occasionally have longer jumps with a distance of about 200 μ m, which looks related to the formation of new spots and clusters of spots. Often, sequential ignitions of spots seem to be connected, forming chains of spots, as shown in Figure 3-13. As the process gas pressure increases, the lengths of such chains become shorter on average. As shown in Figure 3-13(d), the apparent spot motion is in the primarily retrograde direction at relatively high gas pressure.

Images with sweep time of 1 μ s for spots in nitrogen

Figure 3-14 shows selected streak images for the cathode spots in nitrogen at pressures of (a) 6 mPa and (b) 1 Pa. The general spot motion trend in the presence of a magnetic field is not apparent in Figure 3-14 since only the time resolution was enhanced, but the spatial magnification remained unchanged.

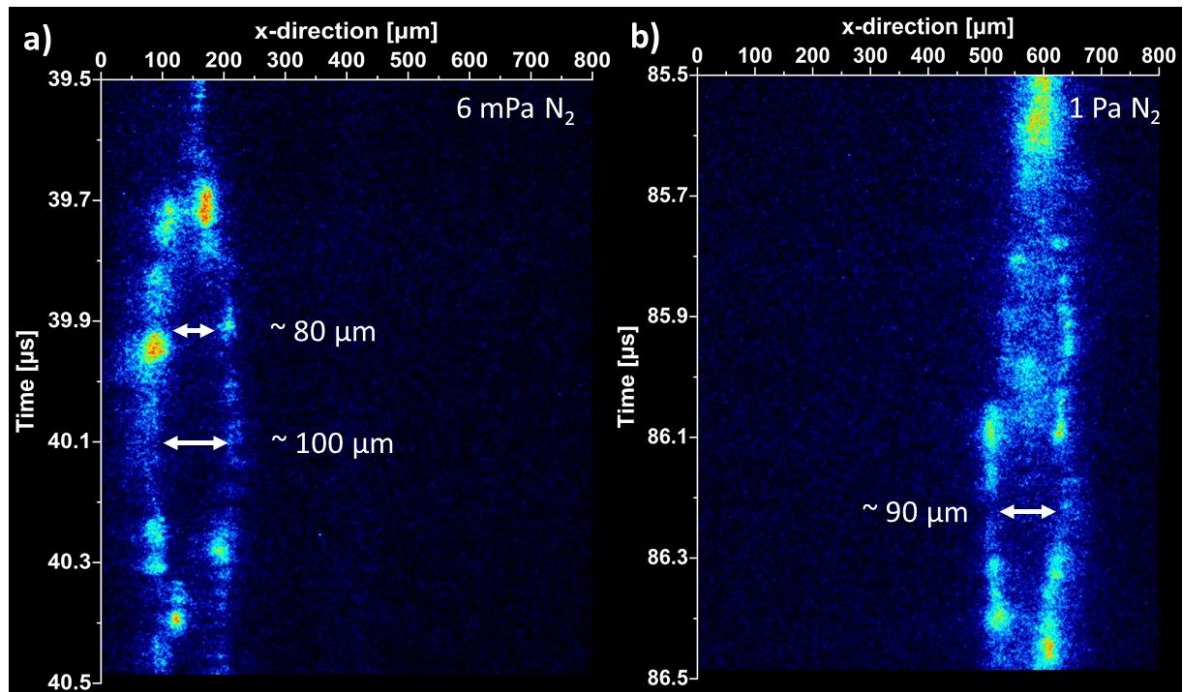


Figure 3-14 Streak images of the cathode spots in nitrogen at pressures of (a) 6 mPa and (b) 1 Pa with 1 μ s sweep time. The applied arc current was 750 A.

In Figure 3-14, one interesting feature was found: the emission site splits and follows two paths. In the example, the measured distance between sites of plasma emission was roughly 80 μ m and 100 μ m at about 40.0 μ s and 40.1 μ s, respectively. As shown in Figure 3-14(a), the measured distance increases in the range between about 39.8 μ s and about 40.1 μ s. Figure 3-14(b) shows a selected streak image of cathode spots in a nitrogen atmosphere of 1 Pa. In the streak images, several spots are visible along the paths between about 86.1 μ s and about 86.5 μ s in the streak images. The measured distance between sites of spot emissions was approximately 90 μ m at about 86.2 μ s.

Images with sweep time of 10 μ s for spots in oxygen

Figure 3-15 shows selected streak images of cathode spots ignition at various oxygen pressures: (a) 17 mPa, (b) 125 mPa, (c) 760 mPa, (d) 1 Pa. The trends of apparent spot motion in an oxygen atmosphere are quite different from spots in pure vacuum, argon, and nitrogen.

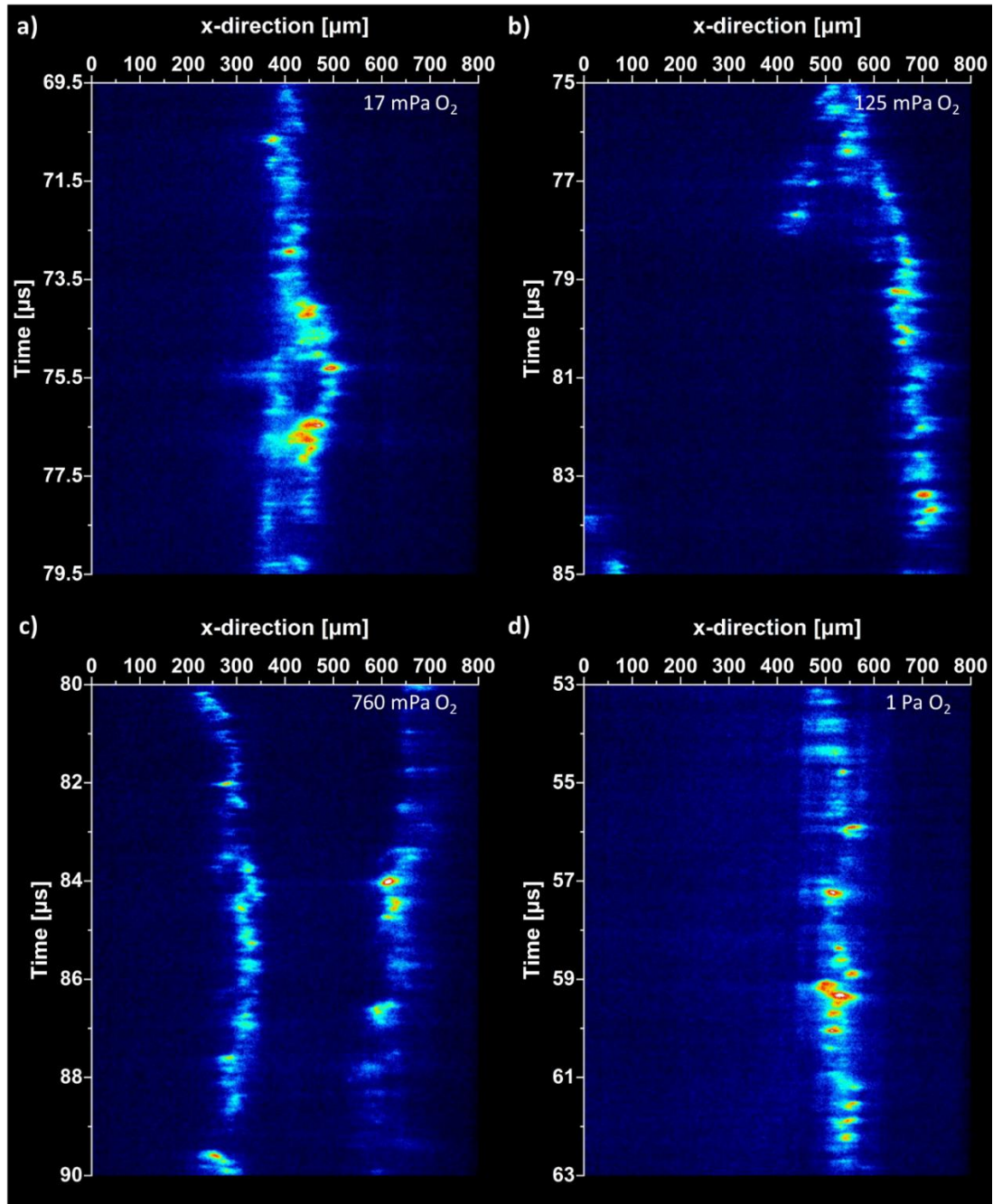


Figure 3-15 Streak images of the cathode spots in oxygen at a pressure of (a) 17 mPa, (b) 125 mPa, (c) 760 mPa, and (d) 1 Pa with 1 μ s sweep time. The applied arc current was 750 A, and the image intensifier gain was set to minimum value.

In general, the cathode spots travels in the retrograde ($-\mathbf{j} \times \mathbf{B}$) direction in the presence of a transverse magnetic field. However, as seen in Figure 3-15, it seems that the apparent motion of spots does not have a dominant direction in the oxygen atmosphere. The apparent motion of spots shows a trend that repeatedly ignites in almost the same position. The ignition and extinction events look like a spot chain along the time direction of a streak image. On average, the length of such a chain is longer than those found in nitrogen. Also, multiple cathode spot ‘chains’ can be present at the same time, as shown in Figure 3-15(c). The spot chains in oxygen are not significantly reduced when the gas pressure is increased, as it is in nitrogen. The above statements are based on trends discovered by analyzing a large number of streak images. Streak images are particularly adapted to revealing spot features in oxygen.

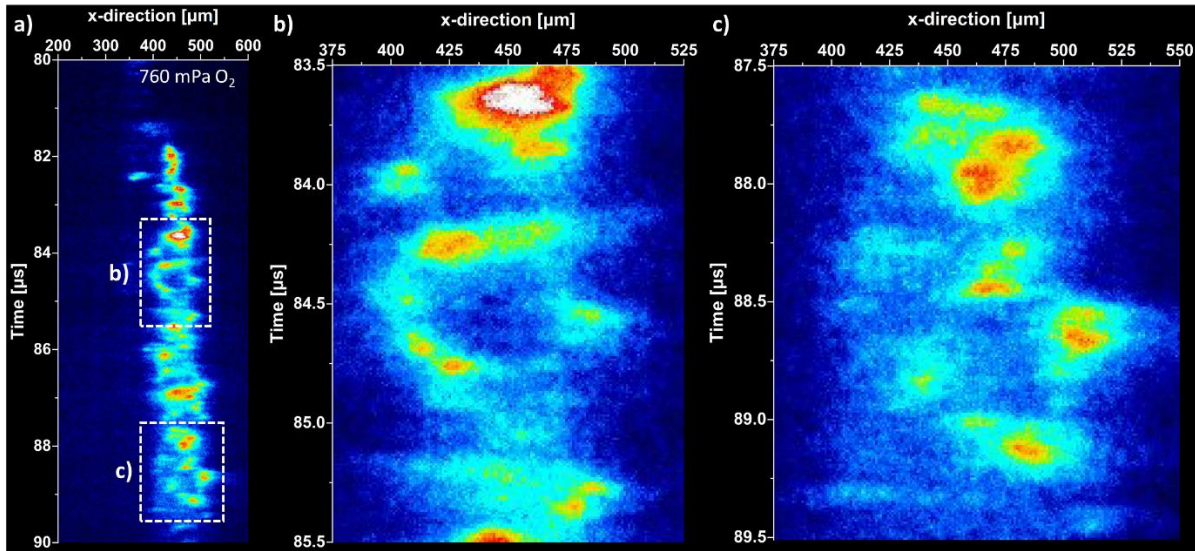


Figure 3-16 (a) Streak images of the cathode spots in oxygen at a pressure of 760 mPa with 10 μs sweep time; (b) a zoomed image of the white rectangular area indicated (b) in (a); (c) a zoomed image of the white rectangular area indicated (c) in (a). The applied arc current was 750 A. The image intensifier was set to the lowest gain value.

Figure 3-16 shows a selected streak image for the cathode spots in oxygen at a pressure of 760 mPa. In the example, new cathode spot ignitions occur next to the previous site and then again close to the initial site. As seen in Figure. 3-16(a), the spot is slightly steered in the retrograde direction.

Images with sweep time of 1 μ s for spots in oxygen

Figure 3-17 shows a selected streak image of cathode spots with 1 μ s sweep time in 17 mPa of oxygen. It shows a similar observation trend with spots in nitrogen, as shown in Figure 3-14. For example, in this streak image, the measured distance between of plasma emission site at about 79.05 μ s is about 30 μ m, and the measured distance between of plasma emission site at about 79.3 μ s is about 50 μ m. Also, the measured distance between sites of plasma emission at around 79.05 μ s is equivalent to the distance of the emission site at 78.9 μ s, as shown in Figure 3-17.

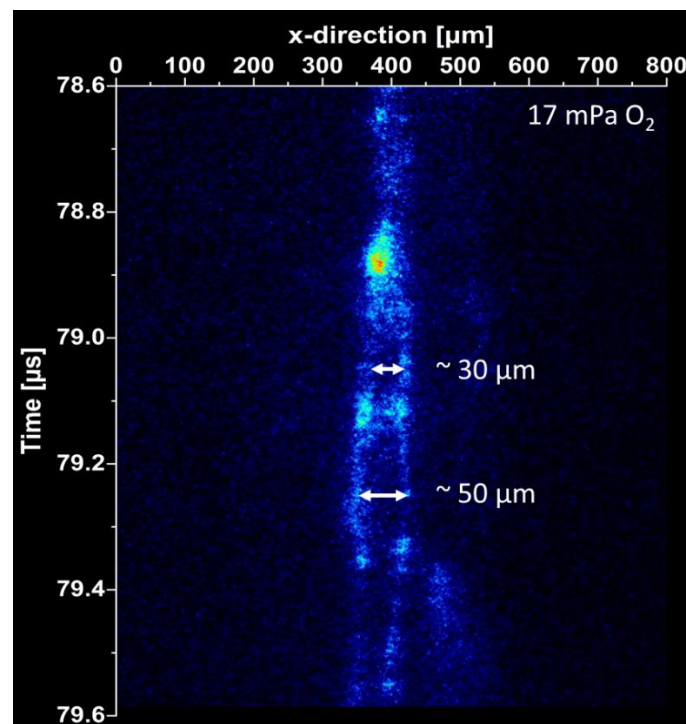


Figure 3-17 Streak images of the cathode spots in oxygen at a pressure of 17 mPa with 1 μ s sweep time. The applied arc current was 750 A. The image intensifier gain was set to '10'.

3.5 Fast Fourier transform (FFT) analysis of experimental results

Whether the cathode spots have characteristic lifetimes such as a 'periodic spot lifetime' or show a broad spectrum of emission fluctuations can be investigated by analyzing the streak camera images. The fractal description is a proper approach to investigate cathode spot ignition because the cathode spot has self-similarity, which is well known as one of the fractal characteristics. Such analysis (self-

similar analysis) is most effectively conducted by fast Fourier transformation (FFT). The brightness fluctuation data can be obtained from the streak camera images. The data can be transformed into the spectral power density as a function of frequency using FFT. If there exist specific peaks in the spectral power density as a function of frequency, it means the cathode spots have such characteristic times. In the case of opposite, such function can be described by a power law, and it would be supportive for the fractal model [39]. The power law can be described by mathematical fitting with its own steepness, which is named the “Colored Random Noise (CRN)” index, as mentioned in chapter 2.1.6. The CRN index presents a quantitative measure for fluctuations and has a physical meaning, depending on the value ($\alpha = 0$; white noise, $\alpha = 1$; pink noise, $\alpha = 2$; brown noise, $\alpha > 2$; black noise). Here, the results of the fractal description are going to be shown separately for the arcs in vacuum and arcs in various gas with different process pressure.

3.5.1 FFT analysis of arcs in vacuum

Figure 3-18 shows a selected streak image (a) of the cathode spots with 500 ns sweep time and the spectral power density graph (b) generated by the FFT of fluctuation data from Figure 3-18(a). The spectral power density that can be fitted to a power law shows the absence of peaks, as shown in Figure 3-18(b). The calculated CRN index is close to brown noise ($\alpha = 2$) at intermediate frequencies (2×10^6 Hz– 3×10^8 Hz). The physical meaning of the brown noise is related to the Brownian motion, which are the steps in a diffusion process. This observation is a similar result to the random walk of cathode spots, characterized for Brownian motion ($\alpha = 2$) by analyzing arc traces [32], and voltage noise fluctuation, featured for brown noise ($\alpha = 2$) by measuring pulsed arc voltages [180]. The specific characteristic frequency or related time cannot be identified; rather, the streak data can support the fractal model which shows a CRN index near 2 (2.2 ± 0.1). Therefore, the spot ignition and extinction events can be associated with a stochastic description, even in the case of a magnetically steered vacuum arc. According to the fractal theory, considering the CRN index, a number greater than 2 indicated stronger feedback of previous step events compared to Brownian motion.

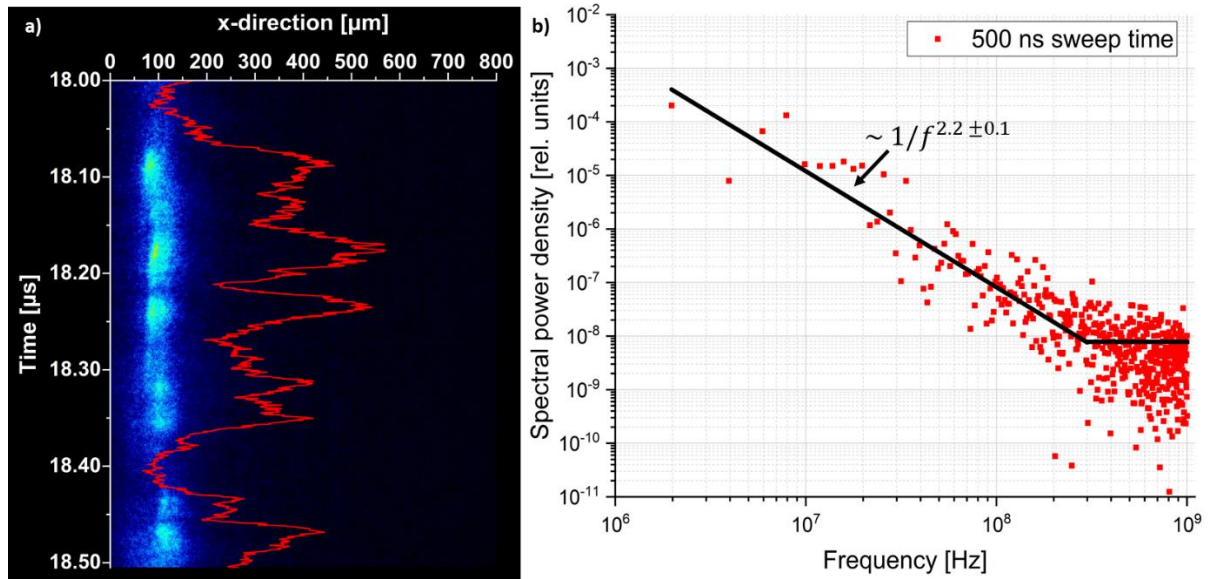


Figure 3-18 Example of a vacuum arc spot streak image with 500 ns sweep time. The arc current was 800 A. The red graph in (a) depicts the intensity of light emission fluctuations near the 100 μm location; (b) Spectral power density (intensity²/frequency in rel. units) determined by the FFT of the light emission fluctuation data from (a); the black line in (b) reflects the intensity of light emission fluctuations near 100 μm location and shows a fit for an CRN index near 2 below 300 MHz and white noise for higher frequencies.

3.5.2 FFT analysis of arcs in low pressure argon, nitrogen, and oxygen atmospheres

Figure 3-19 shows a selected streak image (a) of cathode spots with 1 μs sweep time in 125 mPa of oxygen and the spectral power density graph (b) generated by the FFT of fluctuation data from Figure 3-19(a).

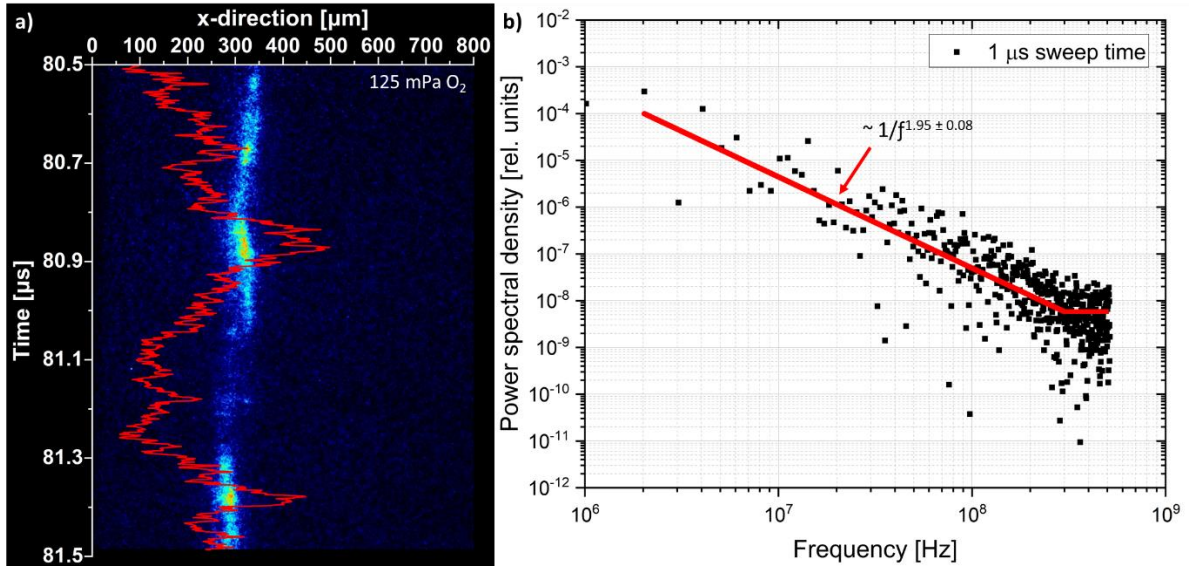


Figure 3-19 (a) Example of a cathode spot streak image with 1 μ s sweep time in 125 mPa of oxygen. The arc current was 750 A. The red graph in (a) depicts the intensity of light emission fluctuations near the 300 μ m location; (b) Spectral power density (intensity²/frequency in rel. units) determined by the FFT of the light emission fluctuation data from (a); the red line in (b) shows a fit for an CRN index near 2 below 300 MHz and the line reflects the intensity of the light emission fluctuations near the 300 μ m location.

The result of the spectral power density analysis shows that the absence of peak is confirmed even in the case of low-pressure oxygen atmosphere. The CRN index value is lower than the case of vacuum arc at intermediate frequencies (2×10^6 Hz – 3×10^8 Hz), but the value is still close to 2, as shown in Figure 3-19(b).

The CRN index for argon, nitrogen and oxygen at different process pressures are presented in Figure 3-20. In the case of argon, the CRN index in the observed pressure range is kept the almost same value 2.2, indicating that spots appear according to the Brownian motion and that the cathode surface conditions are unaffected by the gas, i.e., practically no compound layer is present, similar to the case of pure vacuum arc.

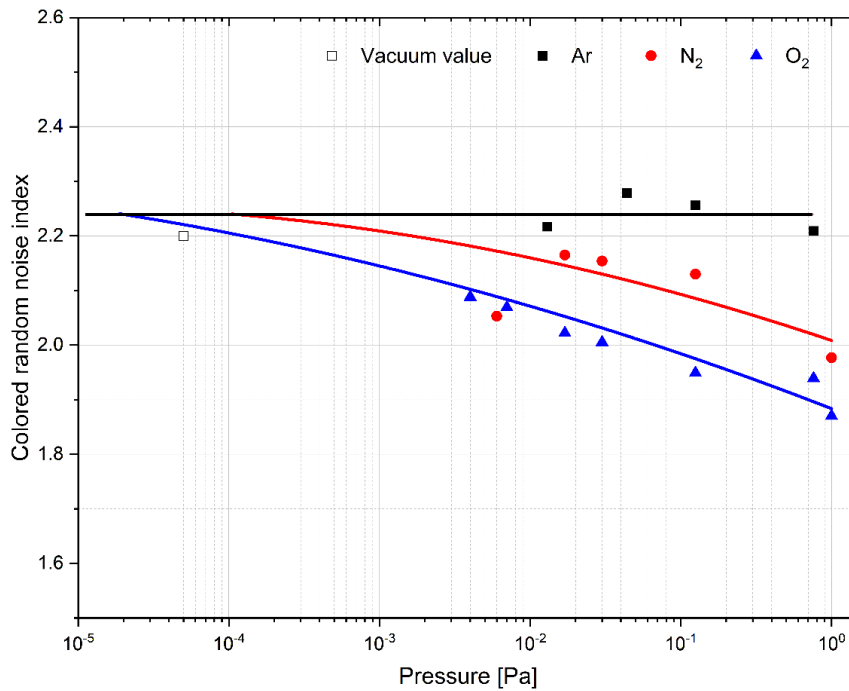


Figure 3-20 The obtained colored random noise (CRN) index of argon (black square), nitrogen (red circle), and oxygen (blue triangle) with various process pressures. Each data point represents an average of 10 measured data. The open shape square indicates a measured data for vacuum arcs. The lines are inter- and extrapolated fits.

For the case of nitrogen and oxygen, the CRN indexes have a decreasing trend when the pressure is increased from 17 mPa to 1000 mPa and from 4 mPa to 1000 mPa, respectively. A smaller CRN index indicates the low-frequency events decline compared to high-frequency events, which means that the decreased CRN index values correlate with reduced feedback or relevance of previous spot events. In the presence of a reactive gas, the CRN index is lower than in the argon and pure vacuum case. This indicates that the spot ignition event occurs relatively quickly in the reactive gas medium, i.e., the spot ignites quite easily when the compound is readily formed on the cathode surface. The compound layer is the result of competing processes of layer formation and erosion by the cathode spot ignition on the cathode surface. In the case of oxygen and nitrogen, extrapolation of the CRN curves eventually reaches the curve for argon-vacuum to lower pressures, as shown in Figure 3-20. There is an overlap point between the argon-vacuum curve with nitrogen and oxygen curves. The intersection indicates that respective reactive gas is becoming applicable. Clearly visible, the intersection is positioned at lower pressure for oxygen than for nitrogen. According to previous literature [34], the thermodynamic driving force (Gibbs free energy) indicates how easy the compound layer is formed on the cathode surface. Noble gases do not form a compound on the cathode surface, and therefore spots in argon show similar behavior as spots in vacuum.

3.6 Fundamental limitations of optical emission method

The cathode spot motion was investigated by various optical methods such as optical emission spectroscopy [217], including line shape analysis [224], optical absorption imaging [28], [29], interference and shadow techniques [30], [225], fast framing camera imaging [12], [118], [226], [227] and streak camera imaging [15], [26], [51], [228]. Due to the spot ignition occurring at various locations, it is impossible to utilize methods other than optical techniques, such as probes.

The temporal resolution limit of any optical emission method is associated with the finite lifetime of excited atomic and ion states. Namely, the collected light comes from the optical transition from upper levels of atoms and ions, each having a finite lifetime described by their respective Einstein coefficients [53]. Therefore, the optical emission method has fundamental limitations for observing spot ignition. To confirm this interpretation, the primary optical transitions which contributed to the streak images of vacuum arc is required. The emission spectrum lines of vacuum arcs were measured with a PI-MAX 4 camera (Princeton Instruments) coupled to an IsoPlane SCT320 spectrometer under the same experimental discharge conditions. The obtained emission spectrum is shown in Figure 3-21.

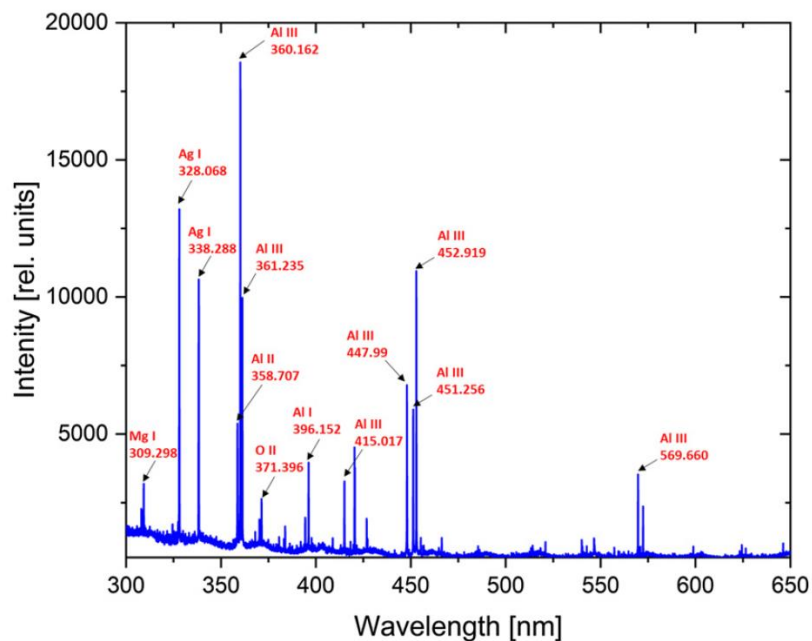


Figure 3-21 Emission spectrum of vacuum arc between 300 nm and 650 nm; the intensities obtained are corrected for the spectral sensitivities of the PI-MAX versus streak camera detector.

The dominated emission spectrum lines are aluminum and silver ions due to the silver glue used to attach the trigger ceramic to the aluminum cathode. From the measured spectrum, the five most intense lines and their Einstein coefficients are presented in Table 3-2.

Table 3-2 Emitting species, wavelength of the most intense lines contributing to imaging of vacuum arc, and their Einstein coefficients [229], [230].

	Wavelength [nm]	Einstein coefficient [10^8 s^{-1}]
Ag I	328.068	1.40
Ag I	338.288	1.30
Al III	360.162	1.31
Al III	361.235	1.45
Al III	452.919	2.49

The Einstein coefficients are related to the lifetime of the upper level of the optical transition; thus, if the sequence of explosive spot ignitions is faster than the most probable lifetimes of the excited state, the spot events cannot be clearly distinguished. The events would be blurred in time collecting light by any optical detector. This phenomenon can be supported by slop transition to white noise. In the case of vacuum arc, the transition to white noise is found higher than about 280 MHz in Figure 3-18(b). This value is correlated with the limits observed for the vacuum arc since the Einstein coefficients are associated with the lifetime of the upper level of the optical transition. In our case, the aluminum ions found mainly have three different wavelengths of 360.162 nm, 361.235 nm, and 452.919 nm, and the Einstein coefficients corresponding to each wavelength are $1.31 \times 10^8 \text{ s}^{-1}$, $1.45 \times 10^8 \text{ s}^{-1}$, and $2.49 \times 10^8 \text{ s}^{-1}$, respectively. The optical emission from the excited state occurs according to the frequency, and the maximum frequency observed is about 250 MHz which is consistent with the values less than 300 MHz that are transited white noise found in the fractal analysis, as shown in Figure 3-18(b).

3.7 Discussion and conclusions

The cathode spot investigations were done in vacuum ($5.6 \times 10^{-5} \text{ Pa}$) and low-pressure argon, nitrogen, and oxygen atmospheres using a state-of-art plasma diagnostic device, a streak camera with a long-distance microscope. The combination of streak camera and long-distance microscope allows us to observe the cathode spots with very high spatial and temporal resolution.

The apparent motion of the cathode spot appears in the retrograde direction, on average, in a form of cluster, in the presence of a transverse magnetic field. However, the apparent motion of the cathode spot has a different trend inside a cluster. The displacements of spots can occasionally be in the Amperian direction for the case of vacuum and a noble gas, argon, inside a cluster.

For the reactive gases, nitrogen, and oxygen, it is found that the characteristics of cathode spot ignition have a different trend. Both gases show that spots ignition looks like a connected “chain” along the time direction. The length of such a chain is reduced as the process pressure is increased for the case of nitrogen. However, in the case of oxygen, the length of the chain is not strongly affected when reducing process pressure. The apparent motion of the cathode spot also shows a different trend compared to the vacuum and argon cases. In the case of nitrogen, the apparent motion of spots usually is in the retrograde direction at high nitrogen pressure, but at low pressure, displacements in both directions are confirmed. For oxygen, the spots do not travel much. The spots repeatedly ignite in the vicinity of previous spot sites, thus there is no obvious preferential direction.

In terms of spot type, spot type 1 is found more often in the reactive gas atmosphere, especially, in oxygen, compared to spot type 2, since spot type 1 ignites on a compound layer of the cathode spot. In the case of spot type 2, it generally ignites on the cathode surface, which lacks a compound layer; thus, the spot type 2 is identified in the argon and the vacuum cases. The spot type can switch from one to another depending on the state of the cathode surface and reactive gas pressure.

A detailed analysis of the fluctuations of the emission of spots is conducted by using fast Fourier transformation (FFT), leading us to a spectral power density. According to FFT analysis, a broad spectrum, described in a fractal (self-similar) model framework, is observed instead of specific characteristic frequency. It means that the spot ignition occurs stochastically without periodicity. The similar trend observed with different sweep times is also the characteristics of self-similarity confirmed through streak images.

A slope in FFT, the colored random noise (CRN) index, is analyzed to quantify the fluctuations of emission spots. The CRN index shows that the fluctuations of emission spots may be affected by previous stochastic events. The CRN index shows the fluctuation of spots is related to the Brownian motion of spots in vacuum and argon (index close to 2), and the CRN index value is not changed when using different argon pressures. The CRN indices of nitrogen and oxygen are lower than the case of argon and vacuum. This result could be correlated to the spot ignition processes. The spot ignition processes occur relatively easily since the compound layer is formed on the cathode surface. The CRN index value is reduced when process pressure is increased.

4. Investigation of the effect of ion potential energy on film growth

4.1 Three different cases for investigation of the effect of ion potential energy on film growth

To investigate the effect of ion potential energy, we deposited aluminum films with a cathodic arc deposition process under three different configurations. The aluminum film was deposited in a silicon substrate with 60 nm thickness. In all three cases, in order to maintain the same film deposition thickness, the film deposition pulses were applied to 9,000 pulses for the reference case, 6,000 pulses for the plasma biasing case, and 1,500 pulses for the high charge state case. The three different configurations were defined as follows:

- Reference case (Reference values of ion kinetic and potential energy in this experiment)
The plasma generation is from a cathodic arc source of minigun type without an external magnetic field and plasma biasing.
- High charge state case (Relative high ion potential and kinetic energy to the reference case)
The plasma generation is from a cathodic arc source of minigun type with the external magnetic field to increase ion charge state, caused high ion potential and kinetic energies [134], [231].
- Plasma biasing case (Comparable ion potential energy to the reference case and comparable kinetic energy to the high charge state case)
The plasma generation is from a cathodic arc source of minigun type without the external magnetic field and the generated plasma is accelerated with comparable kinetic energy with the high charge state case by using plasma biasing [232], [233]. The ion kinetic energy is determined empirically to be comparable with the high charge state case by tuning plasma potential.

The plasma for those three conditions is characterized for energy/mass distribution with energy-resolved mass spectrometer (ERMS) [145], [232], [233], and the characteristic of deposited films under three different configurations is performed by using X-ray diffraction (XRD), X-ray reflectometry (XRR),

atomic force microscopy (AFM), profilometry and scanning electron microscope (SEM) analysis to investigate the effect of the ion potential energy. Combining plasma diagnostic and the film characterizations makes it possible to understand preliminarily how ion potential energy affects film properties.

4.2 Tuning of ion kinetic and potential energies

The importance of the effect of ion potential and kinetic energy on film growth was described in chapter 2.2.2. This chapter considers the practical way of tuning ion kinetic and potential energy. The total energy of ions arriving on the substrate surface consists of the ion kinetic energy and ion potential energy, and the total energy can be described as following [42]

$$E(Q) = E_0 + QeV_{sheath} + E_{ic} + E_c + E_{exc} + \sum_{Q'=0}^{Q-1} E_{Q'} \quad (4.1)$$

From equation (4.1), the first three terms are related to the ion kinetic energy, and the last three terms are related to the ion potential energy. To observe only the effect of ion potential energy, the kinetic energy should be maintained at similar energy values in conditions with different ion potential energy values. However, it is not easy to keep the same kinetic energy in the whole experimental procedure in practice because the kinetic and potential energy are coupled through the conditions of plasma formation. For considering the effect of ion potential energy on film deposition, the experiment has been performed under three different configurations: the reference case (free plasma expansion without an external magnetic field [82]), the high charge state case (plasma expansion with an external magnetic field near the anode [134], [145], [137]), and plasma biasing case (plasma expansion with plasma biasing [232], [233]). The second case (the high charge state case) has the highest potential energy value because produced ions have a higher charge state compared to the reference and plasma biasing case. It is well known that the external magnetic field increases the plasma impedance, which causes a high burning voltage [1], [137]. The higher charge state increases ion kinetic energy and potential energy, as shown in the defined equation (4.1). The third case (the plasma biasing case) is applied for plasma biasing. In this case, the plasma biasing is achieved when the anode potential is shifted positively with respect to the ground [233]. Using substrate biasing can cause the same effect, which means tuning the plasma biasing can control V_{sheath} in the equation (4.1). Since the plasma biasing has the same effect [232] on the ion energy that can be obtained when the substrate is grounded and the plasma is positively biased, the kinetic energy distribution of ions is tuned by the

controlling of the plasma biasing voltage, without affecting the ions' potential energy [233]. By using the plasma biasing approach, it is possible to deposit thin films with differently energetic film forming species on the grounded substrates. Since the energy-resolved mass spectrometer is also grounded, one can deposit thin films with the known plasma properties. Plasma biasing is a promising approach to practically embody the role of ion potential energy in experiments [232], [233].

4.3 Experimental setup

The experimental setup is shown in Figure 4-1. The filtered pulsed cathodic arc was used for experiments. The experimental setup consisted of a cathodic arc “minigun” plasma source with an electro-magnetic coil (EM-coil) and macroparticle filter (MPF). It was installed inside a vacuum chamber with 1 m inner diameter, cryogenically pumped to a base pressure of approximately 5×10^{-5} Pa.

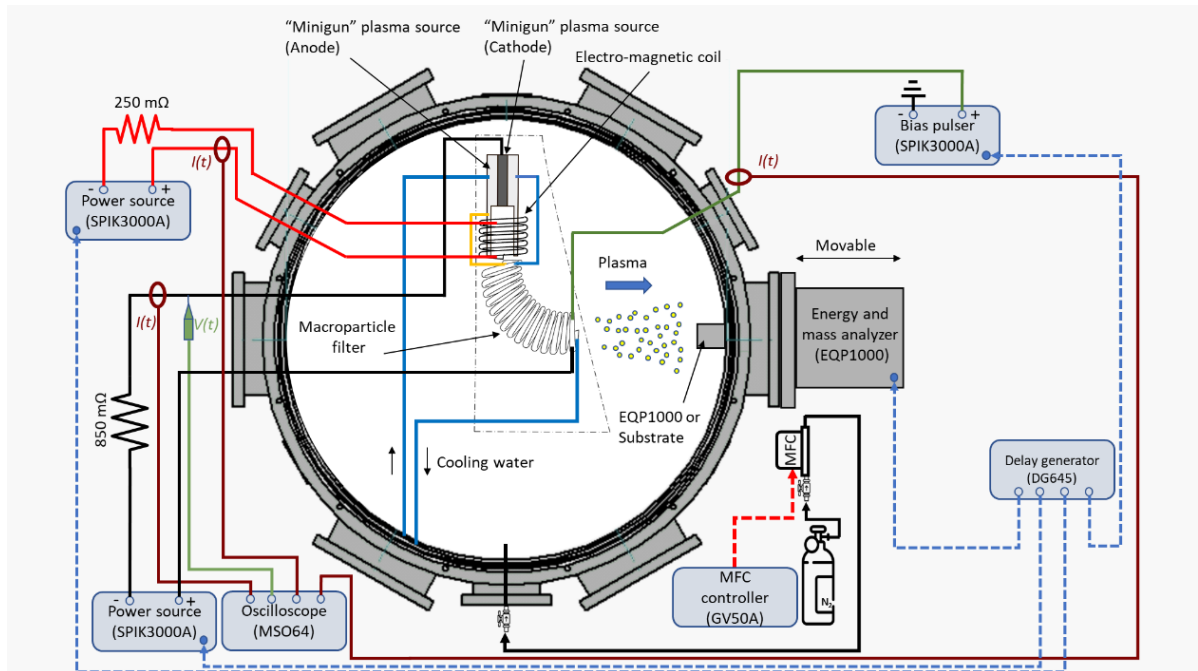


Figure 4-1 Experimental setup showing the minigun source with the electron-magnetic coil, macroparticle filter (not to scale).

The whole arc source setup was floating (electrically isolated). The minigun type source consisted of a cathode rod (aluminum 99.999%) with a 6.25 mm diameter mounted on the axis of the source. The

cathodic arc was ignited with a “triggerless” or “self-triggering” arc ignition method [129]. In this method, a ceramic with a metal-coated part (Figure 2-8) was inserted, creating a conducting path between the cathode and the anode. The coating had a specific resistance ($< 1\text{k}\Omega$) which was measured by a micro-ohmmeter (TTI BS407 by Aim). When voltage is applied, current can pass through the conducting surface of the metal coated part of ceramic, causing Joule heating at connecting points to the cathode. The Joule heating produces a hot spot where the coated ceramic is located and explosively forms plasma of the cathode materials. The produced plasma flows through a macroparticle filter (MPF). The MPF has two main roles: first, plasma transport, and second, elimination of macroparticles from the cathode [231]. The MPF consisted of a quarter-torus solenoid formed by a bent coil of 15 turns, which was connected to a non-metallic water tube for cooling the macroparticle filter and linked to the anode of the bias pulser. The minigun source was powered by a high pulse power generator (SPIK3000A by Melec GmbH). It was charged with a ground-free DC unit (GX50/1000 by ADL GmbH). The applied voltage was 400 V with 1 ms pulse width. The minigun source was placed to inject a plasma stream into the macro particle filter. All triggers were controlled by a delay generator (DG645 by Stanford Research Systems). The high power pulse generator was initially designed for high power impulse magnetron sputtering (HiPIMS) with an arc detection system. To avoid the arc suppression system, the arc current threshold value was set up higher, and a current-limiting 850 m Ω resistor was installed between the power supply and the cathode.

For the reference case, the minigun source was used without the pulsed EM-coil and plasma biasing. For the plasma biasing case, the bias pulse is separately powered by a high pulse power generator (SPIK3000A by Melec GmbH).

The voltage for plasma biasing of 30 V and 30 ms pulse width was applied between the outer part of the macroparticle filter and the ground. The 30 V is an empirical compensation value for the plasma biasing case to have comparable ion kinetic energy to the high charge state case.

For the high charge state case, the pulsed electro-magnetic coil (EM-coil) was used to determine the magnetic field near the anode. The EM-coil was powered separately with a 1.5 ms pulse width by a high pulse power generator (SPIK 3000A by Melec GmbH).

To limit the current through the EM-coil, a 250 m Ω resistor was used. The EM-coil reached up to about 800 A after triggering, which means that the magnetic field strength is about 0.2 T with 5 coil-windings around the anode body. Also, the trigger signal for EM-coil arrives 500 μs before the trigger for an arc minigun; the delay was empirically selected by looking at the arc burning voltage to have the effect of

the magnetic field on the plasma from the very beginning of the arc pulse. If the trigger signal is given at the same time, then the starting point of the EM-coil is influenced by the “Eddy current”.

The main plasma diagnostic tool was an energy-resolved mass spectrometer (ERMS, EQP- HE 1000 by Hiden Ltd), [145], [232], [233]. This setup allowed us to observe the ion energy distribution of plasma under three different configurations. The generated plasma is transported towards the grounded entrance of an ERMS, installed about 8 cm away from the exit of the macroparticle filter, at a flange of the main vacuum chamber. The diameter of the entrance orifice was 100 μm . The ERMS can measure the distribution of the energy-to-charge ratio E/Q for a specified mass-to-charge ratio M/Q , or vice versa, where E , M , and Q are the energy, the mass, and the charge number of the measured ions, respectively. Under three different configurations, the measured ion energy distribution can be an index of ion energy corresponding to the applied ion energy for film growth. By comparing the ion energy distribution and film characteristics, the effect of ion potential energy on film growth can be investigated.

The aluminum films were deposited on a silicon (100) substrate of 20 x 20 mm. The energetic aluminum ions move from the source to the silicon substrate through a macroparticle filter. During the film deposition, the substrate holder is placed at the center position of ion flux, instead of ERMS. Between the distance of ERMS and the macroparticle filter can be adjusted and the substrate holder is positioned at the same distance as the ion energy was measured through the ERMS, during deposition. The ERMS is fully moved back during the deposition.

The deposited film characterization was carried out by X-ray diffraction (XRD), X-ray reflectivity (XRR), atomic force microscopy (AFM), profilometry, and scanning electron microscope (SEM). The crystallinity of the deposited Al films on a silicon substrate was measured by a grazing incidence X-ray diffraction (GI-XRD, Rigaku Ultima IV). The grazing incidence X-ray diffraction measurements are conducted at 1° incidence angle, from 10° to 90° , with a step time of 1 s/step and step size of 0.05° . The film thickness, density and surface roughness were measured by X-ray reflectivity (XRR, Rigaku Ultima IV). The XRR patterns were measured at 1° incidence angle with a step size of 0.05° and a scan time of 1 s/step. The XRR data were fitted to extract information on film (thickness, density and surface roughness) with the Global fit software [234]. The GI-XRD and XRR measurements are performed by using Cu radiation sources at 40 kV and 40 mA in a parallel beam geometry. The film surface morphology was measured by atomic force microscopy (AFM, Bruker Dimension ICON). The scanned area of Al film was $2\ \mu\text{m} \times 2\ \mu\text{m}$ with a resolution of 1024×1024 pixels, and further surface morphology of the Al films was investigated by a scanning electron microscope (SEM).

4.4 Plasma diagnostics

4.4.1 Voltage and current characteristics analysis

Voltage and Current (Rogowski) probes

The burning voltage between the cathode and anode was measured using two passive high voltage probes (TPP0850 by Tektronix) between the electrodes and the ground. The high voltage probes can be used up to 2.5 kV (peak value) with a bandwidth of 800 MHz. Such voltage probes have a voltage divider to reduce the measured voltage (by the factor of 50 in this case) to certain levels for the protection of devices such as oscilloscopes. The voltage drop or cathode fall is present during the ignition process in the measured voltage data. The magnitude of the voltage drop depends on cathode material, and the voltage drop is necessary to maintain the discharge. The arc current can be measured using a Rogowski coil (model Chauvin arnoux MA 200, a sensitivity of 0.001 V/A, and an available frequency range from 5 Hz to 1 MHz in this case). A Rogowski coil can support a direct measurement of the arc current flowing through its center.

4.4.2 Energy-resolved mass spectrometry

Measuring ion energy distributions

Ions accelerate near the cathode spots [233], and the accelerated ions reach a specific location with plasma expansion having energy in a certain range. In order to measure the ion energy distribution, a specific analyzer is required, like an energy-resolved mass spectrometer (ERMS), which is comprised of an electrostatic ion energy analyzer and a quadrupole mass spectrometer [235], [236].

The ERMS can measure the distribution of the mass-to-charge ratio M/Q for a specified energy-to-charge E/Q , or vice versa, where E , M , and Q are the energy, the mass, and the charge number of the measured ions, respectively. A schematic overview of the commercial ERMS (EQP-1000 by Hiden Ltd.) device with a combined high transmission ion energy analyzer and quadrupole mass spectrometer is shown in Figure 4-2.

The ERMS has a grounded entrance: a small hole (100 μm) through which the ion species enter. The device is differentially pumped to maintain lower pressure compared to the plasma source area. There is a potential difference between the entrance (V_{entrance}) of ERMS and plasma (V_{plasma}), which has a certain potential that produces a sheath [1]. In the sheath, there is a voltage drop which is the main

energy source of ion acceleration ($V_{\text{plasma}} > V_{\text{entrance}}$) or ion deceleration ($V_{\text{plasma}} < V_{\text{entrance}}$) toward ERMS [1], [233]. Normally, if the plasma potential is not negative, the ions accelerate toward ERMS with energy gained between plasma and the entrance orifice of ERMS. The energy gain is determined by [1], [233]

$$\Delta E_{\text{kin}}(Q) = Qe(V_{\text{plasma}} - V_{\text{entrance}}) \quad (4.2)$$

where, E_{kin} is ion kinetic energy, Q is the charge-state number, and e is the elementary charge. The ERMS can measure the kinetic energy distributions of ions from plasma, which reach the device orifice, and the energy distribution can be obtained separately dependent on the ion charge state.

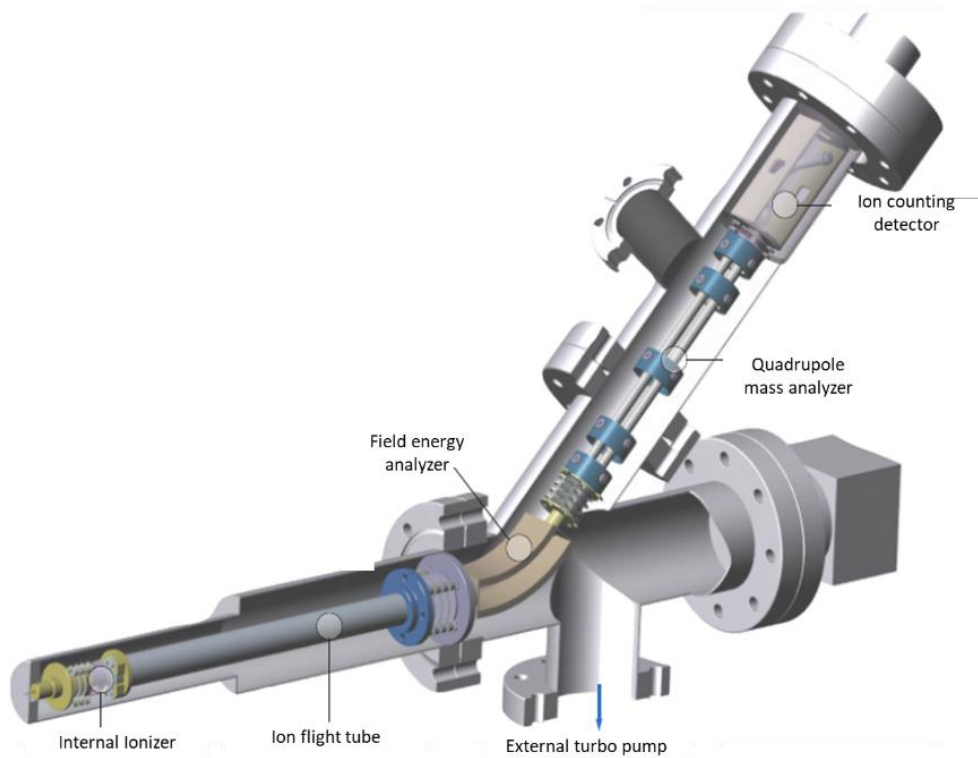


Figure 4-2 Schematic overview of the Hiden EQP Energy-resolved spectrometer. The used device can detect ions with masses up to 1000 atomic mass units with a precision of 0.01 amu [237].

In this thesis, the ERMS was installed in the vacuum chamber and used to measure the ion energy distribution for the cases of reference, high charge state, and plasma biasing. Especially through the comparison of measured energy distributions, it can be found whether high charge state and plasma biasing cases have comparable ion kinetic energy or not. This comparison allowed us to obtain empirical plasma biasing voltage. The detailed results will be shown in chapter 4.5.2.

4.5 Plasma characterization results

4.5.1 Voltage and current characteristics

The voltage and current characteristics were measured by a passive voltage probe (TPP0850 by Tektronix) and Rogowski coil (MA200 by CHAUVIN ARNOUX), respectively. The data was captured in sample mode and stored in a digital oscilloscope (MSO64 by Tektronix). The measured voltage and current waveforms are shown in Figure 4-3.

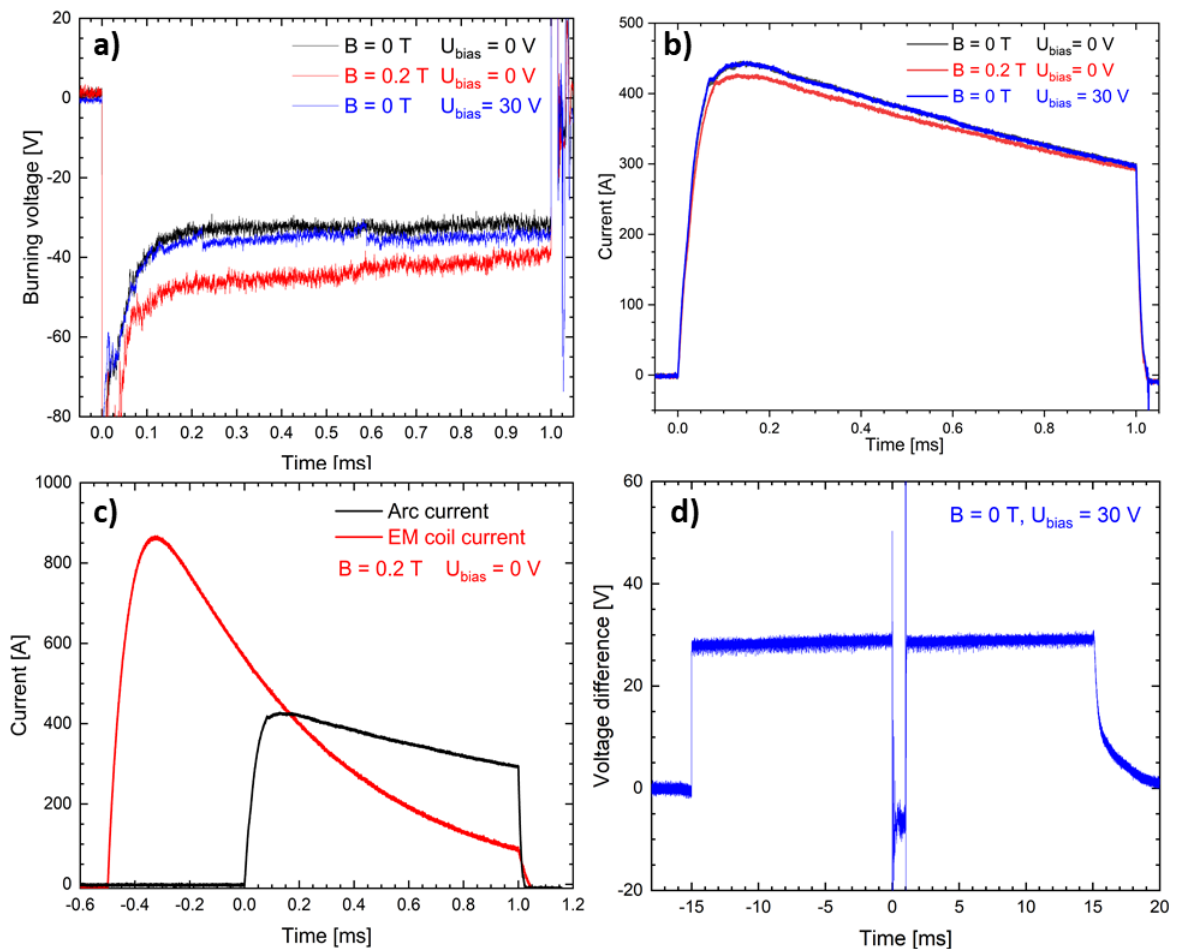


Figure 4-3 (a) Measured burning voltage of three different configuration conditions (Black graph: reference case in absence of external magnetic field and plasma biasing, Red: the presence external magnetic field, Blue: plasma biasing case); (b) Measured current waveform; (c) Measured arc current and electric magnetic coil current; (d) Measured voltage difference between the arc cathode and ground (ERMS) for plasma biasing case where the pulse is in the middle of the bias pulse.

There are four different measured plots in Figure 4-3. The measured burning voltage and current under three different configurations are shown in Figures 4-3(a) and (b), respectively. All cases have the same 1 ms pulse width. The burning voltage value is about 35 V for the reference and plasma biasing cases. However, the high charge state case (presence of external magnetic field) has a higher burning voltage (50 V) than the other cases. This is because of the higher plasma impedance [1], [134], [135]–[137]. While the current has the opposite trend: the measured current value is about 450 A for the reference and plasma biasing case, but the case of the high charge state is about 425 A. Figure 4-3(c) shows the delay between the main arc current and the external magnetic coil (EM-coil). The delay was 0.5 ms which was empirically selected. For the delay, the condition gave the proper effect of the external magnetic field to the ignition process (This delay was determined empirically to avoid eddy current effect). Figure 4-3(d) shows that the measured burning voltage for the plasma biasing case, the biasing voltage was fixed at 30 V with 30 ms pulse width, and the arc ignition occurred with the burning voltage of about 35 V with 1 ms pulse width after 15 ms later after the biasing signal. The bias pulse is much longer than EM-coil and arc ignition pulse to make the biasing pulse (30 ms) have a constant voltage on the time scale of EM-coil pulse (1.5 ms) and arc ignition pulse (1 ms).

After applying pulsed voltage from the voltage source for the typical case, the space between cathode and anode is being charged and the voltage starts increasing. The increased voltage makes the current rising rapidly until the voltage drops to the burning voltage range. The voltage drop has a different delay and value between the reference case the high charge state case, as shown in Figure 4-4.

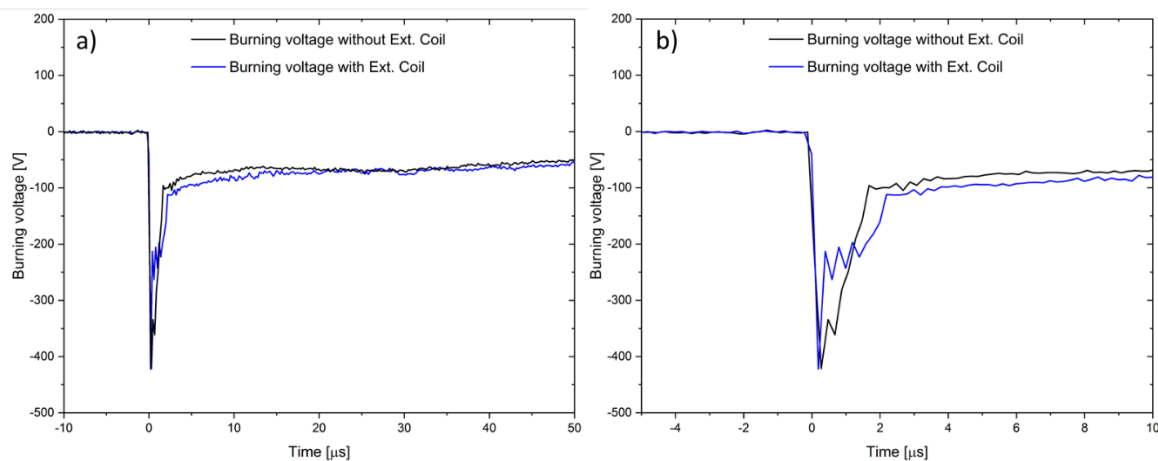


Figure 4-4 Comparison of burning voltage graphs for normal (black line) and presence of external magnetic field case (blue) with different view window (a) from $-10 \mu\text{s}$ to $50 \mu\text{s}$; (b) from $-5 \mu\text{s}$ to $10 \mu\text{s}$.

The typical case and the presence of external magnetic field case have different rising times until reaching maximum current because the external magnetic field blocks the electron flow to the anode. Due to the nature of the discharge, the electrons tend to go to the anode, but the electrons confined in the external magnetic field is required a higher voltage to escape the magnetic field, which leads to a higher burning voltage.

In a recent study of voltage-current phase development of a vacuum arc with nanosecond resolution by an ultra-fast camera [27], four different phases (charging, rising, steady, and decay) were investigated during the arc development. According to the result, the most affected phase was the rising phase, the rising phase time was getting longer with increasing distance between cathode and anode. Also, the rising phase time was correlated with the cathode spot emission radiance. The rising phase time increased for the presence of the external magnetic field. Therefore, the radiance of the cathode spot emission could be delayed, and the burning voltage was higher in the case of the presence of an external magnetic field.

4.5.2 Ion energy distribution

Figure 4-5 shows the measured energy distribution of Al^+ ions, Al^{2+} ions, and Al^{3+} ions under three configurations. The energy distributions show that a maximum value is in a different energy range. The Al^+ ions have a maximum value between 25 eV and 50 eV, the Al^{2+} ions between 50 eV and 100 eV, and Al^{3+} has between 75 eV and 125 eV for this experiment. The maximum value means that the particles with corresponding kinetic energy are present most. The kinetic energy is approximately proportional to the ion charge state, clearly shown in Figures 4-5. Figure 4-5 shows that the curve for Al^+ has the maximum value at about 40 eV, the curve for Al^{2+} has the maximum value at about 80 eV, and the curve for Al^{3+} has the maximum value at about 110 eV. From the measured ion energy distributions, it is shown that the typical kinetic energy of ions in the plasma biasing case can be matched to the high charge state while having different charge state distributions, which mean different ion potential energies. Therefore, the ion potential energy effect can be investigated by comparing deposited film characteristics under different configurations.

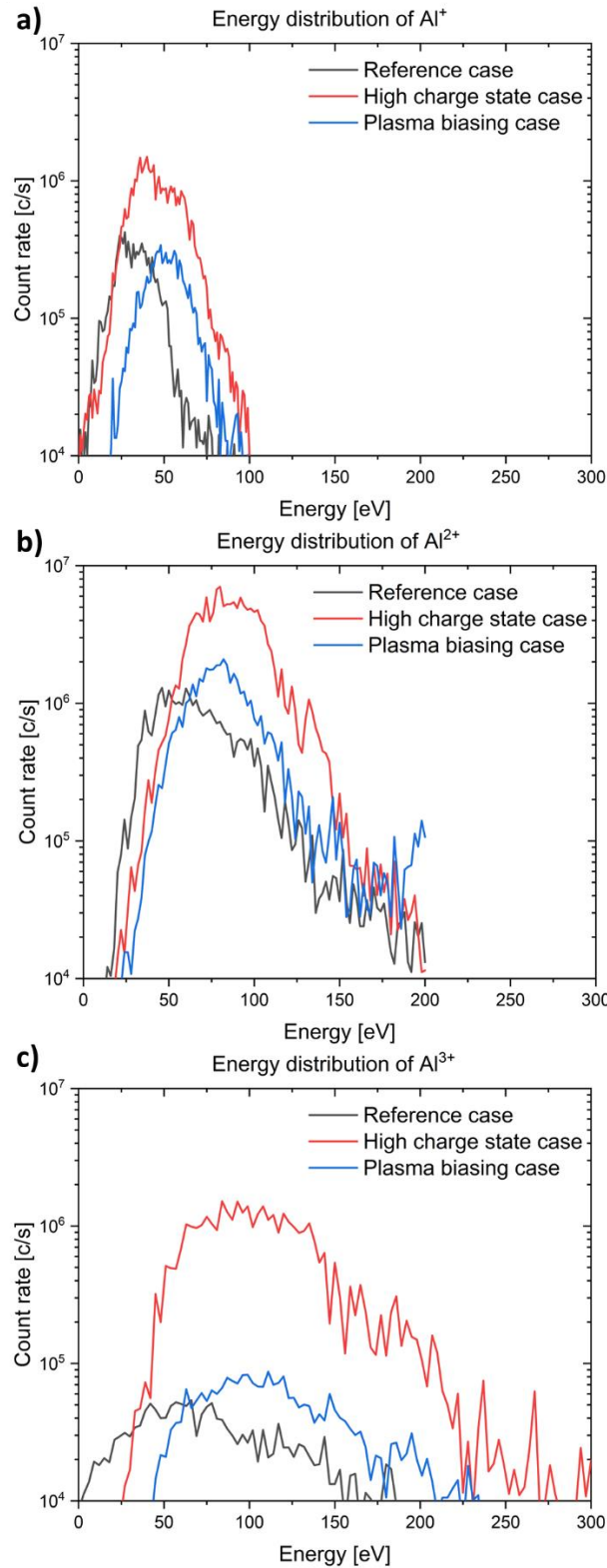


Figure 4-5 Measured energy distribution of species under three different configurations; (a) the energy distribution of Al⁺, (b) the energy distribution of Al²⁺; (c) the energy distribution of Al³⁺. The black curve is the reference case, the red curve is the high charge state case, and the blue curve is the plasma biasing case. The arc current was about 450 A with 1 ms pulse width. (Mass-to-charge ratios of M/Q = 26.98 u for Al⁺ ions, M/Q = 13.49 u for Al²⁺ ions, and M/Q = 8.99 u for Al³⁺ ions, the intensities obtained are corrected for the mass sensitivity of the ERMS).

The potential energy can be estimated through equation 2.22, and the main determining factor of the potential energy are the charge states (Q). The ion charge state distribution is calculated based on energy distribution data, as shown in Table 4-1. According to the data, the fraction of Al^+ is lower in both the case of high charge state and plasma biasing than the case of the reference. The fraction of Al^{2+} is lower in the case of the high charge state than others, and the case of plasma biasing has a similar value compared to the case of reference. For the fraction of Al^{3+} , the case of high charge state shows about 19 % higher values compared to the case of reference and plasma biasing. The average charge states are estimated, as well, and the values are 1.94, 2.16, and 1.99 for the case of reference, high charge state, and plasma biasing, respectively. The average charge state is not much changed. However, the amount of Al^{3+} is significantly (about 19 %) increased in the case of a high charge state. This has a strong effect on the application of cathodic arc because the ionization energy is the most dominant potential energy term, and the ionization energy is a cumulative energy value like Al^+ : 5.99 eV, Al^{2+} : 24.8 eV, and Al^{3+} : 53.5 eV [42]. The approximate ion potential energy can be estimated based on the obtained charge state distribution and cumulative ionization energy value. The estimated ion potential energy is about 27.7 eV, 33.8 eV, and 28.8 eV for reference, high charge state, and plasma biasing case, respectively in the current experiment. The value is calculated based on the measured ion energy distribution data. The distribution ratio of Al^+ , Al^{2+} , and Al^{3+} among the total ion energy distribution is obtained through the measured ion energy distribution graph of each case. The final ionization energy is estimated through the known ionization energy of the ionization step and the distribution ratio of ions, and the final estimated ion potential energy is calculated using equation 2.22. (The excitation energy of the bound electron is neglected). The estimated ion potential energy increased about 22 % for the high charge state case compared to the reference case and about 3 % for the plasma biasing case. Therefore, the case of a high charge state has the highest mean ion potential energy.

Table 4-1 The estimated charge state distribution which are based on the measured energy distribution data.

	Reference case [%]	High charge state case [%]	Plasma biasing case [%]
Al^+	12.8	9.4	8.8
Al^{2+}	80.6	65	83.4
Al^{3+}	6.6	25.6	7.8

4.6 Film characterization results

The effect of ion potential energy cannot be confirmed simply by only performing plasma diagnostics. In order to understand the ion potential energy effect on film growth, it is necessary to simultaneously investigate the properties of the deposited film and plasma processes. For this purpose, aluminum films were deposited in the reference, the high charge state, and the plasma bias cases. The films were deposited on Si (100) substrate. The deposited films were characterized by X-ray diffraction analysis (XRD), X-ray reflectometry (XRR), atomic force microscopy (AFM), profilometry, and scanning electron microscope (SEM).

4.6.1 X-ray diffraction (XRD) and X-ray reflectivity (XRR) analysis

Figure 4-6 shows the GI-XRD patterns of Al films grown with different configurations (the reference case, the high charge state case, and plasma biasing case) with similar film thicknesses around 60 nm. Figure 4-6(a) shows that there is a common peak for all the configurations along the (111) direction. However, there is an additional growth direction (220) when the film is deposited in the case of the high charge state. This result could be related to the ion potential energy because the ion potential energy increased about 22 % for the high charge state case compared to the reference case. It could change the ratio of ion potential energy to kinetic energy per incident particle [47].

The plasma biased case and the reference case show similar peak positions, but the peak has an intensity difference in the (111) direction. Figure 4-6(b) shows the measured XRD pattern of two films of the high charge state case with different thicknesses (60 nm and 120 nm) under the same growth configuration ($B = 0.2$ T, $V_{\text{bias}} = 0$ V). The XRD results show that the peaks for 120 nm film have higher intensity in (200) and (220) directions, but the peak intensity is comparable in (111) direction, as shown in Figure 4-6(b). It means that the film growth does not occur in the (111) direction anymore, but the film grows in the (200) and (220) directions, and most strongly in the (220) direction. This result is a little deviation from the standard XRD patterns of aluminum powder [238], deposited film by DC magnetron sputtering [239], [240], and by a cathodic arc [241]. In the result of standard XRD patterns of aluminum, the preferred orientation of aluminum film is (111) direction, and the intensity of (111) direction is 4 times higher than the (220) direction. For the film deposited by DC magnetron sputtering with 150 nm [239] and 2.5 μm [240] thickness, the intensity of the peak along the (111) direction is vigorous, but the intensity of the peak along the (222) direction is very weak. For the film deposited by a pulsed cathodic arc with 1.5 μm [241], it shows a similar trend as well.

The previous results showed a similar trend to the standard powder result even with different deposit techniques. Also, the film thickness is not the same in each case. Therefore, the XRD result obtained in this experiment could be considered as an effect of ion potential energy rather than an effect of film thickness.

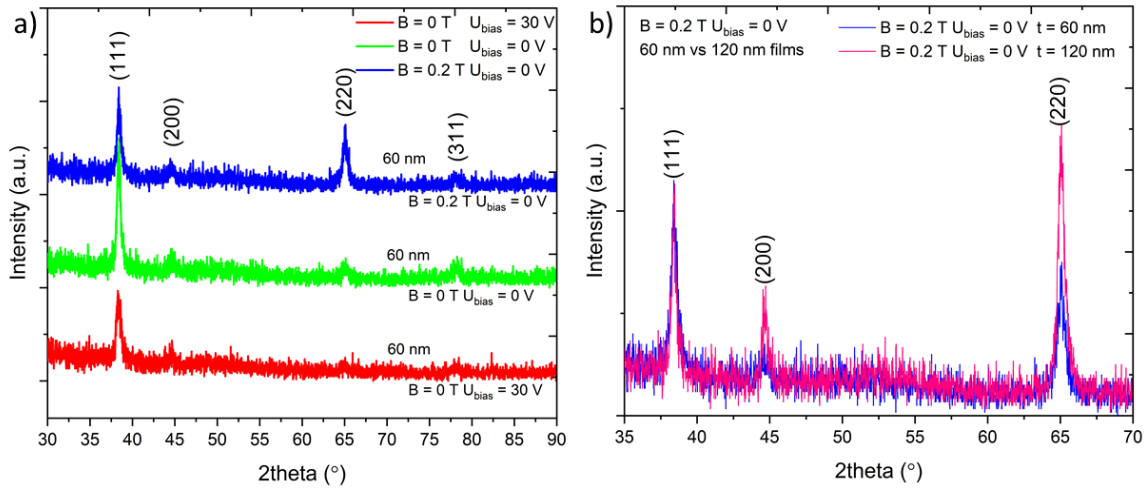


Figure 4-6 The GI-XRD patterns of Al thin films deposited on Si substrate. (a) The three different configuration cases (the green is a reference case, the blue one is a high charge state case, and the red one is a plasma biasing case.) with the same film thickness about 60 nm. (b) Comparison of the GI-XRD patterns of Al for the high charge state case with different film thicknesses. (The measured film thickness by profilometer is 60 nm for the blue curve, and 120 nm for the pink curve).

To quantify the degree of crystallinity of film orientation, equation 4.3 was used, where $\sum I_{tot}$ is the integrated area of the entire X-ray diffractogram, $\sum I_{net}$ is the integrated area under crystalline XRD peaks, and $\sum I_{cons.bgr}$ is the background of the diffractogram [242]:

$$Degree\ of\ crystallinity = \left(\frac{\sum I_{net}}{\sum I_{tot} - \sum I_{cons.bgr}} \right) \times 100 \quad (4.3)$$

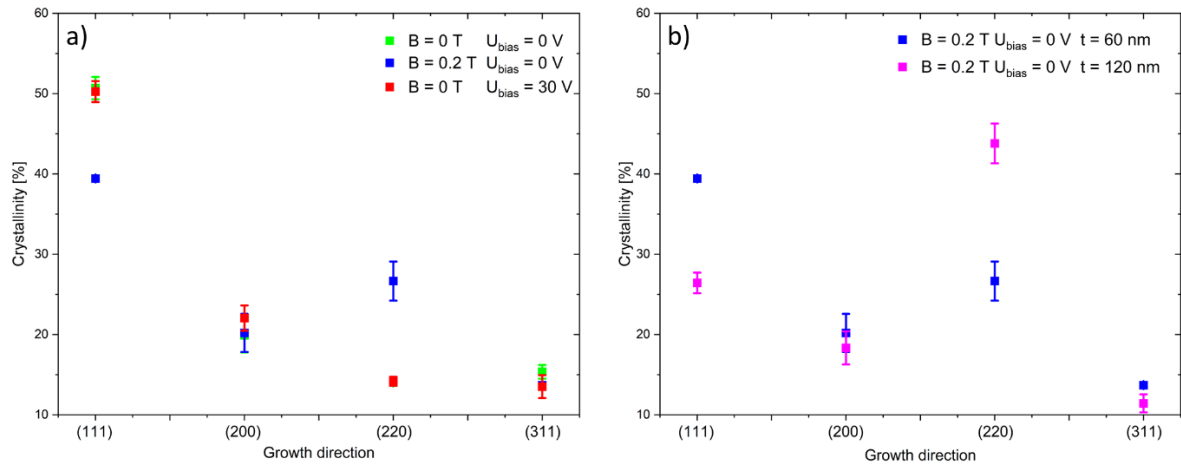


Figure 4-7 (a) The evaluated degree of crystallinity of film orientation for the Al films with three different configurations. (The green rectangular is for reference, the blue rectangular is the case of high charge state, and the red rectangular is the case of plasma biasing); (b) The evaluated degree of crystallinity of the Al film with different film thickness for the case of high charge state. (The blue rectangular is for the 60 nm thickness and the magenta rectangular is for the 120 nm thickness).

The degree of crystallinity was calculated based on the measured XRD data for Al films. It was found that the degree of crystallinity of Al films along the (111) direction decreased about from 51 % to about 40 % and increased (220) direction from about 14 % to 27 % for the high charge state case as shown in Figure 4-7(a). Also, this trend was confirmed by the thicker Al film of the high charge state case, as shown in Figure 4-7(b). The degree of crystallinity for the thicker Al film along the (111) direction reduced from about 40 % to about 27 % and increased from about 27 % to about 44 % for the (220) direction.

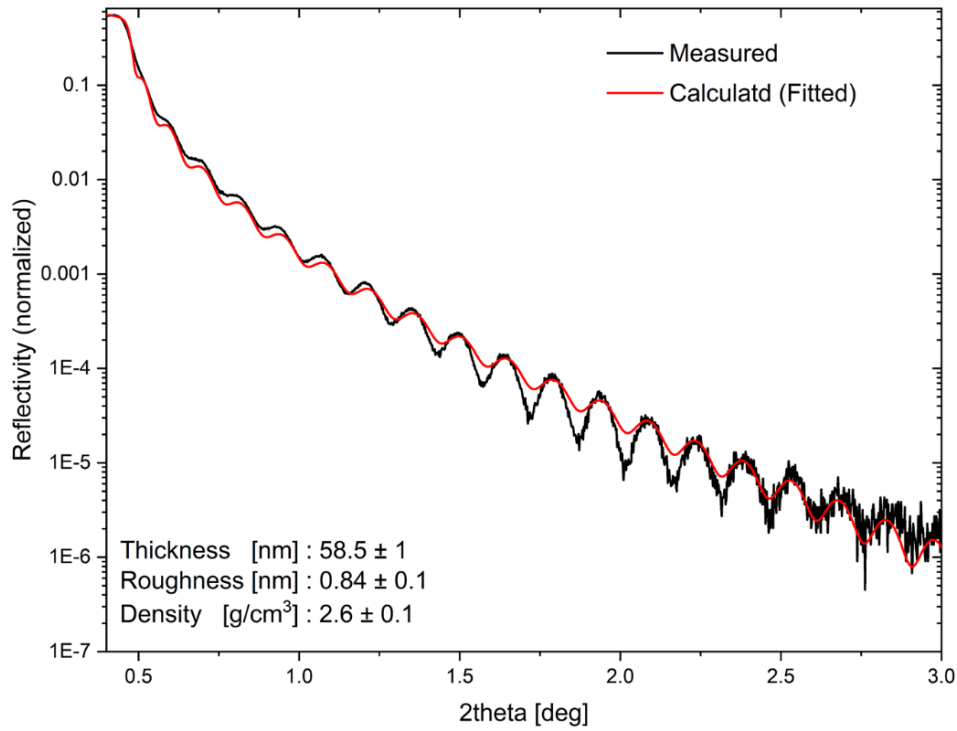


Figure 4-8 The measured and fitted XRR data of Al film for the high charge state case

The measured and fitted XRR data for the high charge state case is shown in Figure 4-8. From the XRR measurement, film properties were obtained, as shown in Table 4-2. The film thickness, measured by XRR, is about 60 nm for the high charge state and plasma biasing cases, in agreement with those measured by the profilometer. The thickness data could not be obtained for the reference case due to the high roughness of the film. The estimated density is about 2.6 g/cm³ for all the cases, which are considered dense (for comparison: bulk density of aluminum: 2.7 g/cm³).

Table 4-2. The thickness (nm), roughness (nm), and density of aluminum (g/cm³) obtained through the Global fit software [234] based on XRR measurements. (The proper thickness and roughness data of the reference case were not obtained due to roughness of the film).

Sample	B-field [T]	Plasma bias [V]	Thickness [nm]	Roughness [nm]	Density of aluminum [g/cm ³]
Reference case	0	0	-	-	2.55 ± 0.1
High charge state case	0.2	0	58.5 ± 1	0.84 ± 0.1	2.60 ± 0.1
Plasma biasing case	0	30	60.0 ± 1	1.00 ± 0.1	2.60 ± 0.1

4.6.2 Atomic force microscopy (AFM) analysis

The AFM topographic image of the Al film is shown in Figure 4-9. The calculated root-mean-square roughness (R_q) is 4.0 nm for the reference case. Only the reference case of the AFM topographic is measured, as shown in Figure 4-9. This is because the high charge state and the plasma biasing cases show a roughness measured by XRR (below 1 nm) as presented in Table 4-2. Therefore, considering to the results AFM and XRR, the feature size on the top surface of the reference case is expected to be bigger than the other cases.

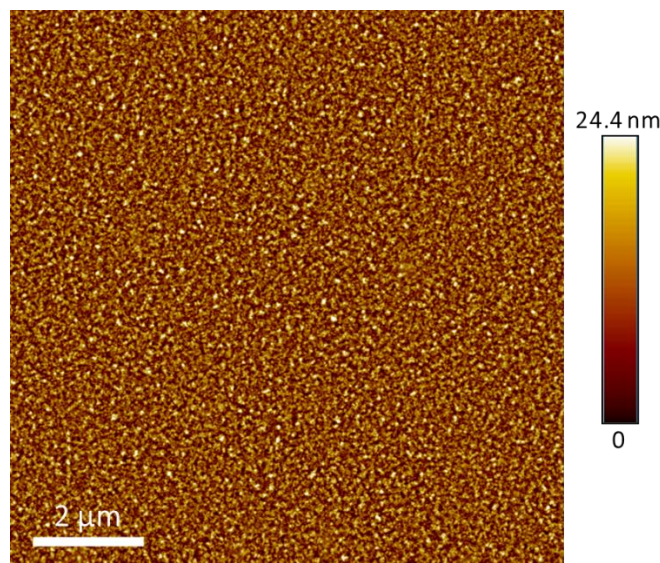


Figure 4-9 AFM image of Al films on silicon substrate for the reference case ($B = 0$ T, $U_{\text{bias}} = 0$ V) in false color.

4.6.3 Scanning electron microscope (SEM) analysis

Figure 4-10 shows SEM images of the Al film surface deposited on silicon. According to the SEM images, the typical feature size of the film is smaller for the high charge state case (Figures 4-10(c), (f), and (i)) compared to the reference case (Figures 4-10(a), (d), and (g)). This result was supported by the AFM data. In the case of the plasma biasing, the surface morphology was found as shown in Figures 4-10(b), (e), and (h). It shows a different morphology as compared to the reference and the high charge state case. Further investigation is needed to clearly understand this result. Also, there are black spot observations as shown in Figures 4-10(a), (b), and (c). The number of the black spots was observed more for the case of the reference compared to the others. The cause of this result is not obviously known, requiring further investigations. According to the theoretical investigations in literature,

molecular dynamics simulation [203], the higher ion potential energy of ions lead to a slightly lower interface mixing and fewer point defects [203]. This can lead that the collision pattern is changed near the substrate surface in case of the higher ion potential energy [203], which could be a reason of the structural changes in thin films.

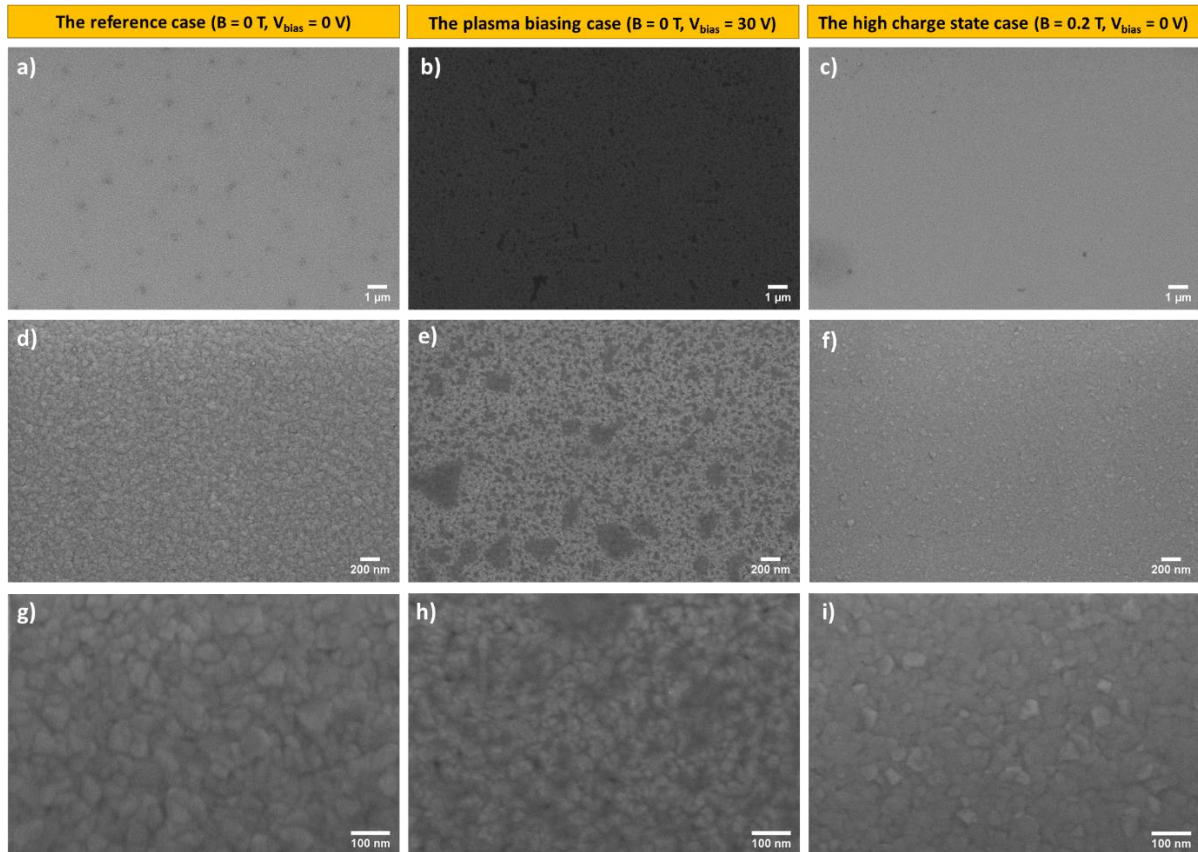


Figure 4-10 The surface morphology of SEM images of Al films deposited on silicon substrate under three different configurations. The reference case is (a), (d), and (g). The plasma biasing case is (b), (e), and (h). The high charge state case is (c), (f), and (i).

The XRD analysis of the Al films showed that the films grow along the (220) direction after a certain film thickness in case of the high charge states. Therefore, the cross-section of the growth films on silicon substrates was investigated for further understanding. The cross-section of morphology of the Al films on the silicon substrate is shown in Figure 4-11.

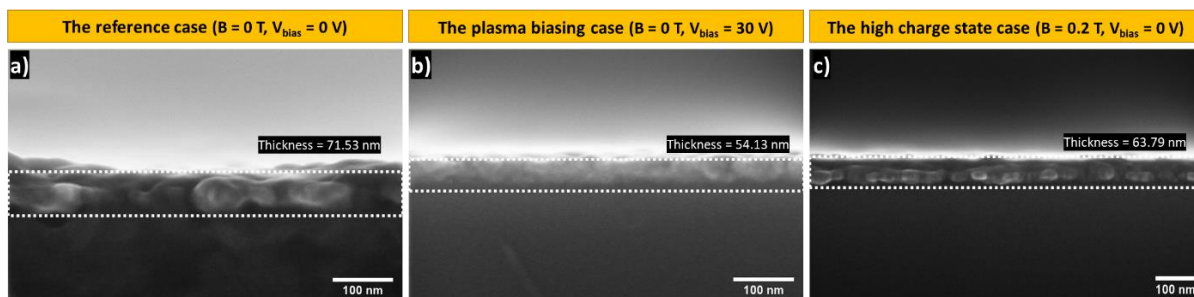


Figure 4-11 (a) Cross section SEM images of Al thin films deposited on silicon substrate under three different configurations the reference case; (b) the plasma biasing case, and (c) the high charge state case.

Contrary to the results shown in the XRD data in Figure 4-8, no preferential film growth was found due to very small grain size and the resolution of SEM is not enough to resolve such small features. The thickness of the Al film obtained through the SEM is in agreement with the XRR and profilometer obtained previously.

4.7 Discussion and conclusions

The effect of ion potential energy on film growth was studied by tuning ion charge states. The ion potential energy is known to lead to “atomic scale heating” [42], [46], and studies on this have not been conducted much. In particular, in the plasma of a cathodic arc with higher ion charge states, the role of ion potential energy is more significant due to the presence of multiply charged ions. The total energy strongly depends on charge state, which affects both ion kinetic and potential energy. For example, with a high charge state, ion kinetic and potential energy have higher energy compared to a low charge state.

In order to understand the ion potential energy effect on film growth, proper experiments were required, which were capable of tailoring the ion energy. To satisfy the requirement, an experiment with three different conditions was conducted. These conditions allowed us to tune the charge state. Finally, the experiments were carried out by having three different configurations: reference case, high charge state case, plasma biasing case. Here, the ion potential energy was controlled by an indirect approach, namely, changing the ion charge states. In the case of the high charge state, high ion kinetic and potential energy were obtained compared to the reference case, and in the case of the plasma biasing case, the ion potential energy was similar to the reference case, but the ion kinetic energy was comparable to the high charge state case. The ERMS measured the ion energy distribution

to confirm that the ion energy was properly adjusted. The calculated mean ion potential energy follows about 27.7 eV for the reference case, about 33.8 eV for the high charge state case, and about 28.8 eV for the plasma biasing case. The high charge state case has a higher ion potential energy compared to the others.

The aluminum films were deposited with designed ion energy distribution under the same three configurations. The deposited aluminum films were characterized by X-ray diffraction (XRD), X-ray reflectivity (XRR), atomic force microscopy (AFM), profilometry and scanning electron microscope (SEM). According to the XRD results, the three deposited films have crystalline structures, and the common peak is observed along (111) direction. However, the preferential growth along the (220) direction is only found in the case of the high charge state with high ion kinetic and potential energies compared to other cases, after a certain film thickness. The evaluated degree of crystallinity based on the XRD pattern also supports the phenomenon. The degree of crystallinity in the (220) direction accounts for about 27 % of the high charge state case, while the other cases occupy about 14 % of the total structural composition. This trend obviously is confirmed by comparing the two XRD patterns of films with different thicknesses of the high charge state cases (60 nm and 120 nm). For the 120 nm case, the degree of crystallinity (in 220) direction is about 44 %, i.e., higher by about 17 % than the 60 nm one. Through observed material characterization, it could be considered that the high ion potential energy may affect the preferential growth direction thin film or polycrystalline growth. Namely, the overall average charge states are not increased significantly, but due to the increased ion potential energy (increase about 22%, from the reference case to the high charge case), the collision pattern is changed [203], and the ratio of ion potential energy to kinetic energy per incident particle is influenced [47]. This shifts the energy balance further toward the ion potential energy, which can be predicted to lead the film growth towards having a preferential direction [243] or a polycrystalline growth.

The effect of ion potential energy on film deposition has been investigated through the combination of film characterization and plasma diagnostics. The presented results show there is an effect of potential energy changes between the different conditions, and this has an effect on the film properties. These results here can be considered first preliminary results for the following deeper investigations on thin films to understand the correlation between the ion potential energy and the film deposition.

5. Summary and conclusions

This thesis aimed to investigate two main questions. The first question is to investigate the appearance of cathodic arc spot motion in a vacuum or gas atmosphere (reactive and noble gas) with very high temporal and spatial resolution and to find the answer to whether or not cathodic arc spots have periodic characteristic times between spot ignitions, which is one of the open fundamental questions. The second goal is to understand if and how much the ion potential energy affects film deposition, especially when using pulsed cathodic arc deposition since here we deal with multiply charged ions. The ion potential energy is high and cannot be ignored in the cathodic arc process due to the high charge states, which is one of the characteristics of the cathodic arc process. To answer these questions, proper and various plasma diagnostics have been applied.

For observation of cathodic arc spot, a combination of a long-distance microscope and streak camera system was used. The system allowed us to take high spatial and temporal resolution streak images. The appearance of cathodic arc spot motion in different atmospheres has been shown to be related to two well-known types of cathode spots: “type 1” for the reactive gas (N_2 , O_2) atmospheres and “type 2” for the vacuum and noble gas (Ar) atmosphere. The observed cathode spots in streak images have interesting features of apparent motion, for example, the spots tend to strongly appear in clusters of groups for vacuum and noble gas (Ar) in the retrograde direction, and the cathode spots look like “connected chains” when operating in a reactive gas (N_2 , O_2), especially, the spots ignited in oxygen do not show a preferential direction of ignition; neither the Amperian nor retrograde direction.

The fluctuations of the light emitted by the cathode spot from the obtained streak images were analyzed with the fast Fourier transformation, leading us to a spectral power density that can be fitted to a power law with a colored random noise (CRN) index near 2 (slope of the broad spectrum) in vacuum and noble gas (Ar). The physical meaning of this analysis can be concluded that the cathode arc spot ignited stochastically like steps in the Brownian motion, and there is no specific characteristic spot lifetime. This result can be described in the framework of a fractal model. The self-similarity, which is a characteristic of the fractal model, was also confirmed through the appearance of spot motion observed at different sweep times. Through the FFT analysis for the streak images, the CRN index for noble gas has a similar value to the vacuum case. The CRN index decreases with increasing process pressure for the reactive gas atmospheres (N_2 , O_2), which is indicating that the spot ignition with low-frequency events declines compared to high-frequency events. A detailed description of the experiment and results are provided in Chapter 3.

For investigation of the ion potential energy effect on film deposition in chapter 4, three different configuration experiments were conducted. The three different configurations were categorized: the reference case, the high charge state case, and the plasma biasing case. The high charge state case has a higher kinetic and potential energy of ions compared to the reference case, and the plasma biasing case has comparable kinetic energy of ions to the high charge state case and similar potential energy of ions to the reference case. The high charge state and plasma biasing cases have a similar value of kinetic energy of ions, while the potential energy of ions has a quite different value. The energy distribution of ion kinetic energy was measured by energy-resolved mass spectroscopy, and the strength of ion potential energy was estimated relatively based on the measured energy distribution data. Through the ERMS measured, it was confirmed that the tuning of the ion kinetic energy was suitable.

To investigate the effect of ion potential energy, aluminum films were deposited on silicon substrates with three different corresponding energy for the three different cases. The deposited aluminum films were characterized by X-ray diffraction (XRD), X-ray reflectivity (XRR), atomic force microscopy (AFM), profilometer, and scanning electron microscope (SEM), as discussed in chapter 4. According to the combination of film characterization and plasma diagnostics, the ion potential energy could affect the film growth's preferential direction or lead to a polycrystalline growth. This finding could serve as a starting point for further research into the correlation between ion potential energy and film deposition.

Bibliography

- [1] A. Anders, *Cathodic Arcs From Fractal Spots to Energetic Condensation*. New York: Springer, 2008.
- [2] M. A. Lieberman and A. J. Lichtenberg, *Principles of Plasma Discharges and Materials Processing*. New Jersey: WILEY, 2005.
- [3] I. Beilis, *Plasma and Spot Phenomena in Electrical Arcs*. Cham: Springer, 2020.
- [4] P. G. Slade, *The vacuum interrupter: Theory, design, and application*. Boca Raton: CRC Press, 2007.
- [5] R. Bini, B. M. Colosimo, A. E. Kutlu, and M. Monno, "Experimental study of the features of the kerf generated by a 200 A high tolerance plasma arc cutting system," *J. Mater. Process. Technol.*, vol. 196, no. 1–3, pp. 345–355, 2008, doi: 10.1016/j.jmatprotec.2007.05.061.
- [6] S. R. K. Rao, G. M. Reddy, and K. P. Rao, "Effects of thermo-mechanical treatments on mechanical properties of AA2219 gas tungsten arc welds," *J. Mater. Process. Technol.*, vol. 202, no. 1–3, pp. 283–289, 2008, doi: 10.1016/j.jmatprotec.2007.08.070.
- [7] I. G. Brown, "Cathodic arc deposition of films," *Annu. Rev. Mater. Sci.*, vol. 28, no. 1, pp. 243–269, 1998, doi: 10.1146/annurev.matsci.28.1.243.
- [8] I. Kleberg, "Die Dynamik von kathodischen Brennflecken im externen Magnetfeld," Humboldt University Berlin, 2001.
- [9] J. E. Daalder, "Random walk of arc cathode spots in vacuum," *J. Phys. D. Appl. Phys.*, vol. 16, no. 9, pp. 17–27, 1983, doi: 10.1088/0022-3727/16/9/002.
- [10] E. Hantzsche, B. Jüttner, and H. Pursh, "On the random walk of arc cathode spots in vacuum," *J. Phys. D. Appl. Phys.*, vol. 16, pp. L173–L179, 1983, doi: 10.1088/0022-3727/16/9/002.
- [11] B. E. Djakov and B. Jüttner, "Random and directed components of arc spot motion in vacuum," *J. Phys. D. Appl. Phys.*, vol. 35, no. 20–21, pp. 2570–2577, 2002, doi: <https://doi.org/10.1088/0022-3727/35/20/316>.
- [12] B. Jüttner, "The dynamics of arc cathode spots in vacuum. Part III: Measurements with improved resolution and UV radiation," *J. Phys. D. Appl. Phys.*, vol. 31, no. 14, pp. 1728–1736, 1998, doi: 10.1088/0022-3727/31/14/017.
- [13] I. Beilis, B. E. Djakov, B. Jüttner, and H. Pursch, "Structure and dynamics of high-current arc cathode spots in vacuum," *J. Phys. D. Appl. Phys.*, vol. 30, no. 1, pp. 119–130, 1997, doi: 10.1088/0022-3727/30/1/015.
- [14] Z. Shi, S. Jia, L. Wang, Q. Yuan, and X. Song, "Experimental investigation on the motion of cathode spots in removing oxide film on metal surface by vacuum arc," *J. Phys. D. Appl. Phys.*, vol. 41, no. 17, 2008, doi: 10.1088/0022-3727/41/17/175209.
- [15] B. Jüttner and I. Kleberg, "The retrograde motion of arc cathode spots in vacuum," *J. Phys. D. Appl. Phys.*, vol. 33, no. 16, pp. 2025–2036, 2000, doi: 10.1088/0022-3727/33/16/315.
- [16] L. Li *et al.*, "Control of cathodic arc spot motion under external magnetic field," *Vacuum*, vol. 91, pp. 20–23, 2013, doi: 10.1016/j.vacuum.2012.10.008.

- [17] L. Wang, J. Deng, X. Zhou, S. Jia, Z. Qian, and Z. Shi, "Experimental investigation of cathode spots and plasma jets behavior subjected to two kinds of axial magnetic field electrodes," *Phys. Plasmas*, vol. 23, no. 4, pp. 043514–8, 2016, doi: 10.1063/1.4947561.
- [18] X. Song, Q. Wang, Z. Lin, P. Zhang, and S. Wang, "Control of vacuum arc source cathode spots contraction motion by changing electromagnetic field," *Plasma Sci. Technol.*, vol. 20, no. 2, p. 25402, 2018, doi: 10.1088/2058-6272/aa8a30.
- [19] P. J. Walke, R. New, and C. M. Care, "Behavior of a steered cathodic arc as a function of steering magnetic field," *Surf. Coatings Technol.*, vol. 59, no. 1–3, pp. 126–128, 1993, doi: [https://doi.org/10.1016/0257-8972\(93\)90068-Y](https://doi.org/10.1016/0257-8972(93)90068-Y).
- [20] S. K. Sethuraman and M. R. Barrault, "Study of the motion of vacuum arcs in high magnetic field," *J. Nucl. Mater.*, vol. 93–94, no. 6, pp. 791–798, 1980, doi: 10.1016/0022-3115(80)90209-3.
- [21] A. E. Robson, "The motion of a low-pressure arc in a strong magnetic field," *J. Phys. D: Appl. Phys.*, vol. 11, no. 13, pp. 1917–1923, 1978, doi: <https://doi.org/10.1088/0022-3727/11/13/014>.
- [22] I. I. Beilis, B. Sagi, V. Zhitomirsky, and R. L. Boxman, "Cathode spot motion in a vacuum arc with a long roof-shaped cathode under magnetic field," *J. Appl. Phys.*, vol. 117, no. 23, pp. 233303–8, 2015, doi: 10.1063/1.4922862.
- [23] M. G. Drouet, "Physics of the Retrograde Motion of the Electric Arc," *IEEE Trans. Plasma Sci.*, vol. PS-13, no. 5, pp. 235–241, 1985, doi: 10.1109/TPS.1985.4316412.
- [24] M. S. Benilov, H. T. C. Kaufmann, W. Hartmann, and L. G. Benilova, "Revisiting Theoretical Description of the Retrograde Motion of Cathode Spots of Vacuum Arcs," *IEEE Trans. Plasma Sci.*, vol. 47, no. 8, pp. 3434–3441, 2019, doi: 10.1109/TPS.2019.2904866.
- [25] V. Nemchinsky, "Model of the Retrograde Motion of a Vacuum Arc: Comparison to Experiments," *IEEE Trans. Plasma Sci.*, vol. 48, no. 4, pp. 1154–1161, 2020, doi: 10.1109/TPS.2020.2978837.
- [26] B. Jüttner, "Cathode spots of electric arcs," *J. Phys. D: Appl. Phys.*, vol. 34, no. 17, pp. R103–R123, 2001, doi: 10.1088/0022-3727/34/17/202.
- [27] Z. Zhou, A. Kyritsakis, Z. Wang, Y. Li, Y. Geng, and F. Djurabekova, "Direct observation of vacuum arc evolution with nanosecond resolution," *Sci. Rep.*, vol. 9, no. 1, pp. 1–12, 2019, doi: 10.1038/s41598-019-44191-6.
- [28] A. Anders, S. Anders, B. Jüttner, W. Büttcher, H. Lück, and G. Schröder, "Pulsed Dye Laser Diagnostics of Vacuum Arc Cathode Spots," *IEEE Trans. Plasma Sci.*, vol. 20, no. 4, pp. 466–472, 1992, doi: 10.1109/27.256775.
- [29] A. Anders, S. Anders, B. Jüttner, and H. Lück, "High-resolution imaging of vacuum arc cathode spots," *IEEE Trans. Plasma Sci.*, vol. 24, no. 1, pp. 69–70, 1996, doi: 10.1109/27.491695.
- [30] A. Batrakov, N. Vogel, S. Popov, D. Proskurovsky, D. Kudimov, and D. Nikitine, "Interferograms of a cathode spot plasma obtained with a picosecond laser," *IEEE Trans. Plasma Sci.*, vol. 30, no. 1, pp. 106–107, 2002, doi: 10.1109/TPS.2002.1003946.
- [31] B. Jüttner, "Erosion Craters and Arc Cathode Spots in Vacuum," *Beiträge Plasmaphys.*, vol. 19, no. 1, pp. 25–48, 1979, doi: <https://doi.org/10.1002/ctpp.19790190104>.
- [32] S. Anders and B. Jüttner, "Influence of Residual Gases on Cathode Spot Behavior," *IEEE Trans.*

- Plasma Sci.*, vol. 19, no. 5, pp. 705–712, 1991, doi: 10.1109/27.108402.
- [33] J. Achtert *et al.*, “Influence of Surface Contaminations on Cathode Processes of Vacuum Discharges,” *Beiträge Plasmaphys.*, vol. 17, no. 6, pp. 419–431, 1977, doi: 10.1002/ctpp.19770170606.
 - [34] M. Golizadeh, F. M. Martin, S. Kolozsvári, A. Anders, and R. Franz, “Cathode spot behavior in nitrogen and oxygen gaseous atmospheres and concomitant cathode surface modifications,” *Surf. Coatings Technol.*, vol. 421, no. 15, p. 127441, 2021, doi: 10.1016/j.surfcoat.2021.127441.
 - [35] M. Golizadeh, A. Anders, F. Mendez Martin, S. Kolozsvári, and R. Franz, “Insights into surface modification and erosion of multi-element arc cathodes using a novel multilayer cathode design,” *J. Appl. Phys.*, vol. 127, no. 11, pp. 113301–10, 2020, doi: 10.1063/1.5141406.
 - [36] B. Jüttner, “Nanosecond Displacement Times of Arc Cathode Spots in Vacuum,” *Plasma Phys. Control. Fusion*, vol. 26, no. 1 A, pp. 249–258, 1984, doi: 10.1088/0741-3335/26/1A/323.
 - [37] S. A. Barengolts, G. A. Mesyats, and D. L. Shmelev, “Structure and time behavior of vacuum arc cathode spots,” *IEEE Trans. Plasma Sci.*, vol. 31, no. 5 I, pp. 809–816, 2003, doi: 10.1109/TPS.2003.818449.
 - [38] P. Siemroth, B. Schultrich, and T. Schülke, “Fundamental processes in vacuum arc deposition,” *Surf. Coatings Technol.*, vol. 74–75, no. PART 1, pp. 92–96, 1995, doi: 10.1016/0257-8972(95)08346-4.
 - [39] A. Anders, “The fractal nature of vacuum arc cathode spots,” *IEEE Trans. Plasma Sci.*, vol. 33, no. 5 I, pp. 1456–1464, 2005, doi: 10.1109/TPS.2005.856488.
 - [40] P. Meakin, H. E. Stanley, and A. Thomas, “Scaling properties for the surfaces of fractal and nonfractal objects: An infinite hierarchy of critical exponents,” *Phys. Rev. A*, vol. 34, no. 4, pp. 3325–3340, 1986, doi: 10.1103/physreva.34.3325.
 - [41] A. Anders, “Physics of arcing , and implications to sputter deposition,” *Surf. Coatings Technol.*, vol. 502, no. 1–2, pp. 22–28, 2006, doi: 10.1016/j.tsf.2005.07.228.
 - [42] A. Anders, “Atomic scale heating in cathodic arc plasma deposition,” *Appl. Phys. Lett.*, vol. 80, no. 6, pp. 1100–1102, 2002, doi: 10.1063/1.1448390.
 - [43] J. M. Andersson, J. Vetter, J. Müller, and J. Sjöln, “Structural effects of energy input during growth of $Ti_{1-x}Al_xN$ ($0.55 \leq x \leq 0.66$) coatings by cathodic arc evaporation,” *Surf. Coatings Technol.*, vol. 240, no. 15, pp. 211–220, 2014, doi: 10.1016/j.surfcoat.2013.12.018.
 - [44] C. Wüstefeld, D. Rafaja, V. Klemm, C. Michotte, and M. Kathrein, “Effect of the aluminium content and the bias voltage on the microstructure formation in $Ti_{1-x}Al_xN$ protective coatings grown by cathodic arc evaporation,” *Surf. Coatings Technol.*, vol. 205, no. 5, pp. 1345–1349, 2010, doi: 10.1016/j.surfcoat.2010.07.057.
 - [45] G. Taghavi, P. Azar, and M. Ürgen, “Effect of high-voltage pulse bias on the stress and morphology of CA-PVD TiN coatings,” *Surf. Eng.*, vol. 36, no. 1, pp. 13–21, 2018, doi: 10.1080/02670844.2018.1512731.
 - [46] J. Musil, “Hard and superhard nanocomposite coatings,” *Surf. Coatings Technol.*, vol. 125, no. 1–3, pp. 322–330, 2000, doi: [https://doi.org/10.1016/S0257-8972\(99\)00586-1](https://doi.org/10.1016/S0257-8972(99)00586-1).
 - [47] A. Anders, “A structure zone diagram including plasma-based deposition and ion etching,” *Thin Solid Films*, vol. 518, no. 15, pp. 4087–4090, 2010, doi: 10.1016/j.tsf.2009.10.145.

- [48] J. M. Schneider, A. Anders, I. G. Brown, B. Hjörvarsson, L. Hultman, and I. G. Brown, "Temporal development of the plasma composition of a pulsed aluminum plasma stream in the presence of oxygen," *Appl. Phys. Lett.*, vol. 75, no. 5, pp. 612–614, 1999, doi: 10.1063/1.124457.
- [49] J. Rosén, A. Anders, L. Hultman, and J. M. Schneider, "Temporal development of the composition of Zr and Cr cathodic arc plasma streams in a N₂ environment," *J. Appl. Phys.*, vol. 94, no. 3, pp. 1414–1419, 2003, doi: 10.1063/1.1591079.
- [50] R. L. Boxman, *Handbook of Vacuum Arc Science and Technology*. New Jersey: Noyes, 1995.
- [51] A. Anders, S. Anders, B. Jüttner, H. Pursch, W. Böttcher, and H. Lück, "Vacuum arc cathode spot parameters from high-resolution luminosity measurements," *J. Appl. Phys.*, vol. 71, no. 10, pp. 4763–4770, 1992, doi: 10.1063/1.350668.
- [52] A. Anders, S. Anders, A. Forster, and I. G. Brown, "Pressure ionization: Its role in metal vapour vacuum arc plasmas and ion sources," *Plasma Sources Sci. Technol.*, vol. 1, no. 4, pp. 263–270, 1992, doi: 10.1088/0963-0252/1/4/006.
- [53] K. Oh, D. Kalanov, and A. Anders, "High-resolution observation of cathode spots in a magnetically steered vacuum arc plasma source," *Plasma Sources Sci. Technol.*, vol. 30, no. 9, p. 095005, 2021, doi: 10.1088/1361-6595/ac1ee1.
- [54] K. Oh, D. Kalanov, P. Birtel, and A. Anders, "High-resolution observation of cathodic arc spots in a magnetically steered arc plasma source in low pressure argon , nitrogen , and oxygen atmospheres," *J. Appl. Phys.*, vol. 130, no. 18, p. 183304, 2021, doi: 10.1063/5.0072021.
- [55] D. A. Frank-Kamenetskii, *Plasma the fourth state of matter*. New York: Springer, 1972.
- [56] F. F. Chen, *Introduction to Plasma Physics and Controlled Fusion*, Third Edit. New York: Springer, 2016.
- [57] P. Chatterton, *High voltage vacuum insulation*. London: ACADEMIC PREEE, 1995.
- [58] I. G. Kesaev, *Cathode processes in the mercury arc*. NEW YORK: CONSULTANTS BUREAU, 1964.
- [59] B. Jüttner, "The dynamics of arc cathode spots in vacuum: New measurements," *J. Phys. D. Appl. Phys.*, vol. 30, no. 2, pp. 221–229, 1997, doi: 10.1088/0022-3727/30/2/009.
- [60] B. Jüttner, "Nanosecond displacement times of arc cathode spots in vacuum," *IEEE Trans. Plasma Sci.*, vol. 27, no. 4, pp. 836–844, 1999, doi: 10.1109/27.782247.
- [61] G. Y. Yushkov and A. Anders, "Physical limits for high ion charge states in pulsed discharges in vacuum," *J. Appl. Phys.*, vol. 105, no. 4, pp. 1–5, 2009, doi: 10.1063/1.3079501.
- [62] S. Zöhrer and A. Anders, "Time-resolved ion energy and charge state distributions in pulsed cathodic arc plasmas of Nb – Al cathodes in high vacuum," *Plasma Sources Sci. Technol.*, vol. 27, no. 5, p. 055007, 2018, doi: <https://doi.org/10.1088/1361-6595/aabdc7>.
- [63] G. Y. Yushkov and A. Anders, "Extractable, elevated ion charge states in the transition regime from vacuum sparks to high current vacuum arcs," *Appl. Phys. Lett.*, vol. 92, no. 4, pp. 1–3, 2008, doi: 10.1063/1.2839616.
- [64] E. M. Oks, G. Y. Yushkov, and A. Anders, "Temporal development of ion beam mean charge state in pulsed vacuum arc ion sources," *Rev. Sci. Instrum.*, vol. 79, no. 2, p. 02B301, 2008, doi: 10.1063/1.2801094.

- [65] S. Hohenbild, C. Gr., G. Y. Yushkov, E. M. Oks, and A. Anders, "A study of vacuum arc ion velocities using a linear set of probes," *J. Phys. D Appl. Phys.*, vol. 41, no. 20, p. 205210, 2008, doi: 10.1088/0022-3727/41/20/205210.
- [66] J. Kutzner and H. C. Miller, "Integrated ion flux emitted from the cathode spot region of a diffuse vacuum arc," *J. Phys. D Appl. Phys.*, vol. 25, no. 4, pp. 686–693, 1992, doi: <https://doi.org/10.1088/0022-3727/25/4/015>.
- [67] G. W. McClure, "Plasma expansion as a cause of metal displacement in vacuum-arc cathode spots," *J. Appl. Phys.*, vol. 45, no. 5, pp. 2078–2084, 1974, doi: 10.1063/1.1663547.
- [68] J. Rosén and A. Anders, "Time and material dependence of the voltage noise generated by cathodic vacuum arcs," *J. Phys. D. Appl. Phys.*, vol. 38, no. 23, pp. 4184–4190, 2005, doi: 10.1088/0022-3727/38/23/007.
- [69] A. Anders, K. Fukuda, and G. Y. Yushkov, "Ion charge state fluctuations in vacuum arcs," *J. Phys. D. Appl. Phys.*, vol. 38, no. 7, pp. 1021–1028, 2005, doi: 10.1088/0022-3727/38/7/009.
- [70] A. Anders, "Plasma fluctuations, local partial Saha equilibrium, and the broadening of vacuum-arc ion charge state distributions," *IEEE Trans. Plasma Sci.*, vol. 27, no. 4, pp. 1060–1067, 1999, doi: 10.1109/27.782282.
- [71] A. Anders and E. Oks, "Material-dependent high-frequency current fluctuations of cathodic vacuum arcs: Evidence for the ecton cutoff of the fractal model," *J. Appl. Phys.*, vol. 99, no. 10, pp. 103301–5, 2006, doi: 10.1063/1.2196244.
- [72] G. A. Mesyats, *Explosive Electron Emission*. Ekaterinburg: URO Press, 1998.
- [73] G. A. Mesyats, "Mechanism of anomalous ion generation in vacuum arcs," *Physics-Uspekh*, vol. 45, no. 10, pp. 1001–1018, 2002, doi: 10.1070/PU2002v045n10ABEH001247.
- [74] G. A. Mesyats, *Cathode phenomena in a vacuum discharge : the breakdown, the spark, and the arc*. Moscow: Nauka, 2000.
- [75] S. P. Bugaev, E. A. Litvinov, G. A. Mesyats, and D. I. Proskurovskii, "Explosive emission of electrons," *Sov. Phys. Usp.*, vol. 115, no. 1, p. 51, 1975, doi: <https://doi.org/10.1070/PU1975v018n01ABEH004693>.
- [76] E. A. Litvinov, G. A. Mesyats, and D. I. Proskurovskii, "Field emission and explosive electron emission processes in vacuum discharges," *Usp. Fiz. Nauk*, vol. 26, no. 2, p. 138, 1983, doi: <https://doi.org/10.1070/PU1983v026n02ABEH004322>.
- [77] G. A. Mesyats, "Ecton Mechanism of the Vacuum Arc Cathode Spot," *IEEE Trans. Plasma Sci.*, vol. 23, no. 6, pp. 879–883, 1995, doi: 10.1109/27.476469.
- [78] G. A. Mesyats and D. I. Proskurovsky, *Pulsed electrical discharge in vacuum*. Berlin: Springer-Verlag Berlin Heidelberg, 1989.
- [79] G. A. Mesyats, "Ecton or electron avalanche from metal," *Phys. Uspkhi*, vol. 38, no. 6, pp. 567–591, 1995, doi: <https://doi.org/10.1070/PU1995v038n06ABEH000089>.
- [80] A. Anders, "The evolution of ion charge states in cathodic vacuum arc plasmas : a review," *Plasma Sources Sci. Technol.*, vol. 21, no. 3, p. 035014, 2012, doi: 10.1088/0963-0252/21/3/035014.
- [81] C. Wieckert, "The expansion of the cathode spot plasma in vacuum arc discharges," *Phys. Fluids*, vol. 30, no. 6, pp. 1810–1813, 1987, doi: 10.1063/1.866195.

- [82] A. Anders, "Ion charge state distributions of vacuum arc plasmas : The origin of species," *Phys. Rev. E*, vol. 55, no. 1, pp. 969–981, 1997, doi: <https://doi.org/10.1103/PhysRevE.55.969>.
- [83] A. Anders, "A review comparing cathodic arcs and high power impulse magnetron sputtering (HiPIMS)," *Surf. Coatings Technol.*, vol. 257, no. 25, pp. 308–325, 2014, doi: [10.1016/j.surfcoat.2014.08.043](https://doi.org/10.1016/j.surfcoat.2014.08.043).
- [84] V. Nemchinsky, "What Heats the Cathode Spot of a Vacuum Arc ?," *IEEE Trans. Plasma Sci.*, vol. 48, no. 7, pp. 1–6, 2020, doi: [10.1109/TPS.2020.2999418](https://doi.org/10.1109/TPS.2020.2999418).
- [85] W. Neumann, *The Mechanism of the Thermoemitting Arc Cathode*. Berlin: AkademieVerlag, 1987.
- [86] Richardson, O.W, *Emission of Electricity from Hot Bodies*. NewYork: Longmans,Green & Co., 1921.
- [87] S. Dushman, "Electron Emission from Metals as a Function of Temperature," *Phys. Rev.*, vol. 21, no. 6, p. 623, 1923, doi: <https://doi.org/10.1103/PhysRev.21.623>.
- [88] S. Dushman, "Thermionic emission," *Rev. Mod. Phys.*, vol. 2, pp. 381–476, 1930.
- [89] O. W. Richardson, "On the negative radiation from hot plantinum," *Proc. Cambridge Phil. Soc.*, vol. 11, no. 4, pp. 286–295, 1902.
- [90] R. F. Khairutdinov, Y. A. Berlin, and K. I. Zamaraev, "Effect of an external electric field on electron-transfer tunnel reactions," *Bull. Acad. Sci. USSR, Div. Chem. Sci.*, vol. 26, pp. 1832–1835, 1977, doi: [10.1007/BF00924370](https://doi.org/10.1007/BF00924370).
- [91] R. H. Good Jr and E. W. Müller, *Field Emission. In: Electron-Emission Gas Discharges I/ Elektronen-Emission Gasentladungen I. Encyclopedia of Physics*, vol. 4/21. Springer, Berlin, Heidelberg, 1956.
- [92] H. C. Miller, "Value of Fowler-Nordheim field emission functions $v(y)$, $t(y)$ and $s(y)$," *J. Franklin Inst.*, vol. 282, no. 6, pp. 382–388, 1966, doi: [https://doi.org/10.1016/0016-0032\(66\)90043-3](https://doi.org/10.1016/0016-0032(66)90043-3).
- [93] E. Hantzsche, "The Thermo-Field Emission of Electrons in Arc Discharges," *Beiträge aus der Plasmaphys.*, vol. 22, no. 4, pp. 325–346, 1982, doi: <https://doi.org/10.1002/ctpp.19820220403>.
- [94] R. H. Fowler and L. Nordheim, "Electron Emission in Intense Electric Fields," *Proc. R. Soc. Lond. A*, vol. 119, no. 781, pp. 173–181, 1928, doi: [10.1098/rspa.1928.0091](https://doi.org/10.1098/rspa.1928.0091).
- [95] E. L. Murphy and R. H. Good, "Thermionic Emission, Field Emission, and the Transition Region," *Phys. Rev.*, vol. 102, no. 6, pp. 1465–1473, 1956, doi: <https://doi.org/10.1103/PhysRev.102.1464>.
- [96] W. W. Dolan and W. P. Dyke, "Temperature and Field Emission of Electrons from Metals," *Phys. Rev.*, vol. 95, no. 2, pp. 327–332, 1954, doi: <https://doi.org/10.1103/PhysRev.95.327>.
- [97] S. Coulombe and J. Meunier, "Thermo-field emission : a comparative study," *J. Phys. D. Appl. Phys.*, vol. 30, no. 5, pp. 776–780, 1997, doi: <https://doi.org/10.1088/0022-3727/30/5/009>.
- [98] S. G. Christov, "General Theory of Electron Emission from Metals," *Phys.stat.sol.*, vol. 17, no. 1, pp. 11–26, 1966, doi: <https://doi.org/10.1002/pssb.19660170103>.
- [99] S. G. Christov and C. M. Vodenicharov, "On the experimental proof of the general theory of electron emission from metals," *Solid. State. Electron.*, vol. 11, no. 8, pp. 757–766, 1968, doi: [https://doi.org/10.1016/0038-0121\(68\)90001-1](https://doi.org/10.1016/0038-0121(68)90001-1).

[https://doi.org/10.1016/0038-1101\(68\)90056-7](https://doi.org/10.1016/0038-1101(68)90056-7).

- [100] B. Jüttner, *Cathodic processes of the metal vapor arc*. Kiev: Paton Electric Welding Institute, 2003.
- [101] G. Ecker and K. G. Müller, "Electron emission from the arc cathode under the influence of the individual field component," *J. Appl. Phys.*, vol. 30, no. 9, p. 1466, 1959, doi: 10.1063/1.1735372.
- [102] V. F. Puchkarev and B. Bochkarev, "Cathode spot initiation under plasma," *J. Phys. D: Appl. Phys.*, vol. 27, no. 6, pp. 1214–1219, 1994, doi: <https://doi.org/10.1088/0022-3727/27/6/019>.
- [103] I. V. Uimanov, "A two-dimensional nonstationary model of the initiation of an explosive center beneath the plasma of a vacuum arc cathode spot," *IEEE Trans. Plasma Sci.*, vol. 31, no. 5, pp. 822–826, 2003, doi: 10.1109/TPS.2003.818435.
- [104] A. Anders, S. Anders, and M. A. Gundersen, "Electron emission from pseudospark cathodes Electron emission from pseudospark," *J. Appl. Phys.*, vol. 76, no. 3, p. 1994, 1994, doi: 10.1063/1.357724.
- [105] C. D. Child, "Discharge From Hot CaO," *Phys. Rev. (Series I)*, vol. 32, no. 5, pp. 492–511, 1911, doi: <https://doi.org/10.1103/PhysRevSeriesI.32.492>.
- [106] I. Langmuir and K. B. Blodgett, "Currents limited by space charge between coaxial cylinders," *Phys. Rev.*, vol. 22, no. 4, pp. 347–356, 1923, doi: <https://doi.org/10.1103/PhysRev.22.347>.
- [107] I. Langmuir, "The effect of space charge and initial velocities on the potential distribution and thermionic current between parallel plane electrodes," *Phys. Rev.*, vol. 21, no. 4, pp. 419–435, 1923, doi: <https://doi.org/10.1103/PhysRev.21.419>.
- [108] K.-U. Riemann, "Theory of the Cathode Sheath in a vacuum arc," *IEEE Trans. Plasma Sci.*, vol. 17, no. 5, pp. 641–643, 1989, doi: 10.1109/27.41172.
- [109] E. Hantzsche, "Arc Spot Ignition Caused by Sheath Instability," *IEEE Trans. Plasma Sci.*, vol. 25, no. 4, pp. 527–532, 1997, doi: 10.1109/27.640660.
- [110] A. T. Forrester, *Large Ion Beams: Fundamentals of Generation and Propagation*. NEW YORK: John Wiley & Sons, 1988.
- [111] G. A. Mesyats, "Ecton mechanism of the cathode spot phenomena in a vacuum Arc," *IEEE Trans. Plasma Sci.*, vol. 41, no. 4, pp. 676–694, 2013, doi: 10.1109/TPS.2013.2247064.
- [112] G. A. Lyubimov and V. I. Rakhovskii, "The cathode spot of a vacuum arc," *Sov. Phys. - Uspekhi*, vol. 21, no. 8, pp. 693–718, 1978, doi: 10.1070/PU1978v021n08ABEH005674.
- [113] J. E. Daalder, "Energy dissipation in the cathode of a vacuum arc," *J. Phys. D: Appl. Phys.*, vol. 10, no. 16, p. 2225, 1977, doi: <https://doi.org/10.1088/0022-3727/10/16/013>.
- [114] G. A. Mesyats, "The role of fast processes in vacuum breakdown," *Proc. 10 Intern. Conf. Phenom. Ioniz. Gases*, pp. 333–63, 1971.
- [115] Y. A. Kotov, O. M. Samatov, V. S. Sedoi, L. I. Chemezova, and A. A. Chertov, "Heating of conductors by high-density current," *Proc. Int. Conf. Megagauss F. Pulsed Power Syst.*, vol. 22, no. 2, pp. 497–502, 1990.
- [116] G. A. Mesyats, "Ectons and their Role in Electrical Discharges in Vacuum and Gases," *J. Phys IV Fr.*, vol. 7, no. C4, pp. C4-93, 1997, doi: 10.1051/jp4:1997407.

- [117] J. Stark, "Induktionserscheinungen am Quecksilberlichtbogen im Magnetfeld," *Zeitschrift für Phys.*, vol. 4, pp. 440–443, 1903.
- [118] R. N. Szente, R. J. Munz, and M. G. Drouet, "The influence of the cathode surface on the movement of magnetically driven electric arcs," *J. Phys. D. Appl. Phys.*, vol. 23, no. 9, pp. 1193–1200, 1990, doi: 10.1088/0022-3727/23/9/009.
- [119] C. Wang, J. Li, Z. Zhang, L. Ye, W. Xia, and W. Xia, "An Experimental Investigation of Cathode Spot Motion in a Magnetically Rotating Arc Plasma Generator at Atmospheric Pressure," *Plasma Chem. Plasma Process.*, vol. 39, no. 1, pp. 259–276, 2019, doi: 10.1007/s11090-018-9937-8.
- [120] E. Weintraub, "Investigation of the arc in metallic vapours in an exhausted space," *Phil. Mag.*, vol. 7, no. 38, pp. 95–124, 1904, doi: <https://doi.org/10.1080/14786440409463094>.
- [121] L. J. Buttolph, "The cooper hewitt mercury vapor lamp," *Gen. Electr. Rev.*, vol. 23, pp. 741–751, 1920.
- [122] A. Greenwood, *Vacuum Switching of High Current and High Voltage at Power Frequencies*, In Handboo. Park Ridge, New Jersey: Noyes Publications, 1995.
- [123] P. G. Slade, *Electrical Contacts: Principles and Applications*. New York: Marcel Dekker Inc., 1999.
- [124] L. B. Raymond, "Triggering Mechanisms in Triggered Vacuum Gaps," *IEEE Trans. Electron Devices*, vol. 24, no. 2, pp. 122–128, 1977, doi: 10.1109/T-ED.1977.18690.
- [125] A. Gilmour and D. L. Lockwood, "Pulsed Metallic-Plasma Generators," *Proc. IEEE*, vol. 60, no. 8, pp. 977–991, 1972, doi: 10.1109/PROC.1972.8821.
- [126] S. Kamakshaiah and R. S. N. Rau, "Delay characteristics of a simple triggered vacuum gap," *J. Phys. D Appl. Phys.*, vol. 8, no. 12, pp. 1426–1429, 1975, doi: <https://doi.org/10.1088/0022-3727/8/12/014>.
- [127] G. C. Watt and P. J. Evans, "A trigger power supply for vacuum arc ion sources," *IEEE Trans. Plasma Sci.*, vol. 21, no. 5, pp. 547–551, 1993, doi: 10.1109/27.249641.
- [128] A. Anders, I. G. Brown, R. A. Macgill, and M. R. Dickinson, "'Triggerless' triggering of vacuum arcs," *J. Phys. D Appl. Phys.*, vol. 31, no. 5, pp. 584–587, 1998, doi: <https://doi.org/10.1088/0022-3727/31/5/015>.
- [129] A. Anders, J. Schein, and N. Qi, "Pulsed vacuum-arc ion source operated with a 'triggerless' arc initiation method," *Rev. Sci. Instrum.*, vol. 71, no. 2, pp. 827–829, 2000, doi: 10.1063/1.1150305.
- [130] M. Godbole and A. M. Jain, "Double Break Vacuum Circuit Breaker," in *10th International Conference on Intelligent Systems and Control*, 2016, doi: 10.1109/ISCO.2016.7727112.
- [131] A. Anders, B. Yotsombat, and R. Binder, "Correlation between cathode properties, burning voltage, and plasma parameters of vacuum arcs," *J. Appl. Phys.*, vol. 89, no. 12, pp. 7764–7771, 2001, doi: 10.1063/1.1371276.
- [132] A. Anders, *Cohesive energy rule for vacuum arcs*. In: Oks, E., Brown, I. (eds) *Emerging Applications of Vacuum-Arc-Produced Plasma, Ion and Electron Beams.*, Nato Scien. Springer, Dordrecht, 2002.
- [133] G. R. Mitchell, "Erratum: High-current vacuum arcs. Part 1: An experimental study," *Proc. Inst.*

- Electr. Eng.*, vol. 118, no. 5, p. 736, 1971, doi: 10.1049/piee.1971.0136.
- [134] A. Anders and G. Y. Yushkov, "Ion flux from vacuum arc cathode spots in the absence and presence of a magnetic field," *J. Appl. Phys.*, vol. 91, no. 8, pp. 4824–4832, 2002, doi: 10.1063/1.1459619.
 - [135] E. M. Oks *et al.*, "Elevated ion charge states in vacuum arc plasmas in a magnetic field," *Appl. Phys. Lett.*, vol. 67, no. 1995, p. 200, 1995, doi: 10.1063/1.114666.
 - [136] F. J. Paoloni and I. G. Brown, "Some observations of the effect of magnetic field and arc current on the vacuum arc ion charge state distribution," *Rev. Sci. Instrum.*, vol. 66, no. 7, pp. 3855–3858, 1995, doi: 10.1063/1.1145448.
 - [137] E. M. Oks, A. Anders, I. G. Brown, M. R. Dickinson, and R. A. MacGill, "Ion charge state distributions in high current vacuum arc plasmas in a magnetic field," *IEEE Trans. Plasma Sci.*, vol. 24, no. 3, pp. 1174–1183, 1996, doi: 10.1109/27.533127.
 - [138] A. Anders, G. Yushkov, E. Oks, A. Nikolaev, and I. Brown, "Ion charge state distributions of pulsed vacuum arc plasmas in strong magnetic fields," *Rev. Sci. Instrum.*, vol. 69, no. 3, pp. 1332–1335, 1998, doi: 10.1063/1.1148801.
 - [139] V. A. Ivanov and H. Pursch, "Time-Resolved Measurements of the Parameters of Arc Cathode Plasmas in Vacuum," *IEEE Trans. Plasma Sci.*, vol. PS-13, no. 5, pp. 334–336, 1985, doi: 10.1109/TPS.1985.4316432.
 - [140] M. Biberman, L. V. S. Vorobev, and I. T. Iakubov, *Kinetics of the non-equilibrium and low temperature plasma*. Moscow: Nauka, 1982.
 - [141] A. S. Bugaev, E. M. Oks, G. Y. Yushkov, A. Anders, and I. G. Brown, "Enhanced ion charge states in vacuum arc plasmas using a 'current spike' method," *Rev. Sci. Instrum.*, vol. 71, no. 2, pp. 701–703, 2000, doi: 10.1063/1.1150266.
 - [142] A. S. Bugaev, "Influence of a current jump on vacuum arc parameters," *IEEE Trans. Plasma Sci.*, vol. 27, no. 4, pp. 882–887, 1999, doi: 10.1109/27.782254.
 - [143] K. Tsuruta, O. Tan, and G. I. Watanabe, "Velocity of Copper Ions Generated from an Impulse Vacuum Arc," *IEEE Trans. Plasma Sci.*, vol. 25, no. 4, p. 603, 1997, doi: 10.3131/jvsj.38.207.
 - [144] G. Yushkov, "Measurement of directed ion velocity in vacuum arc plasmas by arc current perturbation methods," *Int. Symp. Discharges Electr. Insul. Vacuum, ISDEIV*, vol. 1, pp. 260–263, 2000.
 - [145] J. Rosén, A. Anders, S. Mráz, and J. M. Schneider, "Charge-state-resolved ion energy distributions of aluminum vacuum arcs in the absence and presence of a magnetic field," *J. Appl. Phys.*, vol. 97, no. 10, pp. 103306–6, 2005, doi: 10.1063/1.1906291.
 - [146] M. M. M. Bilek, P. J. Martin, and D. R. McKenzie, "Influence of gas pressure and cathode composition on ion energy distributions in filtered cathodic vacuum arcs," *J. Appl. Phys.*, vol. 83, no. 6, pp. 2965–2970, 1998, doi: 10.1063/1.367052.
 - [147] M. Chhowalla, "Ion energy and charge state distributions in zirconium nitride arc plasma," *Appl. Phys. Lett.*, vol. 83, no. 8, pp. 1542–1544, 2003, doi: 10.1063/1.1606107.
 - [148] W. D. Davis and H. C. Miller, "Analysis of the electrode products emitted by dc arcs in a vacuum ambient," *J. Appl. Phys.*, vol. 40, no. 5, pp. 2212–2221, 1969, doi: 10.1063/1.1657960.

- [149] H. C. Miller, "Constraints imposed upon theories of the vacuum arc cathode region by specific ion energy measurements," *J. Appl. Phys.*, vol. 52, no. 7, pp. 4523–4530, 1981, doi: 10.1063/1.329380.
- [150] M. Galonska, R. Hollinger, and P. Spädtke, "Charge sensitive evaluated ion and electron energy distributions of a vacuum arc plasma," *Rev. Sci. Instrum.*, vol. 75, no. 5 PART II, pp. 1592–1594, 2004, doi: 10.1063/1.1691518.
- [151] J. Rośn, J. M. Schneider, and A. Anders, "Charge state dependence of cathodic vacuum arc ion energy and velocity distributions," *Appl. Phys. Lett.*, vol. 89, no. 14, pp. 10–13, 2006, doi: 10.1063/1.2361197.
- [152] G. Y. Yushkov, A. Anders, E. M. Oks, and I. G. Brown, "Ion velocities in vacuum arc plasmas," *J. Appl. Phys.*, vol. 88, no. 10, pp. 5618–5622, 2000, doi: 10.1063/1.1321789.
- [153] A. A. Plyutto, V. N. Ryzhkov, and A. T. Kapin, "High Speed Plasma Streams in Vacuum Arcs," *Sov. Phys. JETP*, vol. 20, no. 2, pp. 328–337, 1965.
- [154] M. Galonska, R. Hollinger, I. A. Krinberg, and P. Spaedtke, "Influence of an axial magnetic field on the electron temperature in a vacuum arc plasma," *IEEE Trans. Plasma Sci.*, vol. 33, no. 5 I, pp. 1542–1547, 2005, doi: 10.1109/TPS.2005.856504.
- [155] K. Tanaka, L. Han, X. Zhou, and A. Anders, "Adding high time resolution to charge-state-specific ion energy measurements for pulsed copper vacuum arc plasmas," *Plasma Sources Sci. Technol.*, vol. 24, no. 4, p. 045010, 2015, doi: 10.1088/0963-0252/24/4/045010.
- [156] A. Anders and G. Y. Yushkov, "Puzzling differences in bismuth and lead plasmas: Evidence for the significant role of neutrals in cathodic vacuum arcs," *Appl. Phys. Lett.*, vol. 91, no. 9, pp. 89–92, 2007, doi: 10.1063/1.2776858.
- [157] A. Anders, "Time-dependence of ion charge state distributions of vacuum arcs: An interpretation involving atoms and charge exchange collisions," *IEEE Trans. Plasma Sci.*, vol. 33, no. 1 II, pp. 205–209, 2005, doi: 10.1109/TPS.2004.841804.
- [158] A. Anders, S. Anders, and B. Jüttner, "Time Dependence of Vacuum Arc Parameters," *IEEE Trans. Plasma Sci.*, vol. 21, no. 3, pp. 305–311, 1993, doi: 10.1109/27.277556.
- [159] R. Franz, P. Polcik, and A. Anders, "Ion charge state distributions of Al and Cr in cathodic arc plasmas from composite cathodes in vacuum, argon, nitrogen, and oxygen," *IEEE Trans. Plasma Sci.*, vol. 41, no. 8, pp. 1929–1937, 2013, doi: 10.1109/TPS.2013.2254135.
- [160] R. Franz, P. Polcik, and A. Anders, "Element- and charge-state-resolved ion energies in the cathodic arc plasma from composite AlCr cathodes in argon, nitrogen and oxygen atmospheres," *Surf. Coatings Technol.*, vol. 272, pp. 309–321, 2015, doi: 10.1016/j.surfcoat.2015.03.047.
- [161] A. I. Bushik, B. Jüttner, and H. Pursch, "On the Nature and the Motion of Arc Cathode Spots in UHV," *Beiträge aus der Plasmaphys.*, vol. 19, no. 3, pp. 177–188, 1979, doi: 10.1002/ctpp.19790190305.
- [162] A. E. Guile and B. Juttner, "Basic Erosion Processes of Oxidized and Clean Metal Cathodes by Electric Arcs," *IEEE Trans. Plasma Sci.*, vol. 8, no. 3, pp. 259–269, 1980, doi: 10.1109/TPS.1980.4317315.
- [163] J. Achtert *et al.*, "Influence of Surface Contaminations on Cathode Processes of Vacuum Discharges," *Beiträge aus der Plasmaphys.*, vol. 17, no. 6, pp. 419–431, 1977, doi:

10.1002/ctpp.19770170606.

- [164] A. Eberhagen, "Die Änderung der Austrittsarbeit von Metallen durch eine Gasadsorption," *Fortschritte der Phys.*, vol. 8, no. 5–6, pp. 245–294, 1960, doi: 10.1002/prop.19600080502.
- [165] Z. L. Tang, K. Yang, H. X. Liu, Y. C. Zhang, H. Li, and X. D. Zhu, "Dynamics of cathode spots in low-pressure arc plasma removing oxide layer on steel surfaces," *Phys. Plasmas*, vol. 23, no. 3, p. 033501, 2016, doi: 10.1063/1.4942870.
- [166] M. Laux *et al.*, "Arcing at B4C-covered limiters exposed to a SOL-plasma," *J. Nucl. Mater.*, vol. 313–316, pp. 62–66, 2003, doi: [https://doi.org/10.1016/S0022-3115\(02\)01333-8](https://doi.org/10.1016/S0022-3115(02)01333-8).
- [167] M. Kandah and J. Meunier, "Study of microdroplet generation from vacuum arcs on graphite cathodes Study of microdroplet generation from vacuum arcs on graphite cathodes," *J. Vac. Sci. Technol. A*, vol. 13, no. 5, p. 2444, 1995, doi: 10.1116/1.579486.
- [168] M. Kandah and J. Meunier, "Vacuum arc cathode spot movement on various kinds of graphite cathodes," *Plasma Sources Sci. Technol.*, vol. 5, no. 3, pp. 349–355, 1996, doi: <https://doi.org/10.1088/0963-0252/5/3/001>.
- [169] I. I. Beilis, "Application of Vacuum Arc Cathode Spot Model to Graphite Cathode," vol. 27, no. 4, pp. 821–826, 1999, doi: 10.1109/27.782245.
- [170] I. I. Beilis, "Vacuum arc cathode spot grouping and motion in magnetic fields," *IEEE Trans. Plasma Sci.*, vol. 30, no. 6, pp. 2124–2132, 2002, doi: 10.1109/TPS.2002.807330.
- [171] Schroeder.M, *Fractals Chaos Power Laws: Minutes from an Infinite Paradise*, 8th ed., 8th ed. New York: W.H. Freeman., 2000.
- [172] S. Anders, A. Anders, and B. Jüttner, "Brightness Distribution and Current Density of Vacuum Arc Cathode Spots," *J. Phys. D. Appl. Phys.*, vol. 25, no. 11, pp. 1591–1599, 1992, doi: 10.1088/0022-3727/25/11/005.
- [173] B. Jüttner, H. Pursch, and V. A. Shilov, "The influence of surface roughness and surface temperature on arc spot movement in vacuum," *J. Phys. D. Appl. Phys.*, vol. 17, no. 2, pp. L31–L34, 1984, doi: 10.1088/0022-3727/17/2/002.
- [174] D. J. Griffiths, *Introduction to Electrodynamics*. New Jersey: Prentice-Hall, 1999.
- [175] B. B. Mandelbrot, *The fractal geometry of nature*. San Francisco: W.H. Freeman., 1982.
- [176] J. G. Holden, "Gauging the Fractal Dimension of Response Times from Cognitive Tasks," in *Tutorials in contemporary nonlinear methods for the behavior sciences*, M. A. Riley and V. Orden, Eds. 2005, pp. 267–318.
- [177] A. R. Osborne and A. Pastorello, "Simultaneous occurrence of low-dimensional chaos and colored random noise in nonlinear physical systems," *Phys. Lett. A*, vol. 181, no. 2, pp. 159–171, 1993, doi: [https://doi.org/10.1016/0375-9601\(93\)90914-L](https://doi.org/10.1016/0375-9601(93)90914-L).
- [178] P. Bak, C. Tang, and K. Wiesenfeld, "Self-organized criticality: An explanation of the 1/f noise," *Phys. Rev. Lett.*, vol. 59, no. 4, pp. 381–384, 1987, doi: <https://doi.org/10.1103/PhysRevLett.59.381>.
- [179] T. Schülke and P. Siemroth, "Vacuum arc cathode spots as a self-similarity phenomenon," *IEEE Trans. Plasma Sci.*, vol. 24, no. 1, pp. 63–64, 1996, doi: 10.1109/27.491692.
- [180] A. Anders, E. M. Oks, and G. Y. Yushkov, "Cathodic arcs: Fractal voltage and cohesive energy

- rule," *Appl. Phys. Lett.*, vol. 86, no. 21, pp. 1–3, 2005, doi: 10.1063/1.1937994.
- [181] D. C. Ferguson, P. Perillat, and B. Vayner, "Spectral Characteristics of GEO Satellite Arcing – 300 To 350 MHz," *J. Astronaut. Sci.*, vol. 69, pp. 139–148, 2022, doi: 10.1007/s40295-021-00295-8.
 - [182] A. Anders, "Energetic deposition using filtered cathodic arc plasmas," *Vacuum*, vol. 67, no. 3–4, pp. 673–686, 2002, doi: 10.1016/S0042-207X(02)00260-9.
 - [183] G. K. Wolf, "Modification of chemical properties of materials by ion beam mixing and ion beam assisted deposition," *J. Vac. Sci. Technol. A Vacuum, Surfaces, Film.*, vol. 10, no. 4, pp. 1757–1764, 1992, doi: 10.1116/1.577743.
 - [184] W. D. Sproul, "Ion-assisted deposition in unbalanced-magnetron sputtering systems," *Mater. Sci. Eng. A*, vol. 163, no. 2, pp. 187–192, 1993, doi: 10.1016/0921-5093(93)90787-F.
 - [185] R. Jordan, D. Cole, J. G. Lunney, K. Mackay, and D. Givord, "Pulsed laser ablation of metals," *Appl. Surf. Sci.*, vol. 86, no. 1–4, pp. 24–28, 1995, doi: 10.1016/S0169-4332(97)00770-8.
 - [186] J. S. Colligon, "Energetic condensation: Processes, properties, and products," *J. Vac. Sci. Technol. A Vacuum, Surfaces, Film.*, vol. 13, no. 3, pp. 1649–1657, 1995, doi: 10.1116/1.579746.
 - [187] F. A. Smidt, "Use of ion beam assisted deposition to modify the microstructure and properties of thin films," *Int. Mater. Rev.*, vol. 35, no. 1, pp. 61–128, 1990, doi: 10.1179/095066090790323975.
 - [188] J. A. Thornton, "Influence of Apparatus Geometry and Deposition Conditions on the Structure and Topography of Thick Sputtered Coatings," *J Vac Sci Technol*, vol. 11, no. 4, pp. 666–670, 1974, doi: 10.1116/1.1312732.
 - [189] G. Taghavi, P. Azar, D. Er, and M. Ürgen, "The role of superimposing pulse bias voltage on DC bias on the macroparticle attachment and structure of TiAlN coatings produced with CA-PVD," *Surf. Coat. Technol.*, vol. 350, no. 25, pp. 1050–1057, 2018, doi: 10.1016/j.surfcoat.2018.02.066.
 - [190] J. Salamania *et al.*, "Influence of pulsed-substrate bias duty cycle on the microstructure and defects of cathodic arc-deposited Ti 1-x Al x N coatings," *Surf. Coatings Technol.*, vol. 419, p. 127295, 2021, doi: 10.1016/j.surfcoat.2021.127295.
 - [191] W. Olbrich and G. Kampschulte, "Additional ion bombardment in PVD processes generated by a superimposed pulse bias voltage," *Surf. Coatings Technol.*, vol. 61, no. 1–3, pp. 262–267, 1993, doi: [https://doi.org/10.1016/0257-8972\(93\)90236-H](https://doi.org/10.1016/0257-8972(93)90236-H).
 - [192] E. Lugscheider, O. Knotek, C. Barimani, S. Guerreiro, and H. Zimmermann, "Deposition of arc TiAlN coatings with pulsed bias," vol. 77, pp. 700–705, 1995.
 - [193] W. Olbrich, J. Fessmann, G. Kampschulte, and J. Ebberink, "Improved control of TiN coating properties using cathodic arc evaporation with a pulsed bias," *Surf. Coatings Technol.*, vol. 49, pp. 258–262, 1991.
 - [194] Y. Wei and C. Gong, "Effects of pulsed bias duty ratio on microstructure and mechanical properties of TiN / TiAlN multilayer coatings," *Appl. Surf. Sci.*, vol. 257, pp. 7881–7886, 2011, doi: 10.1016/j.apsusc.2011.04.066.
 - [195] M. Huang, G. Lin, Y. Zhao, C. Sun, L. Wen, and C. Dong, "Macro-particle reduction mechanism in biased arc ion plating of TiN," *Surf. Coatings Technol.*, vol. 176, no. 03, pp. 109–114, 2003,

- doi: 10.1016/S0257-8972(03)00017-3.
- [196] Z. Li, W. Zhu, Y. Zhang, G. Li, and E. Cao, "Effects of superimposed pulse bias on TiN coating in cathodic arc deposition," *Surf. Coatings Technol.*, vol. 131, no. 1–3, pp. 158–161, 2000, doi: [https://doi.org/10.1016/S0257-8972\(00\)00754-4](https://doi.org/10.1016/S0257-8972(00)00754-4).
 - [197] T. A. Carlson, C. W. Nestor, N. Wasserman, and J. D. McDowell, "Calculated ionization potentials for multiply charges ions," *At. Data Nucl. Data Tables*, vol. 2, pp. 63–99, 1970, doi: [https://doi.org/10.1016/S0092-640X\(70\)80005-5](https://doi.org/10.1016/S0092-640X(70)80005-5).
 - [198] D. H. G. Schneider and M. A. Briere, "Investigations of the Interactions of Highest Charge State Ions w i t h Surfaces," *Phys. Scr.*, vol. 53, no. 2, pp. 228–242, 1996, doi: <https://doi.org/10.1088/0031-8949/53/2/013>.
 - [199] A. Arnau *et al.*, "Interaction of slow multicharged ions with solid surfaces," *Surf. Sci. Rep.*, vol. 27, no. 4–6, pp. 113–115, 1997, doi: [https://doi.org/10.1016/S0167-5729\(97\)00002-2](https://doi.org/10.1016/S0167-5729(97)00002-2).
 - [200] Y. Y. Wang *et al.*, "Energy deposition by heavy ions : Additivity of kinetic and potential energy contributions in hillock formation on CaF₂," *Sci. Rep.*, vol. 4, no. 5742, pp. 1–6, 2014, doi: 10.1038/srep05742.
 - [201] M. Kateb *et al.*, "Role of ionization fraction on the surface roughness , density , and interface mixing of the fi lms deposited by thermal evaporation , dc magnetron sputtering , and HiPIMS : An atomistic simulation," *J. Vac. Sci. Technol. A*, vol. 37, no. 3, p. 031306, 2019, doi: 10.1116/1.5094429.
 - [202] K. Movaffaq, J. T. Gudmundsson, and S. Ingvarsson, "Effect of substrate bias on microstructure of epitaxial film grown by HiPIMS : An atomistic simulation Effect of substrate bias on microstructure of epitaxial film grown by HiPIMS : An atomistic simulation," *J. Vac. Sci. Technol. A*, vol. 38, no. 4, p. 043006, 2020, doi: 10.1116/6.0000233.
 - [203] M. Kateb, J. Tomas, P. Brault, and A. Manolescu, "On the role of ion potential energy in low energy HiPIMS deposition : An atomistic simulation," *Surf. Coatings Technol.*, vol. 426, no. January, p. 127726, 2021, doi: 10.1016/j.surfcoat.2021.127726.
 - [204] HAMAMATSU, "Guide to streak cameras," 2008. doi: 10.2307/book6.3.
 - [205] K. Oh, D. Kalanov, and A. Anders, "Streak image observations of vacuum arc spots in a magnetically steered arc plasma source," in *International Symposium on Discharges and Electrical Insulation in Vacuum, ISDEIV*, 2021, pp. 222–225, doi: 10.1088/1361-6595/ac1ee1.
 - [206] A. Batrakov, S. Popov, R. Methling, D. Uhrlandt, and K. D. Weltmann, "Temporal and spatial behaviour of the single cathode spot ignition in vacuum," in *Proceedings - International Symposium on Discharges and Electrical Insulation in Vacuum, ISDEIV*, 2010, pp. 383–386, doi: 10.1109/DEIV.2010.5625868.
 - [207] S. A. Barengolts, G. A. Mesyats, and D. L. Shmelev, "Structure and Time Behavior of Vacuum Arc Cathode Spots," *IEEE Trans. Plasma Sci.*, vol. 31, no. 5, pp. 809–816, 2003, doi: 10.1109/TPS.2003.818449.
 - [208] R. P. P. Smeets and F. J. H. Schulpen, "Fluctuations of charged particle and light emission in vacuum arcs," *J. Phys. D. Appl. Phys.*, vol. 21, no. 2, pp. 301–310, 1988, doi: 10.1088/0022-3727/21/2/010.
 - [209] H.-J. Kunze, *Plasma Diagnostics*, vol. 670. Springer, Berlin, Heidelberg, 2005.
 - [210] U. Fantz, "Basics of plasma spectroscopy," *Plasma Sources Sci. Technol.*, vol. 15, no. 4, pp.

- S137–S147, 2006, doi: 10.1088/0963-0252/15/4/S01.
- [211] D. Popović, M. Mozetič, A. Vesel, G. Primc, and R. Zaplotnik, “Review on vacuum ultraviolet generation in low-pressure plasmas,” *Plasma Process. Polym.*, vol. 18, no. 9, pp. 1–18, 2021, doi: 10.1002/ppap.202100061.
 - [212] H. Daido *et al.*, “Demonstration of partially transparent thick metallic sodium in the vacuum ultraviolet spectral range,” *Opt. Express*, vol. 21, no. 23, p. 28182, 2013, doi: 10.1364/oe.21.028182.
 - [213] H.-J. Kunze, *Introduction to Plasma Spectroscopy*. Springer Heidelberg Dordrecht London New York, 2009.
 - [214] A. Kolpaková, P. Kudrna, and M. Tichý, “Study of Plasma System by OES (Optical Emission Spectroscopy),” in *WDS’11 Proceedings of Contributed Papers*, 2011, no. Part II, pp. 180–185.
 - [215] “IsoPlane Datasheet,” 2021.
 - [216] X. M. Zhu and Y. K. Pu, “Optical emission spectroscopy in low-temperature plasmas containing argon and nitrogen: Determination of the electron temperature and density by the line-ratio method,” *J. Phys. D. Appl. Phys.*, vol. 43, no. 40, 2010, doi: 10.1088/0022-3727/43/40/403001.
 - [217] A. Anders and S. Anders, “Emission spectroscopy of low-current vacuum arcs,” *J. Phys. D. Appl. Phys.*, vol. 24, no. 11, pp. 1986–1992, 1991, doi: 10.1088/0022-3727/24/11/012.
 - [218] R. Methling *et al.*, “Spectroscopic investigation of a Cu-Cr Vacuum Arc,” *IEEE Trans. Plasma Sci.*, vol. 43, no. 8, pp. 2303–2309, 2015, doi: 10.1109/TPS.2015.2443856.
 - [219] R. Methling, S. Popov, A. Batrakov, D. Uhlandt, and K. D. Weltmann, “Time-resolved spectroscopy of single cathode spots: Comparison of cathode and anode position,” *IEEE Trans. Plasma Sci.*, vol. 39, no. 11, pp. 2860–2861, 2011, doi: 10.1109/TPS.2011.2163321.
 - [220] D. Boonyawan, S. Davydov, B. Yotsombat, N. Chirapatpimol, and T. Vilaithong, “Plasma emission in vacuum arc and rf-discharge plasma sources,” *Rev. Sci. Instrum.*, vol. 73, no. 2, p. 754, 2002, doi: 10.1063/1.1429780.
 - [221] L. A. García *et al.*, “Diagnostics of pulsed vacuum arc discharges by optical emission spectroscopy and electrostatic double-probe measurements,” *Vacuum*, vol. 81, no. 4, pp. 411–416, 2006, doi: 10.1016/j.vacuum.2006.06.005.
 - [222] “NIST database.” <http://physics.nist.gov/PhysRefData/>.
 - [223] C. A. Schneider, W. S. Rasband, and K. W. Eliceiri, “NIH Image to ImageJ: 25 years of image analysis,” *Nat. Methods*, vol. 9, no. 7, pp. 671–675, 2012, doi: 10.1038/nmeth.2089.
 - [224] N. Vogel and B. Jüttner, “Measurements of the current density in arc cathode spots from the Zeeman splitting of emission lines,” *J. Phys. D. Appl. Phys.*, vol. 24, no. 6, pp. 922–927, 1991, doi: 10.1088/0022-3727/24/6/017.
 - [225] A. V. Batrakov, B. Jüttner, S. Popov, D. I. Proskurovsky, and N. Vogel, “Refraction and absorption shadow imaging of the vacuum arc cathode spot at an atomic resonance line of cathode vapors,” *IEEE Trans. Plasma Sci.*, vol. 33, no. 5 I, pp. 1465–1469, 2005, doi: 10.1109/TPS.2005.856517.
 - [226] P. Siemroth, T. Schülke, and T. Witke, “Microscopic High Speed Investigations of Vacuum Arc Cathode Spots,” *IEEE Trans. Plasma Sci.*, vol. 23, no. 6, pp. 919–925, 1995, doi:

10.1109/27.476476.

- [227] P. Siemroth, T. Schülke, and T. Witke, "Investigation of cathode spots and plasma formation of vacuum arcs by high speed microscopy and spectroscopy," *IEEE Trans. Plasma Sci.*, vol. 25, no. 4, pp. 571–579, 1997, doi: 10.1109/27.640667.
- [228] G. A. Mesyats, M. B. Bochkarev, A. A. Petrov, and S. A. Barengolts, "On the mechanism of operation of a cathode spot cell in a vacuum arc," *Appl. Phys. Lett.*, vol. 104, no. 18, p. 184101, 2014, doi: 10.1063/1.4874628.
- [229] J. C. Pickering and V. Zilio, "New accurate data for the spectrum of neutral silver," *Eur. Phys. J. D*, vol. 13, no. 2, pp. 181–185, 2001, doi: 10.1007/s100530170264.
- [230] B. Isberg, "The spectrum of Doubly Ionized Aluminium, Al III," *Ark. Fys.*, vol. 35, no. 45, pp. 551–562, 1968.
- [231] A. Anders, S. Anders, and I. G. Brown, "Transport of vacuum arc plasmas through magnetic macroparticle filters," *Plasma Sources Sci. Technol.*, vol. 4, no. 1, pp. 1–12, 1995, doi: 10.1088/0963-0252/4/1/001.
- [232] A. Anders, N. Pasaja, S. H. N. Lim, T. C. Petersen, and V. J. Keast, "Plasma biasing to control the growth conditions of diamond-like carbon," *Surf. Coat. Technol.*, vol. 201, no. 8, pp. 4628–4632, 2007, doi: 10.1016/j.surfcoat.2006.09.313.
- [233] A. Anders and E. Oks, "Charge-state-resolved ion energy distribution functions of cathodic vacuum arcs: A study involving the plasma potential and biased plasmas," *J. Appl. Phys.*, vol. 101, no. 4, p. 043304, 2007, doi: 10.1063/1.2561226.
- [234] S. Kobayashi, "X-ray thin-film measurement techniques IV. In-plane XRD measurements," *Rigaku J.*, vol. 26, no. 1, p. 3, 2010.
- [235] J. H. Batey, "Quadrupole gas analyser," *Vacuum*, vol. 37, no. 8–9, pp. 659–668, 1987, doi: [https://doi.org/10.1016/0042-207X\(87\)90052-2](https://doi.org/10.1016/0042-207X(87)90052-2).
- [236] J. Benedikt, A. Hecimovic, D. Ellerweg, and A. Von Keudell, "Quadrupole mass spectrometry of reactive plasmas," *J. Phys. D. Appl. Phys.*, vol. 45, no. 40, p. 403001, 2012, doi: 10.1088/0022-3727/45/40/403001.
- [237] Hiden Analytical, "Hiden EQP Systems," Hiden, 2014.
- [238] H. E. Swanson and E. Tatge, "Standard X-ray Diffraction Powder Patterns," U.S Government Printing Office, Washington D. C., 1953.
- [239] E. Smecca *et al.*, "AlN texturing and piezoelectricity on flexible substrates for sensor applications," *Appl. Phys. Lett.*, vol. 106, no. 23, 2015, doi: 10.1063/1.4922229.
- [240] C. Cancellieri *et al.*, "The role of Si incorporation on the anodic growth of barrier-type Al oxide," *Mater. Sci. Eng. B Solid-State Mater. Adv. Technol.*, vol. 226, no. June, pp. 120–131, 2017, doi: 10.1016/j.mseb.2017.09.012.
- [241] D. C. Zhao, G. J. Xiao, Z. J. Ma, S. H. Wu, and N. Ren, "Study on properties of aluminum film deposited on GFRP by cathodic arc technology," *Phys. Procedia*, vol. 18, pp. 240–244, 2011, doi: 10.1016/j.phpro.2011.06.088.
- [242] A. Pandey, S. Dalal, S. Dutta, and A. Dixit, "Structural characterization of polycrystalline thin films by X-ray diffraction techniques," *J. Mater. Sci. Mater. Electron.*, vol. 32, no. 2, pp. 1341–1368, 2021, doi: 10.1007/s10854-020-04998-w.

- [243] M. M. M. Bilek and D. R. McKenzie, "A comprehensive model of stress generation and relief processes in thin films deposited with energetic ions," *Surf. Coatings Technol.*, vol. 200, no. 14–15, pp. 4345–4354, 2006, doi: 10.1016/j.surfcoat.2005.02.161.

Acknowledgements

I would like to express my sincere gratitude to all the people who supported me during my doctoral work at the Leibniz Institute of surface engineering.

First of all, I would like to express my deepest gratitude to my *Doktorvater*, Prof. Dr. A. Anders, the CEO of the IOM for giving me this exciting opportunity. He has supported me with scientific and even personal advice to find the proper way for my voyage. Despite his busy schedule, his door was always open for me, and his professional advice and practical guidance always helped me. My family and I deeply appreciate his support. It has been an honor and privilege to have him as my supervisor.

Further, I am particularly thankful to Dr. D. Kalanov, who supported my experiments with practical help and scientific discussions for my thesis as a mentor. Also, he supported all my publications at IOM. I could not have undertaken my experiment without his help when my right hand was injured.

Next, I am much obliged to Dr. Y. Unutulmazsoy for her mentorship, encouragement, and scientific discussion. As a mentor, she supported me in film characterization and analysis with XRD, XRR, AFM, and SEM.

I am thankful to Dr. J. Bauer and A. Kühne for supporting the SEM investigations. Also, I special thanks to P. Birtel for supporting measuring the magnetic field of the linear magnetron. Further, I would like to extend my sincere thanks to U. Gey, and J. Knipper, and our workshop for their technical support.

I would like to thank Dr. C. Bundesmann for supporting ion beam sputtering experiment. In addition, I special thanks to Dr. A. Lotnyk for supporting the TEM measurement. Also, I am equally thankful to Dr. J. Gerlach, Dr. D. Manova, Dr. S. Mändl, Dr. C. Eichhorn, Dr. U. Helmstedt, F. Pietag, and S. Frenzel for their warm attention and encouragement.

I would be remiss not to mention my group member's support, thanks to Dr. D. Wahyu, Dr. M. Rudolph, J. Dietrich, A. Hossain, and J. Schmidt. I also greatly thank T. Pröhl and his family for their devoted support to my family's adaptation to Leipzig and friendship.

Financial support from the IOM and the Leibniz-Cooperative Excellence is greatly appreciated.

I thank my wife and my two daughters, who always gave me strength and support, and I am grateful to my parents for supporting me throughout my life.

Last but not least, I would like to thank God for his never-ending grace, mercy, provision, and meeting precious people.

Scientific Curriculum Vitae

Education

02/2019 – Current	PhD candidate, Leibniz Institute of Surface Engineering (IOM), Leipzig, Germany, Faculty of Physics and Earth Science, University Leipzig, Germany
09/2020-06/2012	Master of Science (Applied mathematics and physics), Faculty of Aerophysics and Space Research, Moscow Institute of Physics and Technology, Russia
03/2006 – 06/2009	Bachelor, Department of Mechanical Design, Manufacturing & Automation, Yanbian University of Science & Technology, China

Work experience

01/2019 – 03/2022	Leibnitz Institute of Surface Engineering (IOM), Germany
09/2016 – 12/2018	Institute for Basic Science, Republic of Korea
01/2016 – 08/2016	Ulsan National Institute of Science & Technology, Republic of Korea
08/2015 – 11/2016	Altsoft, Republic of Korea
07/2012 – 07.2015	Bioinformatics & Molecular Design Research Center, Republic of Korea

Award

Honorary credential 2009 – Best Graduation Award, Yanji, China

List of own peer-reviewed publications

Publication list of before doctoral work

1. E. E. Son, A. V. Dyrenkov, **O. Kyung**, K. E. Son, and V. Yu. Velikodny, Shock wave in a gas-liquid bubble medium, High Temperature 53, 882-886 (2015), doi: 10.1134/S0018151X1506019X.
2. C. Aniculaesei, Hyung Taek Kim, Byung Ju Yoo, **Kyung Hwan Oh**, and Chang Hee Nam, Novel gas target for laser wakefield accelerators, Review of Scientific Instruments 89, 025110 (2018), doi: 10.1063/1.4993269.
3. Sinmyung Yoon, **Kyunghwan Oh**, Fudong Liu, Ji Hui Seo, Gabor A Somorjai, Jun Hee Lee, and Kwangjin An, Specific metal-support interactions between nanoparticle layers for catalysts with enhanced methanol oxidation activity, ACS Catal. 8, 6, 5391-5398 (2018), doi: 10.1021/acscatal.8b00276.
4. C. Aniculaesei, Vishwa Bandhu Pathak, Hyung Take Kim, **Kyung Hwan Oh**, Byung Ju Yoo, Enrico Brunetti, Yong Ha Jang, Calin Ioan Hojibota, Jung Hun Shin, Jong Ho Jeon, Seongha Cho, Myung Hoon Cho, Jae Hee Sung, Seong Ku Lee, Björn Manuel Hegelich and Chang Hee Nam, Electron energy increase in a laser wakefield accelerator using up-ramp plasma density profiles, Scientific Reports 9, Article number: 11249 (2019), doi: 10.1038/s41598-019-47677-5.
5. C. Aniculaesei, Vishwa Bandhu Pathak, **Kyung Hwan Oh**, Prashant Kumar Singh, Bo Ram Lee, Calin Ioan Hojibota, Tae Gyu Pak, Enrico Brunetti, Byung Ju Yoo, Jae Hee Sung, Seong Ku Lee, Hyung Take Kim and Chang Hee Nam, Proof-of-Principle experiment for nanoparticle-assisted laser wakefield electron acceleration, Phys. Rev. Applied 12, 044041 (2019), doi: 10.1103/PhysRevApplied.12.044041.
6. Bobbili Sanyasi Rao, Myung Hoon Cho, Hyung Take Kim, Jung Hun Shin, **Kyung Hwan Oh**, Jong Ho Jeon, Byung Ju Yoo, Seong Ha Cho, Jin Woo Yoon, Jae Hee Sung, Seong Ku Lee, and Chang Hee Nam, Optical shaping of plasma cavity for controlled laser wakefield acceleration, Phys. Rev. Research 2, 043319 (2020), doi: 10.1103/PhysRevResearch.2.043319.

Publication list during doctoral work

7. **Kyunghwan Oh**, Dmitry Kalanov, André Anders, and Carsten Bundesmann, Properties of secondary particles for ion beam sputtering of silicon using low-energy oxygen ions, J. Vac. Sci. Technol. A 38, 033011 (2020), doi: 10.1116/6.0000037
8. **Kyunghwan Oh**, Dmitry Kalaonv, and André Anders, Streak image observation of vacuum arc spots in a magnetically steered arc plasma source, 29th International Symposium on Discharge and Electrical Insulation in Vacuum (ISDEIV), (2020), doi: 10.1109/ISDEIV46977.2021.9587287
9. **Kyunghwan Oh**, Dmitry Kalanov, and André Anders, High-resolution observation of cathode spots in a magnetically steered vacuum arc plasma source, Plasma Sources Sci. Technol. 30, 095005 (2021), doi: 10.1088/1361-6595/ac1ee1
10. **Kyunghwan Oh**, Dmitry Kalanov, Peter Birtel, and André Anders, High-resolution observation of cathodic arc spots in a magnetically steered arc plasma source in low pressure argon, nitrogen and oxygen atmospheres, J. Appl. Phys. 130, 183304 (2021), doi: 10.1063/5.0072021. This paper was selected as an Editor's Pick

11. Y. Unutulmazsoy, D. Kalanov, **K. Oh**, S. Karimi Aghda, J. W. Gerlach, J. M. Schneider, A. Anders, Towards decoupling the effects of the kinetic energy and potential energy of multiply charged ions in pulsed filtered cathodic arc deposition processes, in preparation

Patent

Kyunghwan Oh, J.H. No, H.Y. Son, etc, Water purification method using plasma in microbubble environment and it's apparatus, KR101639337B1, 10-2013-005780

List of own presentations

15.11.2019 Junior Researcher Seminar at IOM, Leipzig, Germany (Presentation)

“Characterization of plasma to design pulsed ionized physical vapour deposition sources”

29.05.2020 Junior Researcher Seminar at IOM, Leipzig, Germany (Presentation)

“High-resolution observation of vacuum arc spots in a magnetically steered arc plasma source”

05.02.2021 Junior Researcher Seminar at IOM, Leipzig, Germany (Presentation)

“Investigation noise fluctuations of cathodic arcs”

18.06.2021 Junior Researcher Seminar at IOM, Leipzig, Germany (Presentation)

“High-resolution of cathodic arc spots in a magnetically steered arc plasma source in low pressure argon, nitrogen and oxygen atmospheres”

29.09.2021 29th ISDEIV conference at Padova, Italy, Online, (Presentation)

“High-resolution observation of cathodic arc spots in a magnetically steered vacuum arc plasma source”

21.01.2022 Junior Researcher Seminar at IOM, Leipzig, Germany (Presentation)

“High-resolution observation of cathodic arc spots”

14.04.2022 International Online plasma seminar organized by the Gaseous Electronics Conference (GEC), Online, (Invited speaker)

“High-resolution observation of cathode spots in a magnetically steered vacuum arc plasma source”

26.05.2022 Co-author of presentations at International Conference on Metallurgical Coatings and Thin Films (ICMCTF), San Diego, USA

“Colored Random Noise of Cathodic Arcs: What Is It? Should We care?”

30.05.2022 Co-author of presentations at European materials research society (EMRS) Spring meeting, Online

“Pulsed filtered cathodic arc deposition of metastable cubic (V, Al) N thin films”

Author contribution

Title: High-resolution observation of cathode spots in a magnetically steered vacuum arc plasma source

Journal: Plasma Source Sci. Technol. 30 (2021) 095005 (9pp)

DOI: <https://doi.org/10.1088/1361-6595/ac1ee1>

Authors: **Kyunghwan Oh**, Dmitry Kalanov, and André Anders

Research concept was designed by me, D. Kalanov, and A. Anders. Experimental setups were prepared by me, and D. Kalanov. Experimental data acquisition was done by me. Formal data analysis and interpreted by me, and A. Anders. Manuscript was drafted by me. Preparation of the published work was done by me. All authors joined the editing and approved the manuscript.

Title: High-resolution observation of cathodic arc spots in a magnetically steered arc plasma source in low pressure argon, nitrogen, and oxygen atmospheres

Journal: Journal of Applied Physics 130, 183304 (2021), Editor's Pick

DOI: <https://doi.org/10.1063/5.0072021>

Authors: **Kyunghwan Oh**, Dmitry Kalanov, Peter Birtel, and André Anders

Research concept was designed by me, D. Kalanov, and A. Anders. Experimental setups were prepared by me, and D. Kalanov. Experimental data acquisition was done by me. Magnetic field data acquired by P. Birtel. Formal data analysis and interpreted by me, and A. Anders. Manuscript was drafted by me. Preparation of the published work was done by me. All authors joined the editing and approved the manuscript.

Declaration of academic integrity

I declare that this dissertation titled “Diagnostics of ion generation and fluxed from cathodic arc spots for a better understanding of energetic deposition of thin films” has been carried out under the doctoral regulations of the Faculty of Physics and Geosciences of the University of Leipzig. The present dissertation work has been prepared without unauthorized assistance and without the use of other sources, and aids than those stated. All text passages that are incorporated, verbatim or in substance, from published or unpublished writings, have been indicated. All material or services provided by other persons are indicated as such. The current dissertation has not been submitted in the same or a similar form to another examination authority for the purpose of a doctorate or any other degree, either in Germany or abroad. I have not taken any previous unsuccessful examination for a doctorate degree.

.....

(Place, date)

.....

(signature)

Summary of Dissertation

Diagnostics of ion generation and fluxes from cathodic arc spots for better understanding of energetic deposition of thin films

[Diagnostik der Ionenerzeugung und der Ionenflüsse von kathodischen Brennflecken mit dem Ziel des besseren Verständnisses von energetischen Depositionsprozessen dünner Schichten]

submitted to the Fakultät für Physik und Geowissenschaften der Universität Leipzig

by M.Sc. Kyunghwan Oh

in July 2022

with research done at

Leibniz-Institut für Oberflächenmodifizierung e.V. (IOM)

Summary

This thesis is devoted to the investigation of ion generation and fluxes from cathodic arc spots for a better understanding of the energetic deposition of a thin film with state-of-art diagnostic tools. The cathodic arc is characterized by the explosive spot ignition processes, which are the central generation processes of ions; thus, observing the spot characteristics is a challenging task.

The first part of this thesis deals with fundamental arc spot characteristics, especially the trend of apparent spot motion in a magnetically steered arc source placed in a vacuum or a reactive gas atmosphere. For this investigation, a streak camera is used as the main plasma diagnostic, having high spatial and temporal resolution. In more detail, there are two scientific questions, as follows:

1. Is there a characteristic spot time, such as a “periodic spot lifetime” or a “periodic characteristic time between spot ignitions?” This fundamental question is still open and there are two central, mutually exclusive claims in the literature. The first claim is that the spots have a periodic lifetime, or, alternatively, the second claim is that no specific frequency related to the arc ignition processes exists.
2. How different is the apparent spot motion in vacuum and in different atmospheres on the cathode surface in a magnetically steered arc observed with high spatial and temporal resolutions?

To examine whether the spots have characteristic times, streak images were produced in large numbers and analyzed by fast Fourier transformation (FFT). For the investigation of apparent spot motion in different atmospheres, the obtained streak images and spectral slope based on FFT result were analyzed. The main results of the developed scientific questions are summarized as follows:

1. The power spectrum of the arc spot fluctuations does not show any specific frequencies, which means a fractal model, and not a periodic model, can describe the arc spot ignition processes. It was experimentally shown that the cathode spot does not have any specific characteristic spot lifetime.
2. The observed spots in streak images have interesting features of apparent motion. The spots tend to strongly appear in clusters of groups for vacuum and noble gas (Ar). They are displaced in the so-called retrograde direction. The sequence of cathode spots look like a “connected chain” in a reactive gas (N₂ or O₂) atmosphere. The spots ignited in oxygen do not show a preferential direction of ignition; neither the Amperian nor the retrograde direction. The spectral slope based on FFT result in the log-log power-frequency diagram shows a tendency to be reduced in the presence of a compound layer on the cathode surface, which means the spot ignition with low-frequency events declines compared to high-frequency events in the reactive gas atmospheres.

The second part of this thesis considers cathodic arc’s application aspects: the energetic deposition of thin films. Most studies related to energetic deposition have previously investigated the effects of ion *kinetic* energy on film deposition, although the potential energy of ions also contributes to film deposition. Therefore, this thesis focuses on the effects of ion *potential* energy on film growth. In more detail, there are technical and scientific questions related to the second topic, as follows:

1. Can tuning ion charge state and plasma biasing be utilized to tune ion potential energy without influencing ion *kinetic* energy?
2. What is the ion *potential* energy effect on film growth?

To investigate the effect of ion *potential* energy on film growth, plasma diagnostic by energy-resolved mass spectrometry and deposited film characterization by XRD, XRR, AFM, profilometry and SEM were carried out. The main results of the developed questions are summarized as follows:

1. Three different experimental configurations (the reference, the high charge state, and the plasma biasing case) were conducted. The energy distribution of the ion *kinetic* energy was measured by energy-resolved mass spectroscopy for the three different configurations. The ion *potential* energy was estimated based on the measured energy distribution data without having the influence of the ion *kinetic* energy.
2. The ion *potential* energy influences the preferential direction of film growth or polycrystalline growth in the case of aluminum deposition. Although this result is overall still inconclusive, it could be a starting point for further research into the effect of ion potential energy on film deposition.

List of own publications related to this thesis

Title: High-resolution observation of cathode spots in a magnetically steered vacuum arc plasma source

Journal: Plasma Source Sci. Technol. 30 (2021) 095005 (9pp)

DOI: <https://doi.org/10.1088/1361-6595/ac1ee1>

Authors: **Kyunghwan Oh**, Dmitry Kalanov, and André Anders

Research concept was designed by me, D. Kalanov, and A. Anders. Experimental setups were prepared by me, and D. Kalanov. Experimental data acquisition was done by me. Formal data analysis and interpreted by me, and A. Anders. Manuscript was drafted by me. Preparation of the published work was done by me. All authors joined the editing and approved the manuscript.

Title: High-resolution observation of cathodic arc spots in a magnetically steered arc plasma source in low pressure argon, nitrogen, and oxygen atmospheres

Journal: Journal of Applied Physics 130, 183304 (2021). This paper was selected as an Editor's Pick.

DOI: <https://doi.org/10.1063/5.0072021>

Authors: **Kyunghwan Oh**, Dmitry Kalanov, Peter Birtel, and André Anders

Research concept was designed by me, D. Kalanov, and A. Anders. Experimental setups were prepared by me, and D. Kalanov. Experimental data acquisition was done by me. Magnetic field data acquired by P. Birtel. Formal data analysis and interpreted by me, and A. Anders. Manuscript was drafted by me. Preparation of the published work was done by me. All authors joined the editing and approved the manuscript.

Title: Towards decoupling the effects of the kinetic and potential energy in a pulsed filtered cathodic arc process in preparation

Film deposition and mass spectrometry were carried by me, and D. Kalanov. Plasma data analysis and interpreted by me, and D. Kalanov. Material data analysis and interpreted by Y. Unutulmazsoy. Manuscript was drafted by Y. Unutulmazsoy. All authors joined the editing and approved the manuscript.

Scientific mentors and their contributions

Ph.D. Dmitry Kalanov – Supporting plasma diagnostic installation and execution, investigation of the data, and assisting in editing thesis

Leibniz Institute of Surface Engineering (IOM), Leipzig

Dr. Yeliz Ekinci Unutulmazsoy – Supporting film characterization method and interpretation film characterized data and assisting in editing thesis

Leibniz Institute of Surface Engineering (IOM), Leipzig

Doctoral committee

Prof. Dr. Jan Meijer (Chairman)

Felix-Bloch-Institute for Solid State Physics Department for Applied Quantum System (AQS),
University Leipzig

Prof. Dr. André Anders (Supervisor)

Leibniz Institute of Surface Engineering (IOM), Leipzig

Felix-Bloch Institute for Solid State Physics, Leipzig University

Prof. Dr. Bernd Abel

Felix-Bloch Institute for Solid State Physics, Leipzig University

Supervisor

Prof. Dr. André Anders (Betreuer)

Leibniz Institute of Surface Engineering (IOM), Leipzig

Felix-Bloch Institute for Solid State Physics, Leipzig University

Institutes

This thesis work was investigated between January 2019 and December 2021

at the Leibniz Institute of Surface Engineering (IOM)

Permoserstraße 15, 04318 Leipzig, Germany